NASA CONTRACTOR REPORT

NASA CR-2012

THE ROLE OF FLUCTUATING FORCES IN THE GENERATION OF COMPRESSOR NOISE

by Hanno H. Heller and Sheila E. Widnall

Prepared by
BOLT BERANEK AND NEWMAN, INC.
Cambridge, Mass. 02138
for Langley Research Center

NATIONAL AERONAUTICS AND SPACE ADMINISTRATION • WASHINGTON, D. C. • MAY 1972

1. Report No.	2. Government Accession No.	3. Recipient's Catalog No.
NASA CR-2012		

4. Title and Subtitle	5. Report Date
The Role of Fluctuating Forces in the Generation of Compressor Noise	May 1972
	6. Performing Organization Code
7. Author(s)	8. Performing Organization Report No.
Hanno H. Heller and Sheila E. Widnall	2160
9. Performing Organization Name and Address	10. Work Unit No.
Bolt Beranek and Newman, Inc. Cambridge, MA 02138	11. Contract or Grant No. NAS 1-9883
	13. Type of Report and Period Covered Contractor Report
12. Sponsoring Agency Name and Address National Aeronautics and Space Administration Washington, D.C. 20546	14. Sponsoring Agency Code

15. Supplementary Notes

16. Abstract This report describes the results of a theoretical and experimental study on the role of aerodynamically-induced fluctuating forces in the sound generation by axial-flow compressors. Analytical models for the generation and radiation of sound by rotor/stator combinations were developed. For the experimental substantiation of the analytical results, the technology was developed to measure fluctuating forces directly on rotating airfoils using miniature differential-pressure sensors and FM telemetry. Under the assemption of full coherence of the force field on the blade, radiated sound power was predicted from the force measurements on blades and compared with measured sound power. Both broadband radiation from a single rotating airfoil and discrete-frequency radiation due to interaction of multi-bladed stator/rotor configurations were investigated. The results indicate the necessity to obtain information on the details of the force field for accurate prediction of the radiated sound spectrum.

17. Key Words (Suggested by Author(s))	18. Distribution Statement
Aircraft Noise Rotating Blade Noise Compressor Noise Fan Noise	Unclassified - Unlimited

19. Security Classif. (of this report)	20. Security Classif. (of this page)	21. No. of Pages	22. Price*
Unclassified	Unclassified	114	$3.00

*For sale by the National Technical Information Service, Springfield, Virginia 22151

1. Aerodynamic noise
2. Compressor blades
3. Noise (Sound)

TABLE OF CONTENTS

TABLE OF CONTENTS *(Continued)*

LIST OF FIGURES AND TABLES

LIST OF FIGURES AND TABLES *(Continued)*

LIST OF FIGURES AND TABLES *(Continued)*

LIST OF SYMBOLS

a	correction factor
A	blade area
B	number of rotor blades
c	speed of sound
D	drag force component
d_1	drag force component per unit length
e	voltage
f	frequency
F	force
F_1	force per unit length
h	spacing
k	order of input harmonic or wave number
m	order of sound harmonic
n	mB
p	sound pressure
s	sensitivity
S	source strength
S_1	source strength per unit length
T	thrust force component
t_1	thrust force component per unit length
U	flow speed
V	number of stator blades
W	sound power
x,y	co-ordinates
θ	angle around rotor
λ	kV
μ	modal order = $mB-kV$
Π	sound power
ρ	density
ω	circular frequency
Ω	angular velocity

THE ROLE OF FLUCTUATING FORCES IN THE GENERATION OF COMPRESSOR NOISE

Hanno H. Heller
Sheila E. Widnall

Bolt Beranek and Newman Inc.
Cambridge, Massachusetts

I. INTRODUCTION

The noise generated by rotating aerodynamic machinery such as compressors, fans, turbines, and helicopter rotors is composed of *broadband noise* and superimposed *discrete tones* at multiples of the rotational frequency. Radiated sound power increases approximately with the sixth power of a typical flow speed, indicating a generating mechanism that relates to fluctuating aerodynamic forces. The research program described in this report was undertaken to study the fluctuating forces on rotor blades in particular, and, without identifying specific force generating mechanisms, to relate these forces to the sound radiated from the blades.

To establish experimentally the relationship between forces and radiated sound, we developed special techniques for measuring forces on rotating* blades and made appropriate measurements of forces and radiated sound. The results were interpreted by use of an analytical model for sound radiated by fluctuating forces.

Our *analytical* efforts were directed toward understanding two cases of aerodynamic sound radiation: (1) radiation directly into a three-dimensional environment (e.g., a propeller) and (2) radiation first into a "two-dimensional" environment, such as an annular duct, and then into a three-dimensional environment (e.g., a compressor rotor/stator configuration). Our *experimental* efforts, however, were limited to the first case – specifically to a single model rotor and a model rotor/stator configuration,

* Although fluctuating forces on stationary blades will also cause sound generation, these were not the object of study in the described research effort.

both operating with and without superimposed flow and radiating directly into a three-dimensional environment. Although it was not possible to substantiate all theoretical results by appropriate experiments, we present all theoretical findings since they allow for conclusions on some important features of compressor noise theory.

II. COMPRESSOR NOISE THEORY

In this section we discuss the generation of sound by fluctuating forces on rotating blades that operate (1) in a "free environment" (i.e., radiating directly into a three-dimensional environment) and (2) in an "obstructed environment" (i.e., radiating first into a two-dimensional and then into a three-dimensional environment). In both cases, fluctuating forces can be represented by aerodynamic dipoles. In the following sections, we consider the sound power radiation from stationary dipole sources (for completeness, we also discuss monopole sources) and in subsequent sections, the sound power radiation from rotating sources. For rotating sources we discuss the two cases of a rotor-stator configuration in a free-field environment and in a narrow annular duct of semi-infinite extent. This discussion leads to a simplified model for the sound radiated by a ring of fluctuating forces and will be compared to existing exact models.

In discussing the results of the experimental program in Chapter III, we will use this model to interpret discrete frequency sound; broadband noise will be discussed in terms of the simple stationary dipole source.

A. Sound Radiation From Stationary Aerodynamic Sources

1. Analytical approach

We consider a source located between two semi-infinite parallel plates of separation h, a distance small in comparison to a wavelength of sound at the frequency in question (Fig. 1). The problem is to determine how much sound is radiated into the free environment beyond the plates in comparison to the sound generated by the same source in free space. We will first solve the sound generation problem in the two-dimensional environment, satisfying the boundary condition, $p = 0$, on the narrow opening. We will then solve for the particle velocity at this slit and calculate the resulting sound field in the three-dimensional environment. The radiation of the slit into free space is most naturally expressed by a Fourier transfer in the y direction, which turns into a plane-wave reflection problem at the slit. Therefore, the sound generation in the constrained environment is also calculated by means of a Fourier transform in y so that the plane wave components at the slit are immediately available.

The point-sources of interest are the monopole and the vertical and horizontal dipoles.

2. Results

The results of the analysis, presented in Appendix A and summarized in Table I, show that the sound power from a monopole source observed in the free-field environment is independent of whether the monopole source radiates directly into the free field, or whether the source radiates first into a two-dimensional and then into the three-dimensional environment.

The same statement holds for a vertical* dipole. However, locating a horizontal* dipole in a two-dimensional environment results (for a given force) in twice the power observed in the free field; i.e., a 3 dB increase in power (see reference 1).

These simple equations are assumed to be applicable to broadband rotor-noise analysis below frequencies for which the wavelengths are smaller than the distance of hub to shroud (alternatively, root to tip of blade). The free-field dipole power equation is used in the interpretation of broadband sound radiation from the experimental rotor and stator/rotor configurations.

B. Simplified Model for the Sound Radiated by Fluctuating Forces in Compressors

1. Introduction

The calculation of sound radiated by fluctuating forces in axial compressors has been the subject of much research. There are currently exact solutions, of some complexity, for the sound radiated by a ring of fluctuating forces representing a rotor and a stator located in (1) a free field (reference 2) and (2) a confined environment such as a circular duct of semi-infinite length (reference 3) (Fig. 2).

These solutions involve special mathematical functions and final results require the use of a digital computer. In the following, we employ simple approximate analytical expressions for the total power radiated by fluctuating forces for the two cases.

---

* For definition of orientation see Table I.

	SCHEMATIC OF CONFIGURATION (TWO SEMI-INFINITE PLATES, SEPARATED BY A DISTANCE h WITH SOURCE "SPANNING" GAP)	POWER OBSERVED IN FREE-FIELD FROM: SOURCE LOCATED IN TWO-DIMENSIONAL ENVIRONMENT	POWER OBSERVED IN FREE-FIELD FROM: SOURCE LOCATED IN FREE-FIELD ENVIRONMENT
MONOPOLE	PLAN 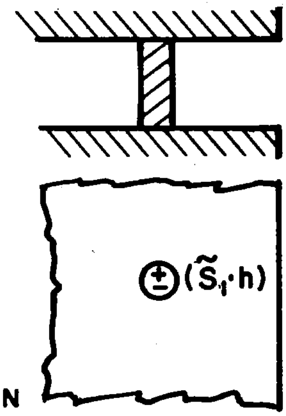 ELEVATION	$\frac{\rho\omega^2 (S_1 h)^2}{4\pi c}$	$\frac{\rho\omega^2 \cdot S^2}{4\pi c}$
"HORIZONTAL DIPOLE"	PLAN 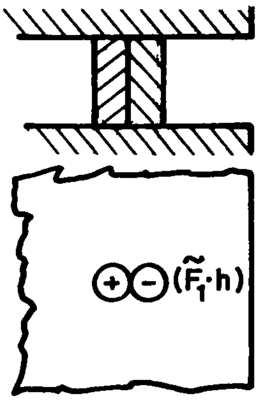 ELEVATION	$\frac{F_1^2 \omega^2 h^2}{6\pi\rho c^3}$	$\frac{F^2 \omega^2}{12\pi\rho c^3}$
"VERTICAL DIPOLE"	PLAN 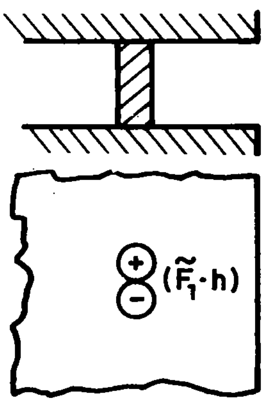 ELEVATION	$\frac{F_1^2 \omega^2 h^2}{12\pi\rho c^3}$	$\frac{F^2 \omega^2}{12\pi\rho c^3}$

TABLE I: RADIATED POWER FROM STATIONARY POINT SOURCES (Note that $F_1 h = F$, $S_1 h = S$)

Our results using these expressions are then compared with the exact theories of references 2 and 3, by which insight into the nature of the sound generation process is obtained. The approximate solutions also indicate what type of "model" is appropriate in the calculation of compressor noise. In other words, an exact solution for a rotor in a free field can hardly be used as an exact solution for compressor noise if the range of parameters is such that enclosure within the duct affects the process of sound generation.

The approximate solutions are based on the ratio of typical lengths in the problem. It is a familiar idea in acoustics that if a geometrical length is smaller (or larger) than a wavelength, certain (different) approximations can be made. The mathematical foundation for these ideas is the theory of singular perturbation problems (reference 4) and the method of matched asymptotic expansions, one of the techniques which has been developed specifically for this type of problem. This technique has found wide application in fluid mechanics and has lately begun to appear in problems of acoustics and aerodynamic noise (references 4 and 5). The formal method of matched asymptote expansion will not be used; the physical reasoning which strongly underlies the mathematical techniques will be stressed in obtaining the approximate solution.

2. Rotor/stator in free-field environment

We now discuss an approximate solution for the sound radiated by fluctuating lift and drag forces on a rotor/stator in a free field which is directly comparable to the solution originally obtained by Lowson. In Lowson's model, the fluctuating forces acting on the blade surface are considered to be point forces. This approximation is justified if the blade chord and span over which the fluctuating forces act are both small in comparison to the acoustic wavelength. In many applications, the chord, but not the span, fulfills this requirement. In such cases, a line of forces along the blade span would be more appropriate; however, these cases will not be further considered although they could be included with a slight extension.

The "point source" model for rotor/stator radiation in a free field is shown in Fig. 3. This is identical to Lowson's model except the stator blade pattern begins at $\theta = 0$ for convenience.

If the stator blades were represented by *steady* point forces, evenly spaced around the ring, the force distribution in θ could be written as the Fourier series for a repeated pattern of delta functions.

$$\vec{F}_s(\theta) = \frac{V\vec{F}}{2\pi} \sum_{k=-\infty}^{\infty} \cos kV\theta \ , \tag{1}$$

where V is the number of blades and $\vec{F}$ is the force on a single blade. Likewise a steady (with respect to the rotor) force distribution on the rotor would be

$$\vec{F}_r(\theta,t) = \frac{B\vec{F}}{2\pi} \sum_{m=-\infty}^{\infty} \cos mB(\theta-\Omega t) \ , \tag{2}$$

which represents a repeated pattern of delta functions rotating with angular velocity Ω.

To represent the *unsteady forces on the stator* due to interaction with the rotor, the stator delta function pattern is multiplied by a function of θ and t that incorporates the amplitude, frequency, and phase shift from blade to blade due to a harmonic of the rotor

$$\vec{F}_s(\theta,t) = \frac{V}{2\pi} \sum_{m=-\infty}^{\infty} \vec{F}_m \cos mB(\theta-\Omega t) \sum_{k=-\infty}^{\infty} \cos kV\theta \ , \tag{3}$$

where $\vec{F}_m$ is the force on a stator blade due to interaction with the m*th* harmonic of the rotor.

A similar expression for the *unsteady force distribution on the rotor* is obtained by multiplying the rotating pattern of delta functions with a function of θ that gives the amplitude and appropriate phase shift between blades due to interaction with the fixed stator.

$$\vec{F}_r(\theta,t) = \frac{B}{2\pi} \sum_{k=-\infty}^{\infty} \vec{F}_k \cos(kV\theta) \sum_{m=-\infty}^{\infty} \cos mB(\theta-\Omega t) \ , \tag{4}$$

where $\vec{F}_k$ is the force on the rotor due to interaction with the stator harmonic.

Figure 3 indicates schematically the repeated delta function patterns multiplied by a continuous wave that gives the appropriate amplitude and phase for the interaction. In these expressions, any phase shift which occurs in the unsteady aerodynamic forces is ignored since it is the same from blade to blade.

The unsteady forces on the stator can also be written

$$\vec{F}_s(\theta,t) = \frac{V}{2\pi} \sum_{k=-\infty}^{\infty} \sum_{m=-\infty}^{\infty} \vec{F}_m \cos[(mB-kV)\theta-mB\Omega t] \ , \tag{5}$$

from Eq. 3, by using standard trigonometric relationships. The spatial pattern depends on mB-kV; the frequency is mBΩ. The corresponding relation for the unsteady forces on the rotor, from Eq. 4, is

$$\vec{F}_r(\theta,t) = \frac{B}{2\pi} \sum_{m=-\infty}^{\infty} \sum_{k=-\infty}^{\infty} \vec{F}_k \cos[(mB-kV)\theta-mB\Omega t] \ . \tag{6}$$

As noted by Lowson, the principle difference in harmonic content between stator/rotor and rotor/stator interaction is that a single harmonic of the rotor induces a single frequency in the unsteady force distribution on the stator while a single harmonic of the stator disturbance induces many harmonics in the rotor unsteady force distribution (in a nonrotating coordinate system).

The Fourier decomposition of the phased point sources gives the familiar spinning modes, waves which travel around the ring at a rotational speed

$$\Omega_{eff} = \frac{mB}{mB-kV} \Omega \ . \tag{7}$$

A "thrust" spinning mode is sketched in Fig. 4. (The "drag" mode, a distribution of force vectors in the θ direction, is more difficult to sketch but is conceptually similar.) For practical applications, the sound radiation for models with m being positive are the most important; in this case the effective wave speed $\Omega_{eff}R_0$ becomes supersonic, which, to a good approximation, is a necessary condition for efficient sound radiation. If an exact solution is sought for the far-field radiation from the rotating lift and drag modes of the stator (Eq. 5) and the rotor (Eq. 6), Lowson's theory is obtained. However, we may obtain an approximate solution for the total acoustic power by making the simplification suggested in Fig. 4 from the rotating ring mode to the traveling line mode since *the important sound radiation in compressors comes from modes which rotate at supersonic speeds.* The conditions for this approximate solution to be valid are that the radius of the ring is large in comparison to the acoustic wavelength and the wave speed is supersonic.

The total acoustic power for the rotating ring mode is then the acoustic power/unit length in the traveling line mode times the perimeter $2\pi R$. It is useful to consider the individual blade elements in the linear model (Fig. 4c) to obtain the relationship between the lift and drag components of the traveling mode. The resultant unsteady force $\vec{F}$ will be largely normal to the incoming flow direction. The unsteady force distribution in the traveling line mode is obtained by replacing θ by y/R_0 in Eqs. 5 and 6. (A factor $1/R_0$ enters in the transformation from $\theta \rightarrow y$ since a force distribution per unit angle has been changed to a force distribution per unit length.)

We obtain for the stator

$$\vec{F}_s(y,t) = \frac{V}{2\pi R} \sum_{k=-\infty}^{\infty} \sum_{m=-\infty}^{\infty} \vec{F}_m \cos[(mB-kV)y/R-mB\Omega t] , \qquad (8)$$

and for the rotor,

$$\vec{F}_r(y,t) = \frac{V}{2\pi R} \sum_{k=-\infty}^{\infty} \sum_{m=-\infty}^{\infty} \vec{F}_k \cos[(mB-kV)y/R-mB\Omega t] . \qquad (9)$$

Each mode of radiation from either rotor or stator is a traveling wave disturbance of the type

$$\vec{f}_i = t_i \cos(k_y y-\omega t)\vec{i}-d_i \cos(k_y y-\omega t)\vec{j} , \qquad (10)$$

where t_i and d_i are the thrust and drag components respectively. The total acoustic power/unit length radiated by this type of singularity distribution is derived in Appendix B. To obtain the total power for the compressor model, Eq. B-14 is multiplied by the perimeter of the ring, $2\pi R_0$:

$$\Pi = \frac{\pi R_0}{4\rho c k}\left[\frac{t_i^2}{2}(k^2-k_y^2) + d_i^2 k_y^2\right] \qquad \text{for } k > k_y \ . \tag{11}$$

The variables t_i, d_i, k and k_y may be identified for the stator and rotor from Eqs. 8 and 9 as follows:

$$k = \frac{mBM}{R_0}\ , \qquad k_y = \frac{mB-kV}{R_0}\ ; \tag{12}$$

for the stator,

$$t_i = \frac{V}{2\pi R_0} T_m\ , \qquad d_i = \frac{V}{2\pi R_0} D_m\ ;$$

and for the rotor,

$$t_i = \frac{B}{2\pi R_0} T_k\ , \qquad d_i = \frac{B}{2\pi R_0} D_k\ .$$

For the stator, the rms acoustic power level due to a single mode is

$$\Pi_{n\lambda} = \frac{V^2}{8\pi R_0^2 \rho c}\frac{1}{nM}\left\{\frac{T_n^2}{4}[(nM)^2-\mu^2] + \frac{D_n^2}{2}\mu^2\right\} \quad \text{for } nM > \mu\ , \tag{13}$$

where $n = mB$, $\lambda = kV$, $\mu = n-\lambda$. For the rotor, the rms acoustic power level due to a single mode is

$$\Pi_{n\lambda} = \frac{B^2}{8\pi R_0^2 \rho c}\frac{1}{nM}\left\{\frac{T_\lambda^2}{4}[(nM)^2-\mu^2] + \frac{D_\lambda^2 \mu^2}{2}\right\} \quad \text{for } nM > \mu\ . \tag{14}$$

These results are an approximate analytic equivalent to Lowson's results, which he expresses (for the rotor) as

$$W_{n\lambda} = \frac{1}{8\pi R_0^2 \rho c} \left[(Mn)^2 \, (BT_\lambda)^2 \, \hat{T} + \mu^2 (BD_\lambda)^2 \, \hat{D} \right] . \tag{15}$$

The analytic equivalents to $\hat{T}$ and $\hat{D}$ are

$$\hat{T} = \frac{(nM)^2 - \mu^2}{4(nM)^3} ; \qquad \hat{D} = \frac{1}{2nM} . \tag{16}$$

Equations 16 are close to the approximations suggested by Lowson upon examining his numerical results:

$$\hat{T} \sim \frac{1}{4nM} ; \qquad \hat{D} \sim \frac{1}{2nM} ,$$

except that $\hat{T}$ is missing the dependence upon μ.

Figure 5 compares the numerical result for $\hat{T}$ and the approximation of Eq. 16. The new results improve the suggested approximation for $\mu \neq 0$. However, the purpose of this comparison is not to provide a new approximate for $\hat{T}$ but to provide an understanding of the nature of the approximate solution, its justification, and its accuracy.

A clarification of the suggestion by Lowson that $\mu = 0$ is an optimum choice for quiet compressors is seen in Eq. 16. For this model of a rotor in a free environment, $\mu = 0$ is an optimum choice if

$$D_\lambda > T_\lambda / \sqrt{2} ,$$

which corresponds roughly to stagger angles, β, of 55° (see Fig. 4c). In the next section, a similar model for a rotor in a confined environment will be discussed.

3. Rotor/stator in a narrow annulus

We now consider sound radiation from fluctuating lift and drag forces for a rotor/stator in a narrow semi-infinite annular duct, as sketched in Fig. 6. We "unwrap" the annular duct and develop an approximate solution for the sound radiated into free space by fluctuating lift and drag forces on a vertical cascade of blades confined between two solid plates.

The representation of the fluctuating point forces as sinusoidal distributions of singularities along the y axis is the same as for the rotor/stator in free space, given by Eqs. 8 and 9; what is different is the solution for the acoustic field.

If the distance between the plates is smaller than $\lambda/2$, the acoustic solutions within the confined environment are two-dimensional oblique plane waves in x and y. The waves are generated at the blades and reflected at the free edge so that only a small fraction of the acoustic power is transmitted into the free space beyond the edge. This immediately raises the question of the applicability of a semi-infinite model to real compressors in cases where the duct seriously modifies the generation of acoustic power over the free-field case. However, several solutions of this type have been developed by more elaborate mathematical techniques and it is our purpose to model approximately these solutions.

The sound power/unit length generated in the confined environment and transmitted into free space by the combination of the fluctuating lift and drag of Eq. 10 is derived in Appendix C. To obtain the total power for the compressor sketched in Fig. 6, the power/unit length is multiplied by the perimeter of the duct, $2\pi R_0$. The result is

$$\Pi = \frac{\pi R_0}{4\rho c k}\left(t_i\sqrt{k^2-k_y^2} - d_i k_y\right)^2 \qquad k > k_y \ . \tag{17}$$

Equation 17 is the equivalent of Eq. 11 for the *confined rotor case*. The two formulas have some rather interesting relationships:

1. In the absence of drag, the acoustic power due to the fluctuating thrust radiated from the confined environment is doubled.

2. In the absence of thrust, the acoustic power due to fluctuating drag is the same.

3. The power radiated into free space by the thrust and drag forces is not just the sum of the squares — there is a cross term between thrust and drag.

It would be more appropriate to compare Eq. 17 with the power radiated "forward" by the rotor in a free environment (Eq. B-15, multiplied by $2\pi R_0$):

$$\Pi = \frac{\pi R_0}{8\rho c k}\left[\frac{t_i^2}{2}(k^2-k_y^2) + k_y^2 d_i^2 - \frac{4}{\pi} d_i t_i \sqrt{k^2-k_y^2}\, k_y\right] \qquad k > k_y\ , \tag{18}$$

which also involves a cross term between thrust and drag. Equation 12 gives the correspondence between t_i, d_i, k and k_y and the compressor parameters of Eqs. 8 and 9.

The formulas, equivalent to Eqs. 13 and 14, for the rms acoustic power radiated into free space by a single mode of the rotor/stator fluctuating forces *confined within a narrow annular duct* are for the stator,

$$\Pi_{n\lambda} = \frac{V^2}{16\pi R_0^2 \rho c}\,\frac{1}{nM}\,\{T_n[(nM)^2-\mu^2]^{\frac{1}{2}} - D_n\mu\}^2 \qquad nM > \mu\ , \tag{19}$$

and for the rotor,

$$\Pi_{n\lambda} = \frac{B^2}{16\pi R_0^2 \rho c}\,\frac{1}{nM}\,\{T_\lambda[(nM)^2-\mu^2]^{\frac{1}{2}} - D_\lambda\mu\}^2 \qquad nM > \mu\ . \tag{20}$$

4. Discussion of developed model

The expressions for the total acoustic power due to harmonic fluctuating lift and drag forces (acting on rotor blades) for the various simplified models are summarized in Table II, along with associated nondimensional functions T_1, T_2, and T_3. The weighting

TABLE II: SUMMARY OF RESULTS

Total Acoustic Power — Free Rotor	$\Pi_{n\lambda} = \left(\frac{B^2T_\lambda^2}{8\pi R_0^2\rho c}\right) \cdot T_1$	$T_1 = \frac{1}{nM}\left\{\frac{1}{4}\left[(nM)^2-\mu^2\right] + \left(\frac{D}{T}\right)_\lambda^2 \cdot \frac{\mu^2}{2}\right\}$
Power Radiated Forward — Free Rotor	$\Pi_{n\lambda} = \left(\frac{B^2T_\lambda^2}{8\pi R_0^2\rho c}\right) \cdot T_2$	$T_2 = \frac{1}{2nM}\left\{\frac{1}{4}\left[(nM)^2-\mu^2\right] + \left(\frac{D}{T}\right)_\lambda^2 \frac{\mu^2}{2} - \frac{2}{\pi}\,\frac{D}{T}\sqrt{(nM)^2-\mu^2}\,\mu\right\}$
Power Radiated into Free Space Confined Rotor	$\Pi_{n\lambda} = \left(\frac{B^2T_\lambda^2}{8\pi R_0^2\rho c}\right) \cdot T_3$	$T_3 = \frac{1}{2nM}\left[\sqrt{(nM)^2-\mu^2} - (D/T)_\lambda\,\mu\right]^2$

function T_1 (related to the *total power radiated by the rotor in a free field*) is in very close agreement with Lowson's (reference 2) more exact but complex theory. The second expression, T_2 (relating to the power *radiated upstream from the free rotor*), is the appropriate quantity to compare with Lansing's (reference 3) theory for the rotor confined in a semi-infinite duct. The effect of close *confinement in a narrow annulus*, which indicates the importance of the duct, is given by T_3. In both T_2 and T_3, the power radiated downstream is obtained by changing the sign of the cross-product term involving thrust and drag.

We will now compare the results of these models for various values of the ratio of drag force and thrust force, D/T. We will then compare the simplified models with the calculation presented by Lansing.

a. D/T = 0

When the fluctuating forces are aligned only along the axis of the duct, the expressions for T_1, T_2 and T_3 become quite simple. The total power from the rotor in a free environment is then proportional to

$$T_1 = \frac{(nM)^2-\mu^2}{4nM} \quad .$$

The power radiated forward from a free rotor is proportional to just half of this expression. The power radiated into free space from the annular duct is twice the total power radiated by the same fluctuating forces in a free environment (see also reference 1). Figure 7 shows T_3 as a function of nM for various values of μ. The acoustic power is reduced as μ increases.

b. D/T > 0

When the drag component of the fluctuating forces is greater than zero, the results become a good deal more interesting because some cancellation occurs in the forward direction due to the presence of both fluctuating lift and fluctuating drag. Figure 8a shows the function T_1, which is equivalent to that in Lowson's theory. Figure 8b shows the function T_2 (relating to the power radiated upstream from a rotor in a free environment).

Due to the negative cross-product terms between lift and drag, some dips in the curves are present. This may have an application in fan noise reduction. Figure 8c shows T_3, the function that relates to the acoustic power radiated into free space due to fluctuating lift and drag forces within a confined annular duct. The dips in the curve are more pronounced than in Figs. 8a and 8b and complete cancellation occurs for certain combinations. One must remember, however, that cancellation in the power radiated forward becomes reinforcement in the power radiated downstream. Figures 9a,b,c show similar results for D/T = 1.0. In Fig. 9a, the total power radiated by the rotor in the free environment is now dominated by the efficiency of the fluctuating drag forces which, as noted by Lowson, is proportional to μ^2. Thus T_1 is minimized for $\mu = 0$. (As discussed previously, $\mu = 0$ is an optimum only if $D/T > 1/\sqrt{2}$.) The power radiated forward continues to show dips (Fig. 9b) and the power radiated into free space from the annular duct still has broad areas of cancellation (Fig. 9c). (With corresponding areas of reinforcement downstream.)

The exact solution for sound radiated by fluctuating forces distributed within a semi-infinite duct of circular cross section was presented by Lansing (reference 3). Although Lansing could have considered any distribution of forces, he presented results for a ring of point forces, located at a radius of 80% of the duct radius (similar to Lowson's model). Using the simple ideas of the approximate theory, one would argue that the duct would have essentially no effect on the power radiated by the fan, being of radius much larger than a wavelength, unless the sources were close to (within a wavelength) the solid wall, whereupon the power would increase and eventually double.*

The simple model also indicates that the proper comparison between the Lowson and Lansing calculations is acoustic power radiated forward rather than "total power", since in the Lansing model most of the acoustic energy travels down the semi-infinite duct and is not considered.

---

* As is well-known (see, for example, reference 6, p. 503), the power radiated by a simple source located in a duct approaches the free-field value by stepwise excitation of an increasing number of duct modes, and the free-field value gives a good average value for the power radiated as a function of frequency once the dimensions of the duct are large.

Lansing presents numerical results for the case $\mu = 5$, $R = 0.8$. His parameter T is equivalent to nM/0.8. The curve he presents is related to our parameter T_1 (or T_2 or T_3) as

$$10 \log \frac{T}{(4\pi\ 0.8)^2} .$$

Figure 10 shows Lansing's calculation replotted using our notation, 10 log T vs nM (which is also the notation used by Lowson). When we compare Lansing's result with Lowson's (or ours) for *total* power radiated by a rotor in a free environment, taking T_1, we see an obvious discrepancy. However, if we compare Lansing's result with only the acoustic power radiated forward, taking T_2, as calculated by our simple model, we find much closer agreement.

In particular, the dip in Lansing's curve can now be interpreted as cancellation of the effect of the fluctuating lift and drag forces rather than as duct resonances. Except for the presence of duct cross modes, his curve is identical to T_2 for large values of nM and the "free-field" value serves as the appropriate mean value as the duct modes are excited. Since the sources are located a distance $R = 0.2$ from the solid wall, a maximum of 3 dB could be added at the low-frequency end whenever $0.2\ nM < \pi/2$ or when $nM \lesssim 8$. (A more accurate way to calculate this effect is to use the solution for a "two-dimensional" source approaching an infinite wall.) However, it is not our intent to continue to refine the approximate theory, but merely to point out its utility in helping to formulate and evaluate more exact methods.

Also indicated on Fig. 10 is the acoustic power radiated into free space if the fluctuating forces were confined in a narrow annulus, T_3. Power would increase significantly at high frequencies and cancellation would be more effective at low frequencies.

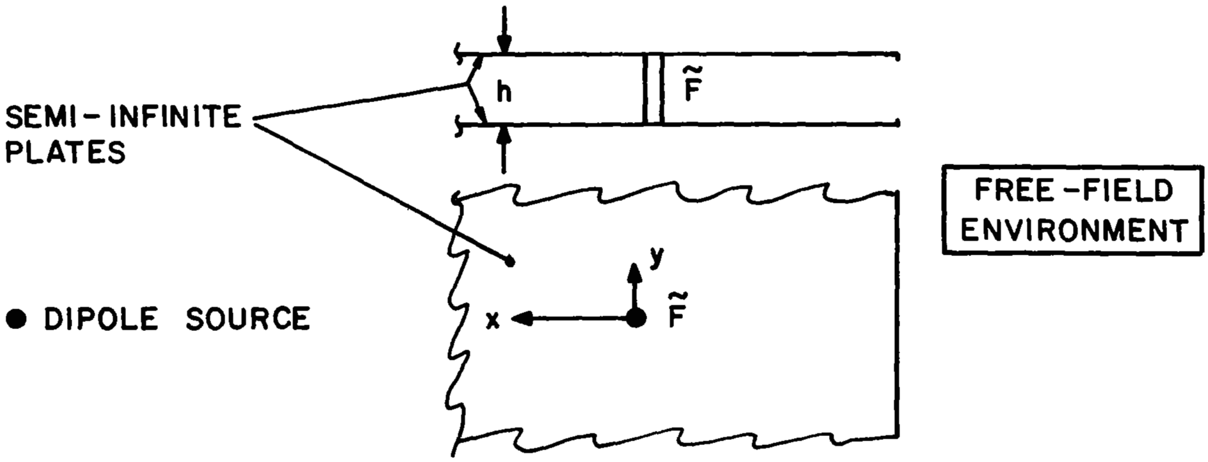

FIG. 1. MODEL FOR STATIONARY DIPOLE SOURCE IN TWO-DIMENSIONAL SEMI-INFINITE ENVIRONMENT

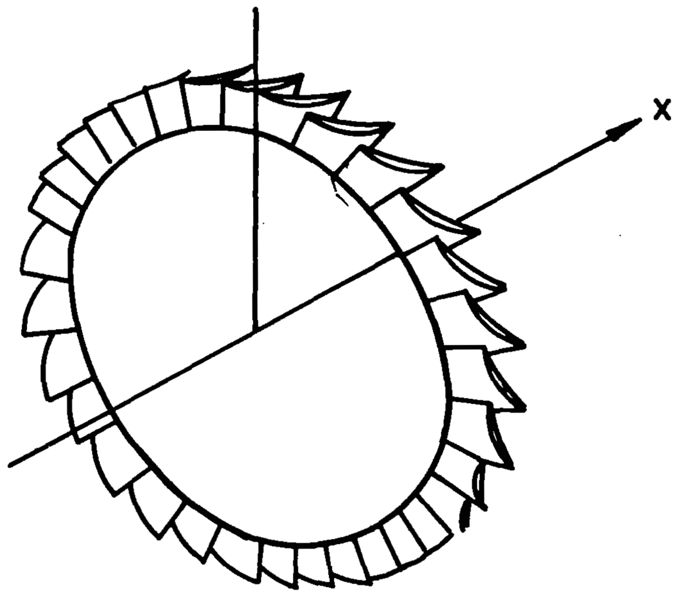

a) FREE ROTOR

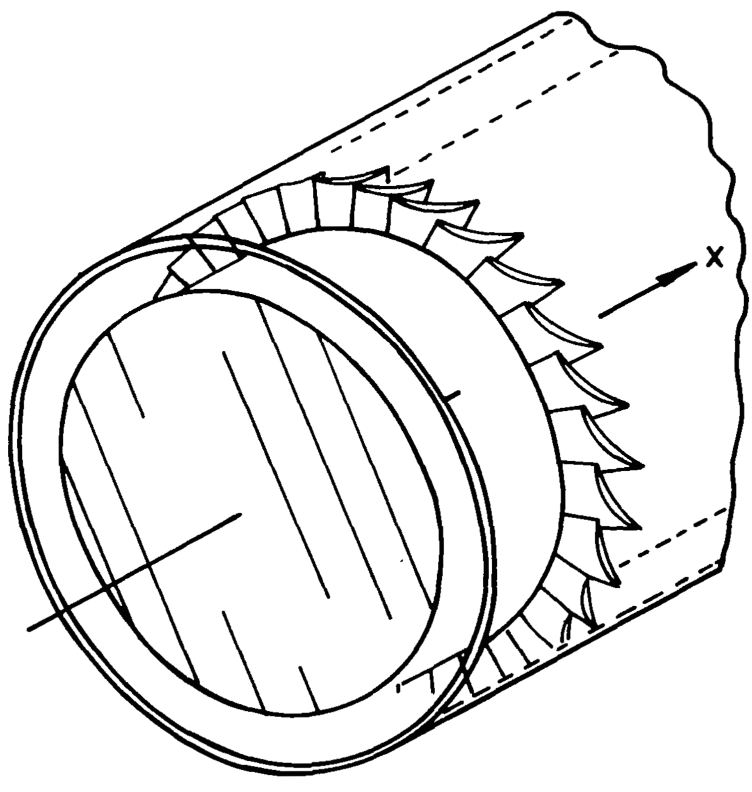

b) ROTOR IN ANNULAR DUCT

FIG. 2. ROTOR/STATOR CONFIGURATION IN (a) FREE-FIELD ENVIRONMENT AND IN (b) ANNULAR SEMI-INFINITE DUCT

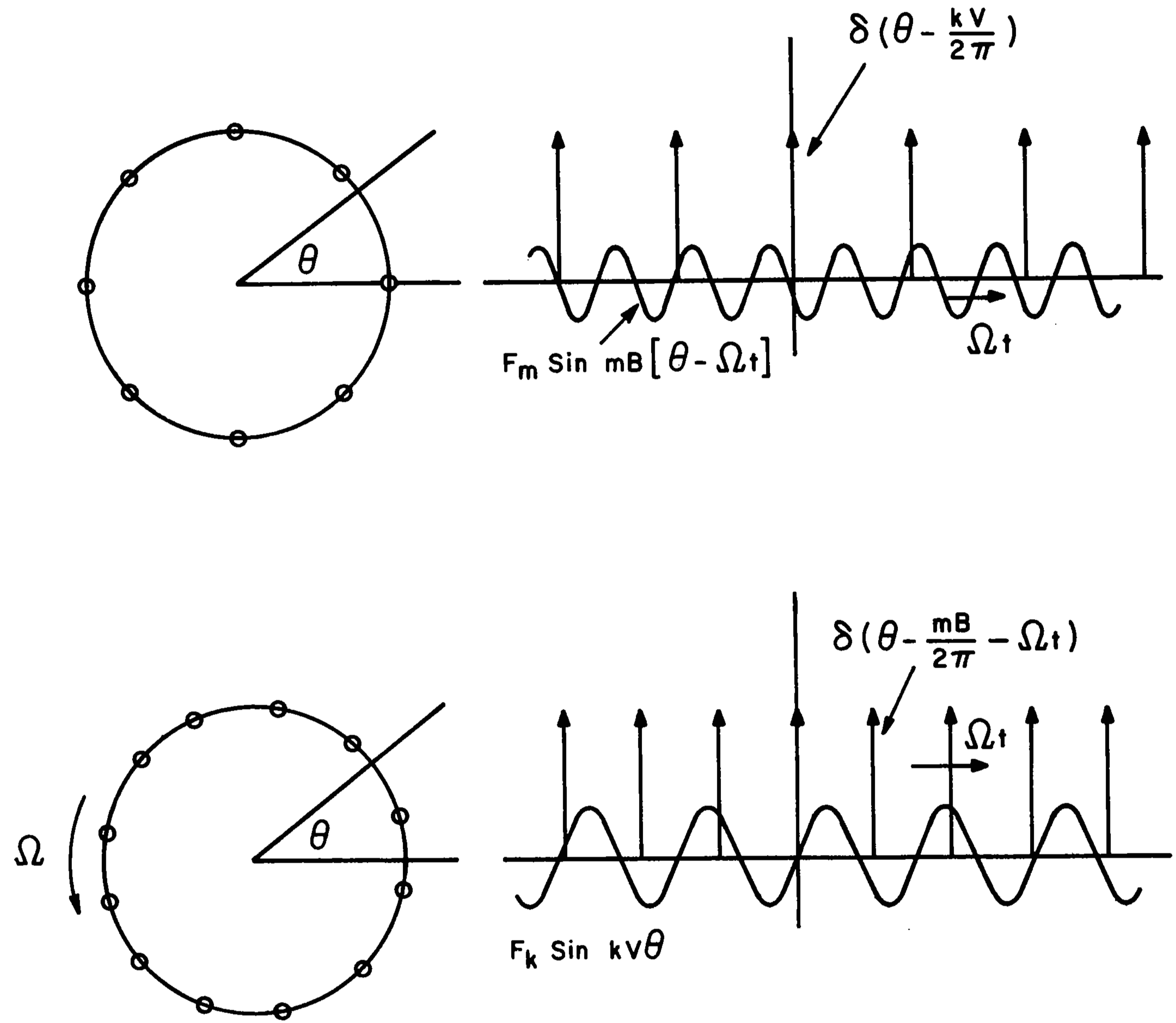

FIG. 3. "POINT-SOURCE" MODEL FOR ROTOR/STATOR RADIATION INTO FREE-FIELD ENVIRONMENT

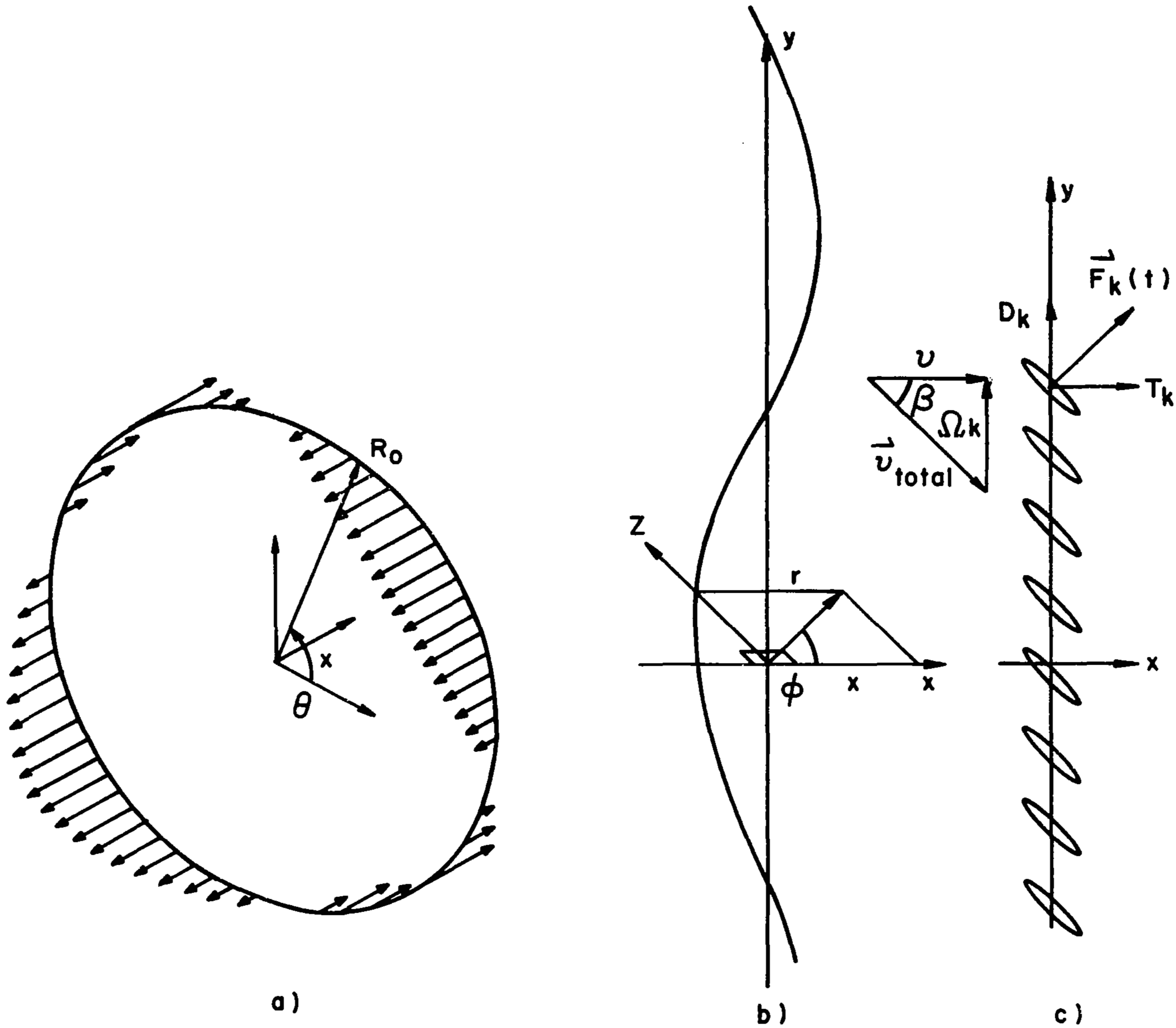

FIG. 4. SPINNING THRUST MODE

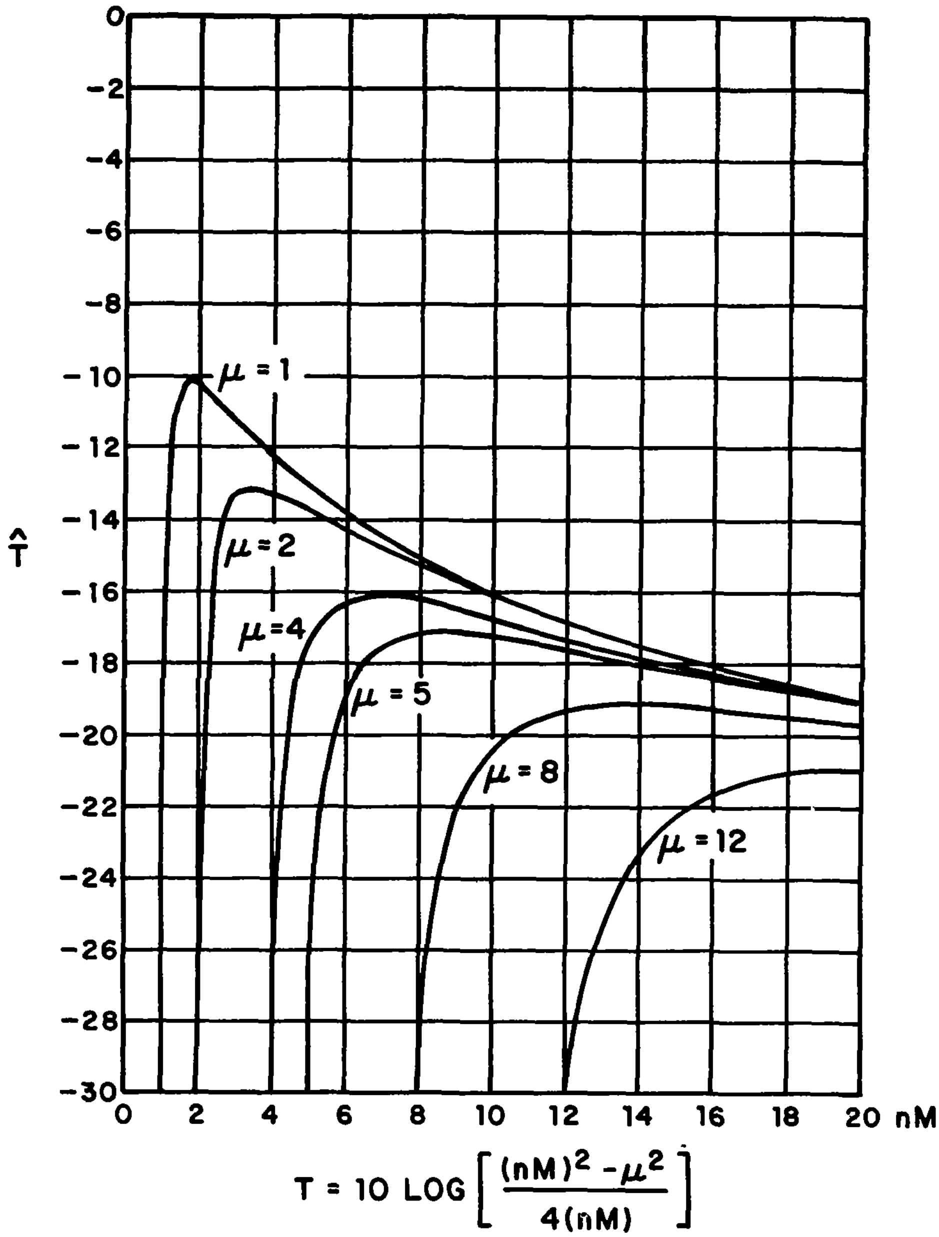

FIG. 5. CONTRIBUTIONS OF THRUST TERMS TO POWER (APPROXIMATE SOLUTION)

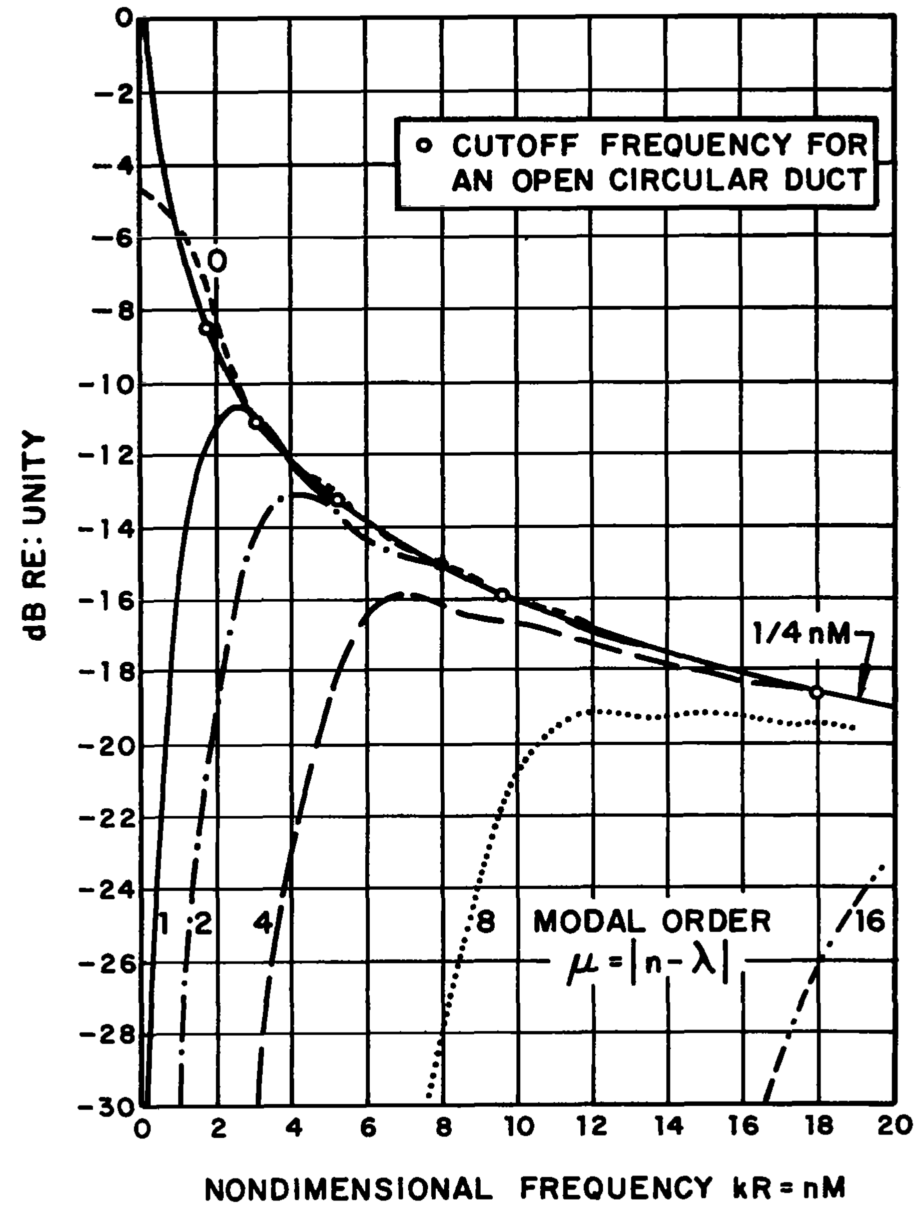

FIG. 5. CONT: CONTRIBUTION OF THRUST TERMS TO POWER (EXACT SOLUTION AFTER LOWSON – REFERENCE 2)

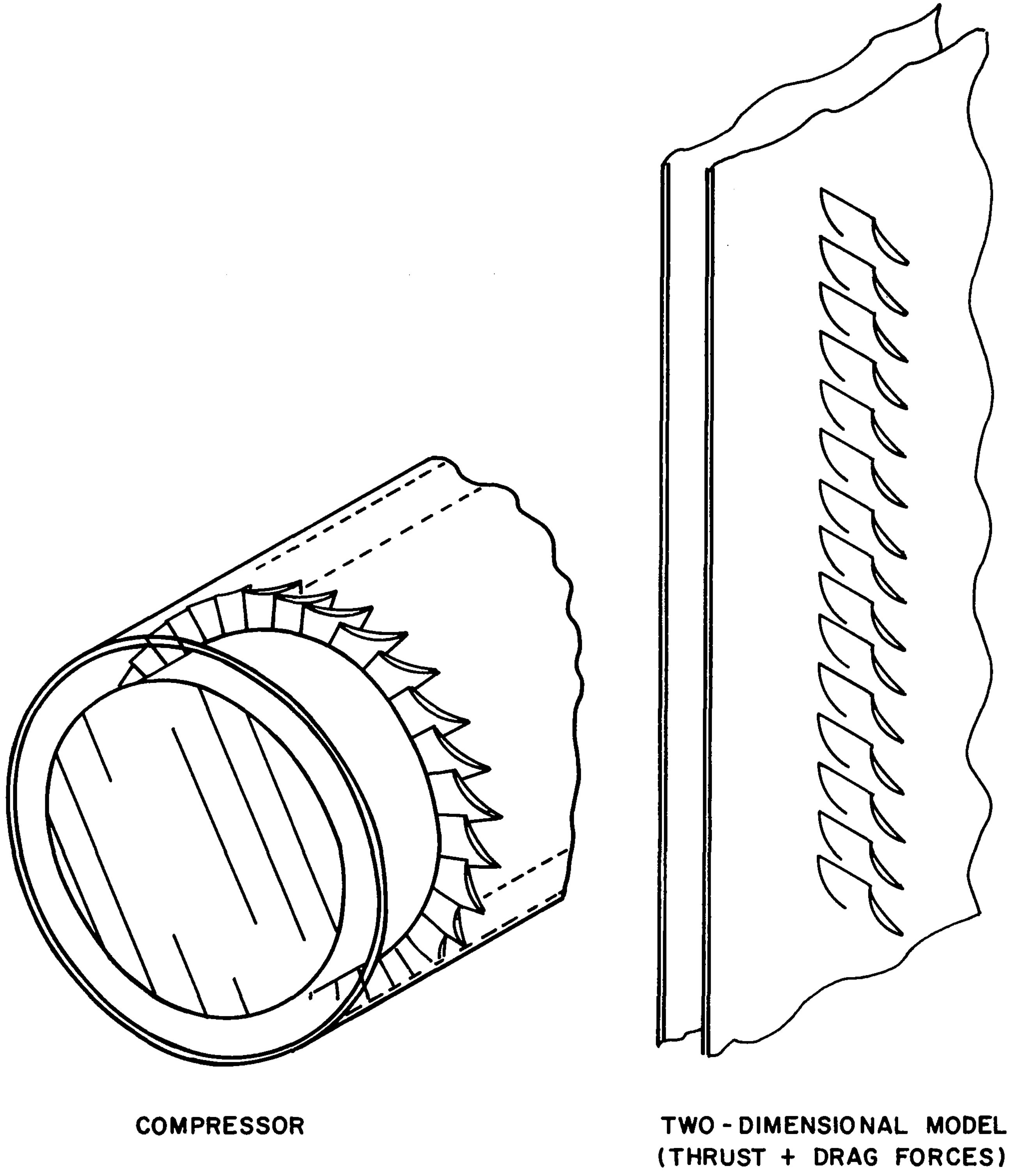

FIG. 6. ROTOR IN NARROW SEMI-INFINITE DUCT AND TWO-DIMENSIONAL ANALOG

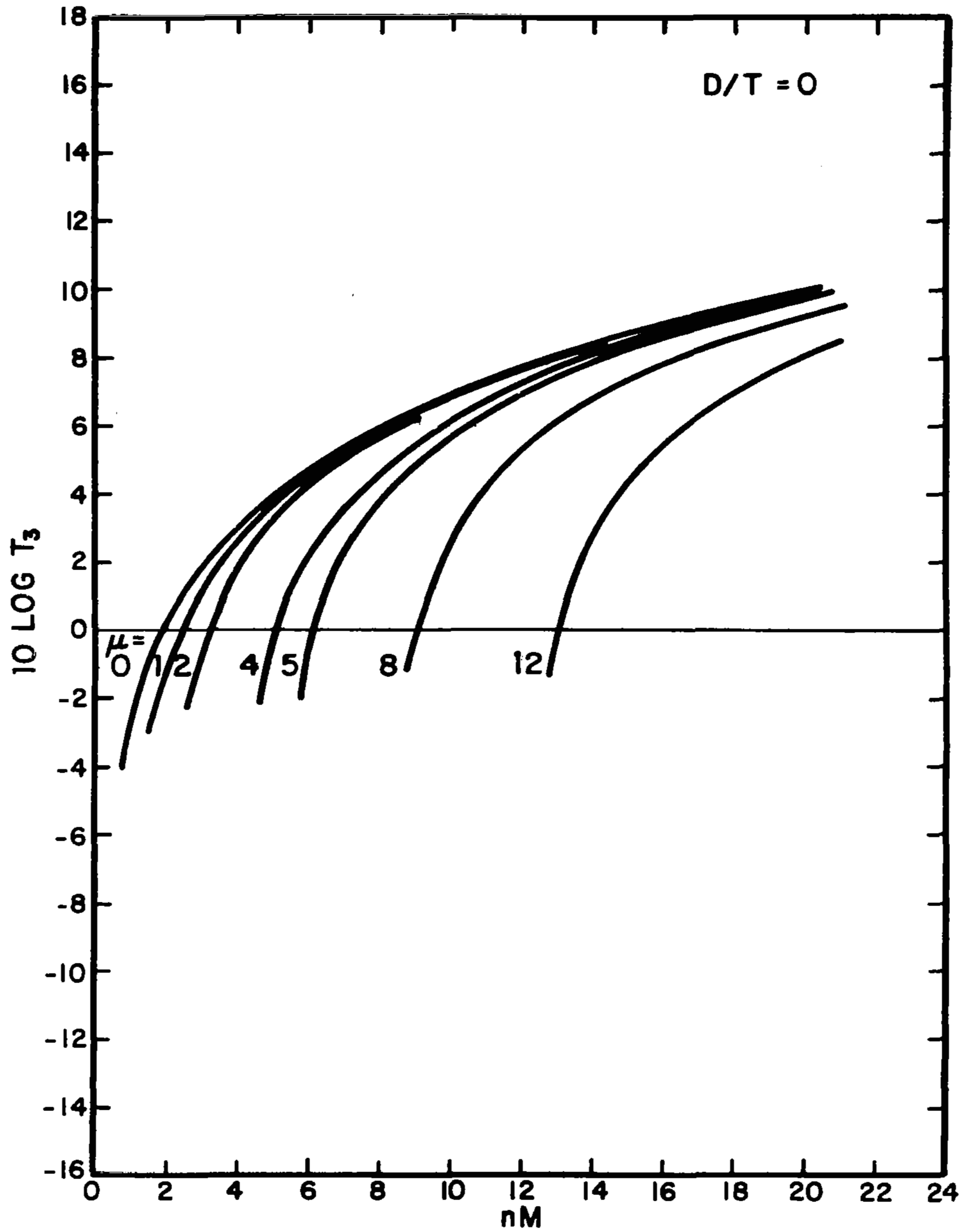

FIG. 7. T_3 (FROM TABLE II) AS FUNCTION OF FREQUENCY PARAMETER nM AND MODAL ORDER

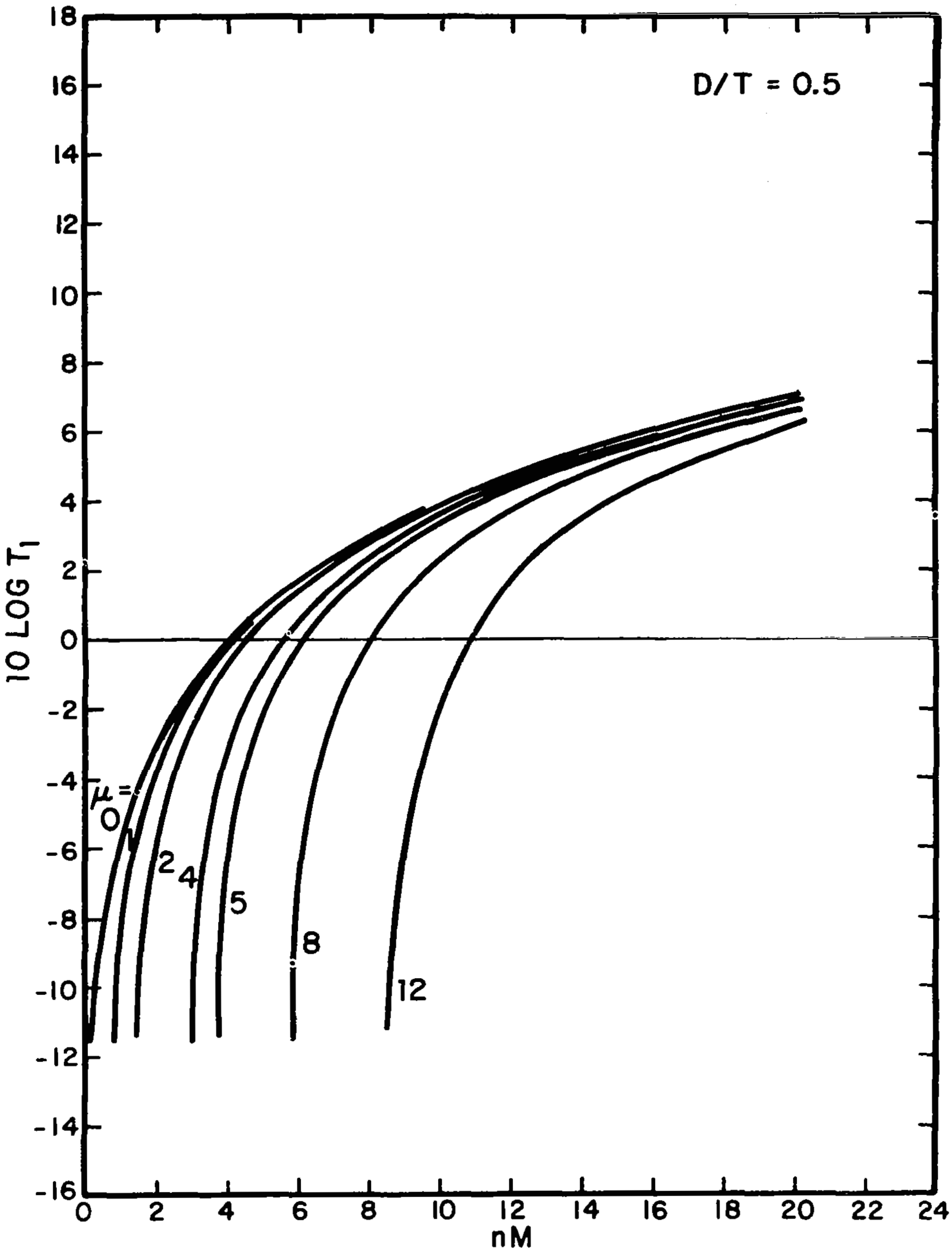

FIG. 8a. T_1 (FROM TABLE II) AS FUNCTION OF FREQUENCY PARAMETER nM AND MODAL ORDER

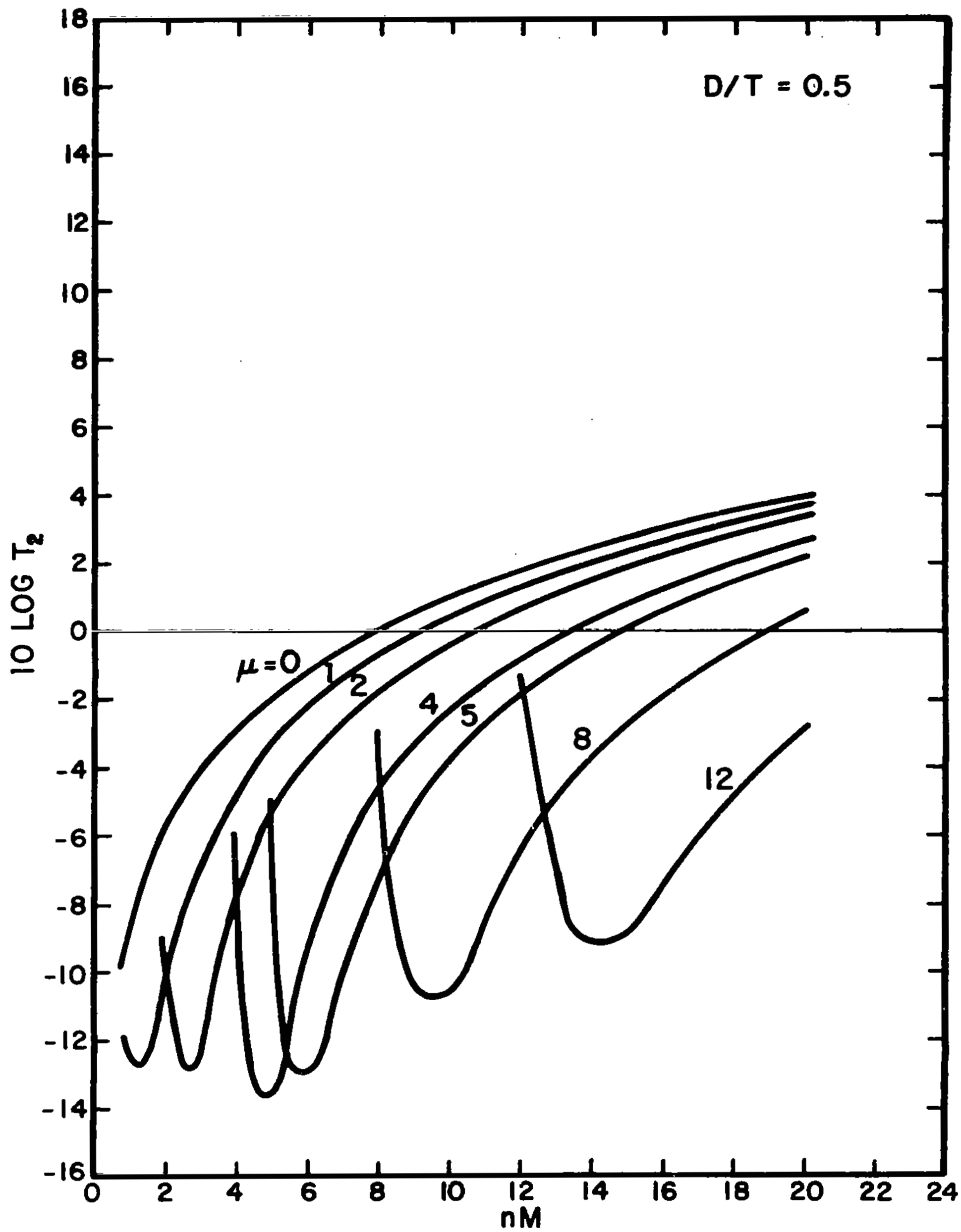

FIG. 8b. T_2 (FROM TABLE II) AS FUNCTION OF FREQUENCY PARAMETER nM AND MODAL ORDER

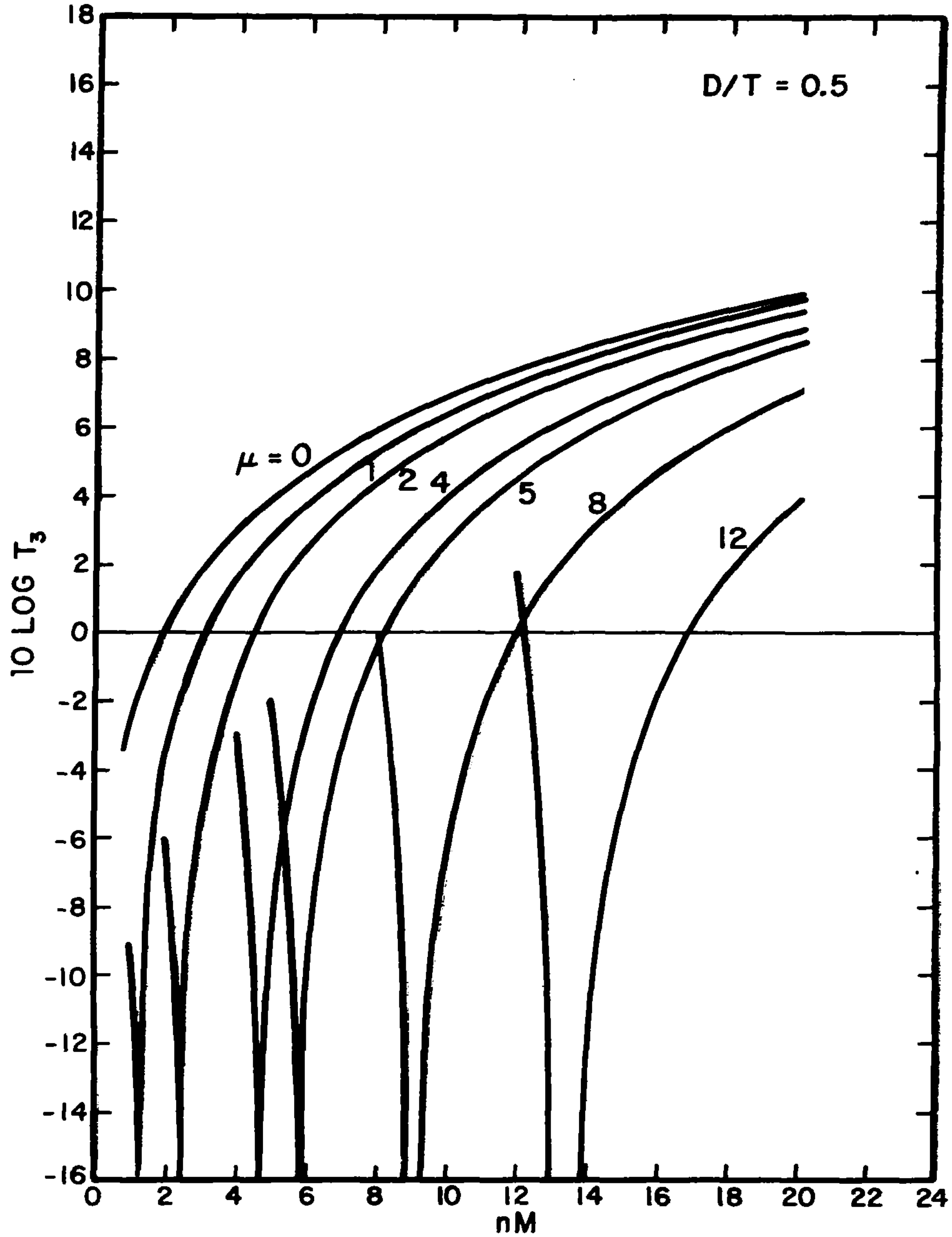

FIG. 8c. T_3 (FROM TABLE II) AS FUNCTION OF FREQUENCY PARAMETER nM AND MODAL ORDER

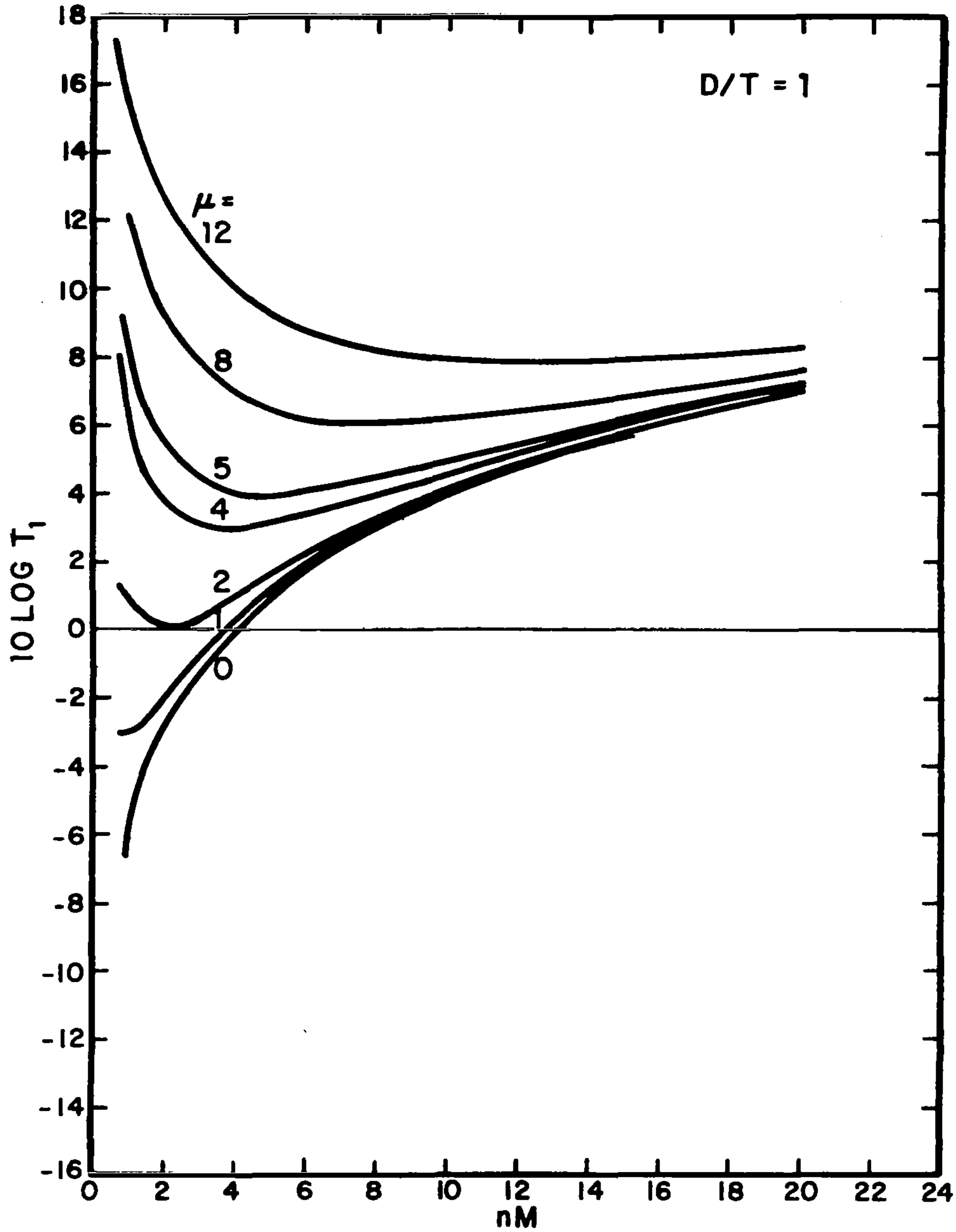

FIG. 9a. T_1 (FROM TABLE II) AS FUNCTION OF FREQUENCY PARAMETER nM AND MODAL ORDER

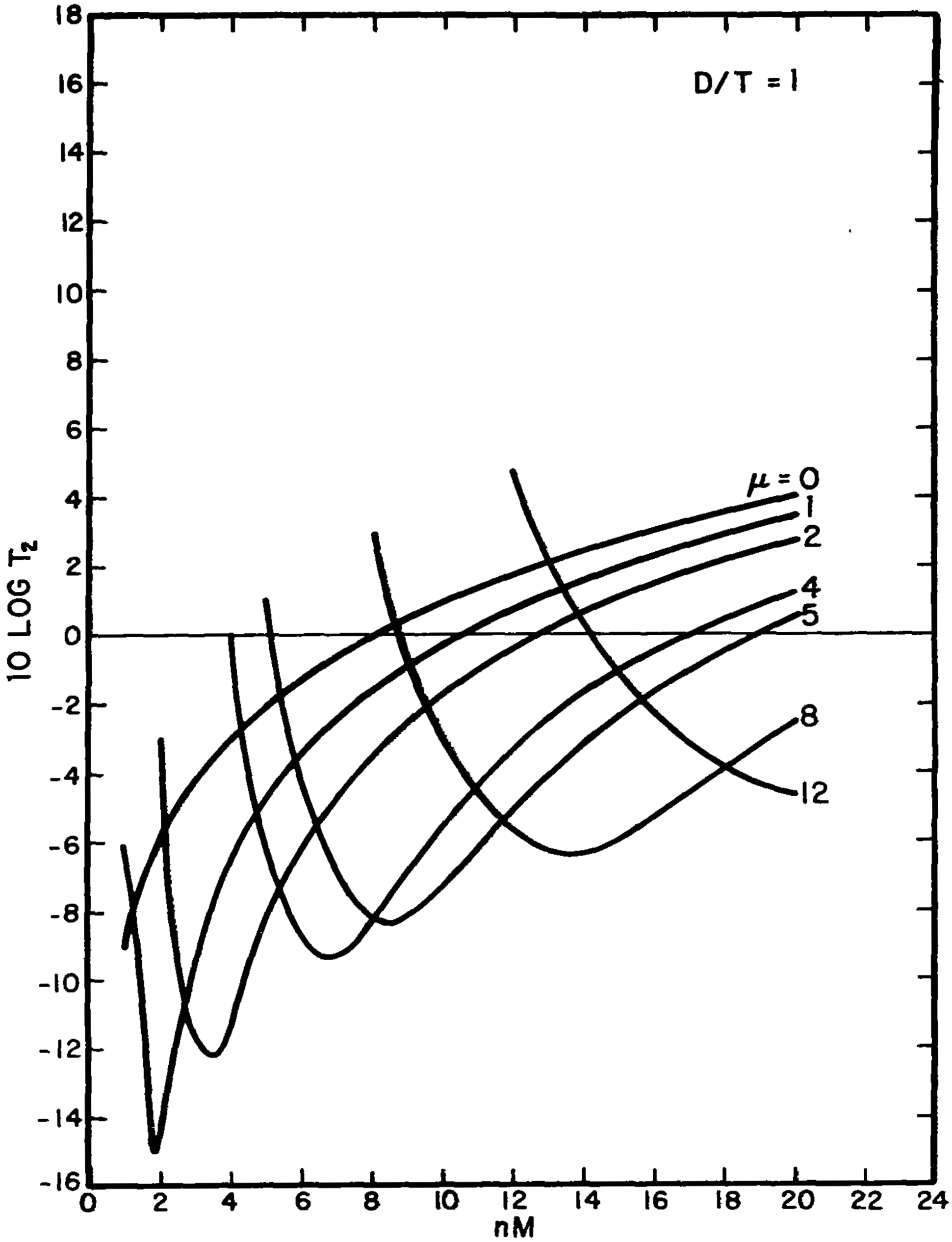

FIG. 9b. T_2 (FROM TABLE II) AS FUNCTION OF FREQUENCY PARAMETER nM AND MODAL ORDER

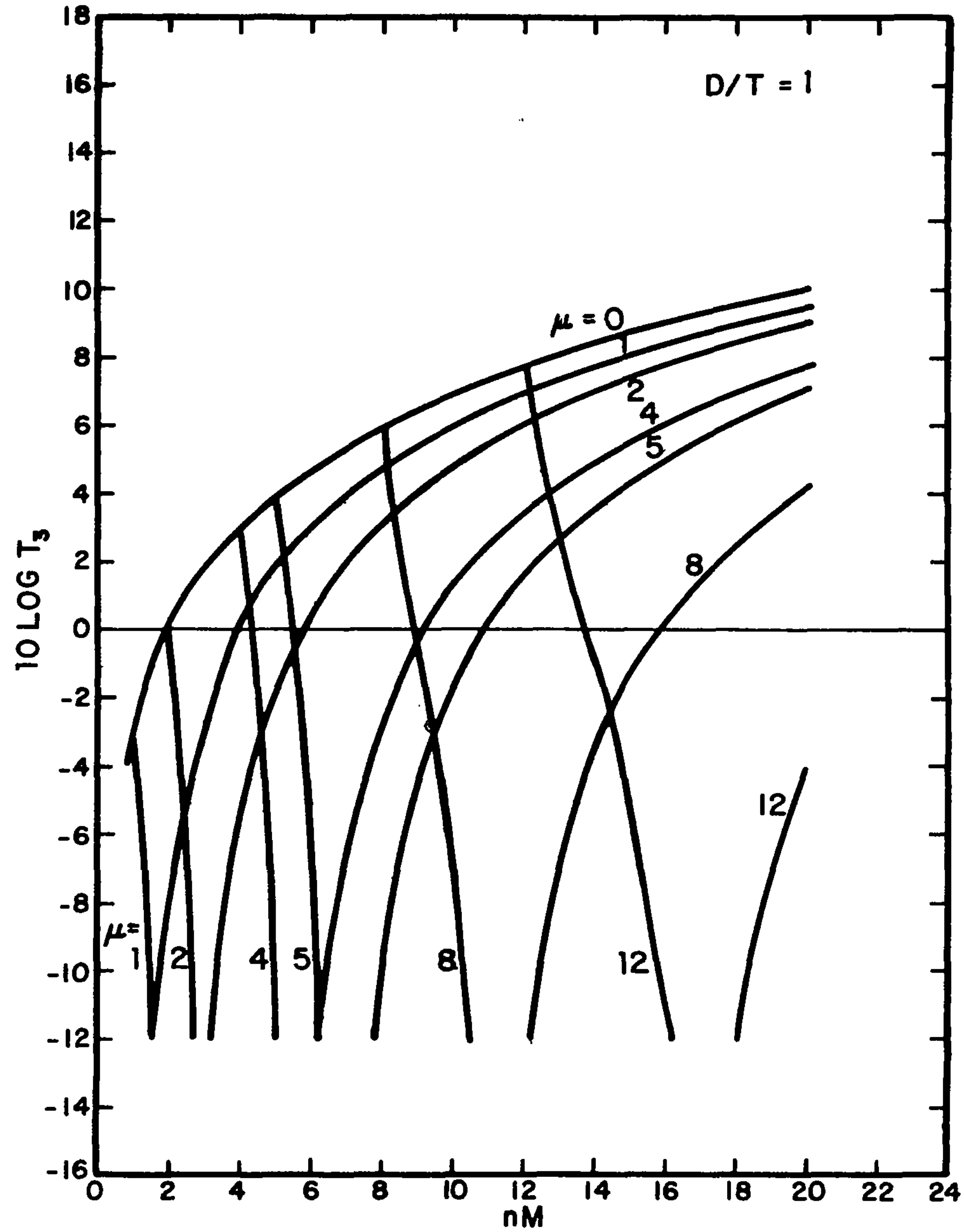

FIG. 9c. T_3 (FROM TABLE II) AS FUNCTION OF FREQUENCY PARAMETER nM AND MODAL ORDER

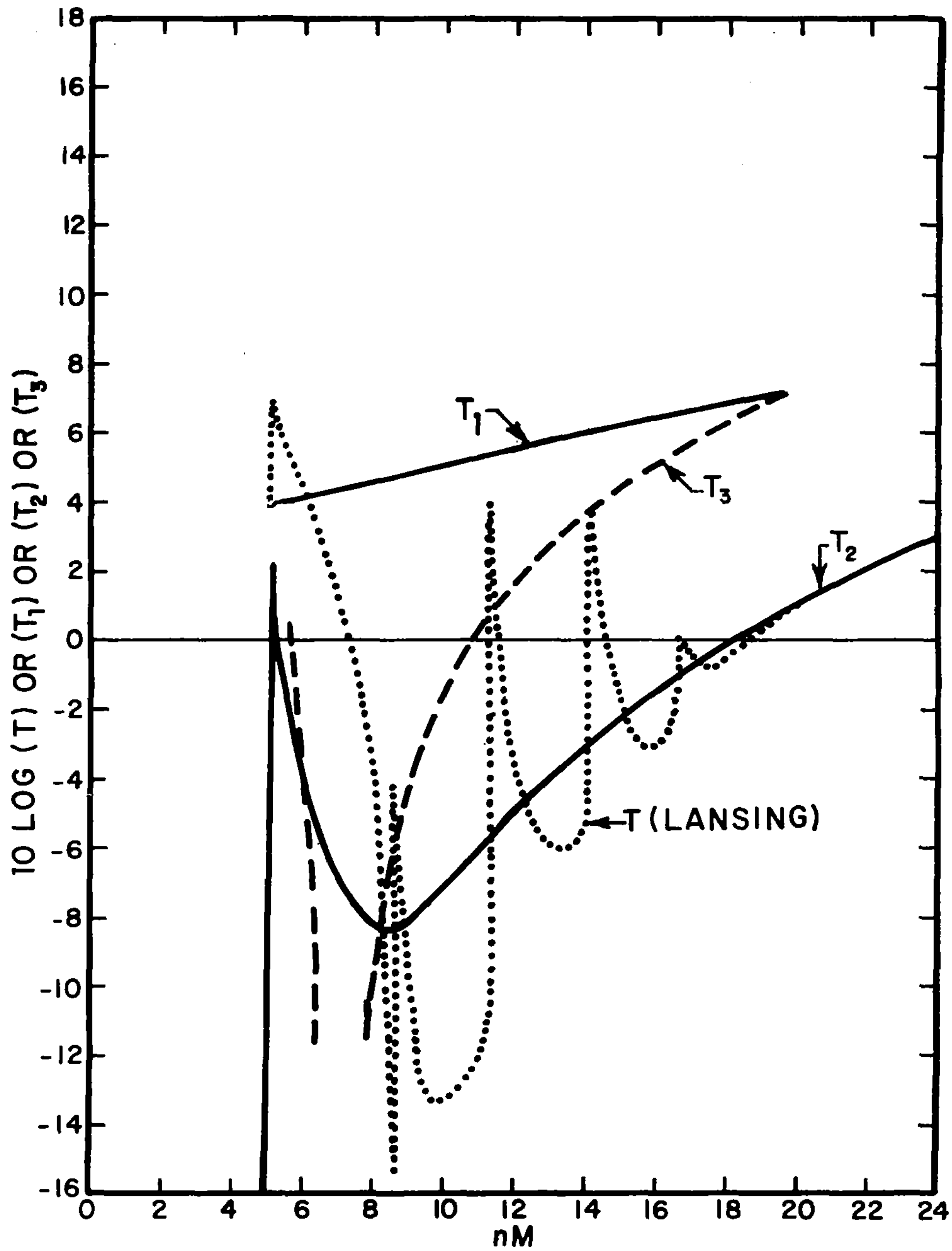

FIG. 10. LANSING'S RESULTS (REPLOTTED ACCORDING TO NOTATION OF PRESENT REPORT) IN COMPARISON TO T_1, T_2 AND T_3 DEVELOPED IN PRESENT ANALYSIS $\mu = 5$; D = 0.94T

III. EXPERIMENTS

A. Introduction

The objectives of the experiments were twofold: (1) to prove the feasibility of measuring fluctuating forces over a wide frequency range on rotating airfoils, using specially developed transducers and telemetry techniques, and (2) to correlate the measured fluctuating forces with the measured sound on the basis of the various theoretical models. While the first objective has been fully achieved, the second had to be curtailed to a few "spot-checks" at experimental conditions that were not always favorable for the case under consideration. Thus, experiments on discrete tone radiation could be conducted only at relatively low values of the basic frequency parameter, nM. This range is characterized by rather drastic changes in the nondimensional parameters T_1, T_2, or T_3, as shown in Figs. 7-9, thus requiring accuracies of sound power measurements that are difficult to obtain in realistic acoustic test rooms. Furthermore, it was difficult to separate thrust and drag components of the measured unsteady forces on the rotor blade, since the effective angle of flow incidence on the rotor blades could not be determined with sufficient accuracy. The measurements and the obtained results should thus be considered as representative.

The experimental program was divided into measuring: (1) discrete frequency forces on blades and corresponding sound radiation, and (2) broadband forces and sound radiation. Several configurations were tested, in particular, a single rotating blade, a single multibladed rotor, a single rotating blade downstream of a multibladed stator, and a multibladed rotor downstream of a multibladed stator. Only for the latter configuration were narrowband measurements of forces and sound obtained; all other configurations were tested for broadband behavior.

B. Force Measurement Technology

1. Approach

There are basically two ways to measure forces on blades: (1) by means of a force-balance *at the root of the blade,* which would provide the moment on the blade, or (2) by means of individual force-sensors *on the blade,* whose output must be integrated to obtain a measure of the total force. The disadvantage of the first approach is that signals are strongly affected by blade bending. The disadvantage of the second approach is the practical limit in numbers of sensors that can be placed on a blade; chances are that information between sensors and directly at leading and trailing edges, as well as at the blade-tip region where sensors cannot be placed, will be lost. However, it was felt that, in general, the second approach would yield more accurate results, especially in the frequency range above the first bending mode frequency, and was adopted for this reason.

2. Sensors

Although the use of strain-gauge sensors would have allowed the acquisition of both steady and unsteady data, their well-known physical delicacy and their sensitivity towards temperature changes disqualified them for the envisioned purpose. We therefore developed and fabricated special differential-pressure piezo-electric *microphones** that were inserted into the blade proper; they measured the local differential pressure, which is proportional to the local force. Thus, steady forces could not be measured; however, the major objective of the research program was the study of unsteady forces on rotor blades in a wide frequency range and acquisition of steady-force data was not considered in the context of the present study.

C. Test Set-up

1. Rotor

Figure 11a shows the basic rotor configuration. One rotor blade is attached to a hollow experimental hub. Depending on the test requirements, up to nine additional rotor blades could be attached to the hub. To avoid the mechanical and electrical problems associated with sliprings, we used telemetry† to transmit the signals from the rotating blade to the stationary recording and analyzing equipment. Inside the hub (Fig. 11b) is the FM transmitter as well as power supplies for the transmitter and for the blade-mounted sensors.

---

* Considerations concerning the development of the differential pressure sensor and specifications are presented in Appendix D.

† Specifications of the BBN FM transmitter are presented in Appendix E.

The hub is connected to a variable-speed motor that allows rotational speeds up to 4000 rpm. Accessible from the outside are switches and a connector bridge, at which individual sensors can be connected to the transmitter.

2. Instrumented blade

The blade (NACA 6409 profile) had a 2.82-in. span and 1.475-in. chord. Twist angle from root to tip changed by 20°. Since this blade was designed to operate in a compressor with a hub diameter of about 2 ft, using the blade on a hub of only 6-in. diameter resulted essentially in an "off-design" operation. However, this fact was not considered detrimental since the basic relationship between fluctuating forces and radiated sound was not expected to depend on the blade operating at a design condition. Figure 12 shows the blade with six sensors.

3. Sensors

Of the six sensors, five were differential-pressure sensors and one a single-sided* sensor. Sensor diameter is 0.25 in., sensor thickness 0.1 in. Each sensor has two diaphragms, facing different sides of the blade (Fig. 13). The diaphragms are supported by piezo-electric crystals whose output is fed to a common internal preamplifier that uses an FET circuit to convert the original high-impedance signal into a low-impedance signal. Polarization of the crystals is such that the sensor output is proportional to the pressure difference rather than to the sum of the pressures. The sensors were spaced on the blade as far apart as possible, within the constraints of the blade surface contour. The diaphragms were covered with an RTV heat-shield material that was faired to the contour of the blade surface.

---

* In order to interpret correctly the signals of the differential sensor, one needs information on the absolute pressure on at least one side of the blade, since a systematic error depends on the ratio of differential pressure to single-sided pressure, as outlined in Appendix F. Since only order-of-magnitude information on the absolute pressure is necessary to determine the correction factor, one single-sided transducer was considered to be sufficient.

4. Data acquisition

Signals coming from each sensor are fed into the (hub-internal) telemetry unit and transmitted to a commercial receiver. The hub-located broadcasting antenna is of circular shape to avoid any Doppler effects. Receiver response was changed to be flat over the audio-frequency range. Transmission frequencies varied somewhat depending on the supply voltage for the transmitter, but were always within the RF-bands (88 to 104 MHz). Signals were strong enough to override any nearby radio station. Signals were then fed either into a General Radio Real Time 1/3 Octave Band Analyzer via a GR-Sound Level Meter (for amplification) and further into an X-Y Plotter (BBN Model 800), or into a General Radio 1%-Bandwidth Filter and to a General Radio Level Recorder. Signal time-history and "instantaneous" one-third octave band spectra could be observed on oscilloscopes, one after the receiver, one before the X-Y Plotter. Figure 14 presents a schematic of the data acquisition system.

The output of the Real Time Analyzer is a one-third octave band spectrum of the local differential pressure, integrated over the transducer surface. Since the amplitude of the signal fluctuated substantially at low frequencies, a 16-sec-integration time was considered necessary to average such fluctuations. For the narrowband analysis (using the 1% GR analyzer), the differential pressure signal at frequencies of interest was averaged by hand from a time history trace over several seconds.

Since differential pressure is measured as force per unit area, forces can be computed by reference to an appropriate area. We will see later on that assessment of the effective area is somewhat speculative because differential-pressure spectra on a blade vary significantly from location to location. Also, questions of force-field coherence at high frequencies enter the problem.

5. Test room

The rotor assembly was located downstream of the exhaust opening of BBN's open-jet, quiet wind tunnel (Fig. 15). (This flow facility is located in a reverberant room so that diffuse field sound power measurements can be obtained.) Thus, either flow could be superimposed on the motor-driven rotor, or the rotor could be driven by the airstream. Acoustic data were obtained through a B&K 1-in. diameter microphone that was moved around in the reverberant room during the integration time of the Real Time Analyzer to improve spatial averaging. Sound pressure levels were then converted into sound power levels, using standard techniques.

6. Test procedure

Before each test, the transmission frequency was adjusted to the best signal strength. Thereafter, all transducers were calibrated with a pistonphone. Electronic and acoustic noise floors were frequently determined. For a given operational condition, differential pressure spectra from each sensor were measured, and the acoustic power spectrum determined. Data reduction procedures will be discussed in the following sections.

D. Results

1. Discrete frequency investigation

Loading and Radiation Parameters

Before we present any experimental data, we recapitulate the important parameters for the analysis of discrete-frequency loading and sound radiation.

The loading of a rotor due to the periodic wake field of an upstream multibladed stator is characterized by the source input harmonic λ, equal to kV, where k — the order of the input harmonic — is an integer and V is the number of stator blades. λ thus determines the loading harmonic for each rotor blade.

Sound radiation from the rotor is related to the sound harmonic number n, equal to mB, where m — the order of the sound harmonic — is an integer and B is the number of rotor blades. Sound radiation at the blade passage frequency is determined by $m = 1$.

The two most important parameters for the sound radiation are (1) the frequency parameter $nM = mB \cdot M$, where M is the rotational Mach number $\Omega R/c$, and (2) the modal order $\mu = |mB - kV|$. The dimensionless quantities T_1, T_2 and T_3 of the analyses presented in Chapter II were plotted as functions of these two parameters.

For the case of a rotor downstream of a multibladed stator, each rotor blade is subjected to kV loading harmonic impulses per revolution. Each time a rotor blade is in line with a stator blade (roughly speaking), a (acoustic) pressure pulse is emitted of a frequency mB (the sound harmonic number). The speed with which the pressure pulse travels around the blade ring depends on the number of rotor and stator blades and on the rotational speed; this phase speed is given by

$$\Omega_{eff} = \left|\frac{mB\ \Omega}{mB-kV}\right| ,$$

where Ω is the angular velocity. Only when the phase speed is supersonic can sound travel away from the source region; otherwise the rotor/stator configuration represents a very inefficient radiator. Theoretically, subsonic phase velocity in a compressor results in zero sound output. In real compressors, there is sound radiation, but it is extremely small.

Data Presentation

In this section we describe experimental results pertaining to the measurement of (discrete) loading harmonics on the rotor due to the periodic stator wake. The rotor was driven by the air flow and thus operated in a "turbine mode", rather than as a compressor. The configuration was not shrouded*, so that sound radiated unobstructed into the free-field environment.

The configuration is shown in the photograph (Fig. 16); the rotor has 10 blades and the (upstream) stator has 9 blades.

By adjusting the speed of the air flow that drove the rotor, various rotational speeds were obtained, in particular, 1520 rpm (25.3 rps), 2260 rpm (37.7 rps), and 3000 rpm (50 rps).

Table III lists for these rotational speeds, (1) the phase speed of the source pattern for various combinations of m and k, (2) the loading harmonic order, λ = kV, and the loading harmonic frequency, and (3) the sound harmonic number n = mB, radiation modal order $\mu = |mB-kV|$, and the radiation frequency.

---

* Justification for studying an unshrouded "compressor" is that many current jet engines have duct lengths of less than a diameter, so that duct effects would play a minor role.

TABLE III: COMPRESSOR LOADING AND RADIATION PARAMETERS

Order of Compressor Sound Harmonic m	Order of Source Input Harmonic k	Phase Speed (ft/sec) $\frac{mB\Omega}{\lvert mB-kV \rvert}$			Loading Harmonic Order $\lambda=kV$	Loading Harmonic Frequency $k V\Omega/2\pi R$ (Hz)			Sound Harmonic Number $n=mB$	Modal Order for Radiation $\mu=\lvert n-\lambda \rvert = \lvert mB-kV \rvert$	Radiation Frequency $mB\Omega/2\pi R$ (Hz)		
		Rev/Sec				Rev/Sec					Rev/Sec		
		25.3	37.7	50		25.3	37.7	50			25.3	37.7	50
1	1	800	1200	1570	9	230	340	450	10	1	253	377	500
2	1	145	216	285	9	230	340	450	20	11	506	754	1000
1	2	100	150	200	18	460	680	900	10	8	253	377	500
2	2	800	1200	1570	18	460	680	930	20	2	506	754	1000
3	1	114	170	225	9	230	340	450	30	21	759	1131	1500
3	2	200	300	400	18	460	680	900	30	12	759	1131	1500
1	3	47	70	92	27	690	1020	1350	10	17	253	377	500
2	3	228	340	450	27	690	1020	1350	20	7	506	754	1000
3	3	800	1200	1570	27	690	1000	1350	30	3	759	1131	1500

Supersonic phase speeds for this particular rotor/stator configuration occurred only at the two higher rotational speeds and only when the orders of source input harmonic and sound harmonics, m and k, were equal. Any other combination of m and k results in a very low subsonic phase speed.

Narrowband spectra (1% bandwidth) were obtained from each blade sensor for the three RPMs listed above. Simultaneously, narrowband pressure-level spectra of the radiated sound from the rotor were measured. A set of representative traces in the frequency range covering the first few input harmonic frequencies and sound radiation frequencies is shown in Fig. 17. Rotational speed was 3000 rpm, the highest rpm that was tested. The top two traces represent fluctuating differential pressure spectra obtained from sensor #1 (tip location near trailing edge) and sensor #6 (root location, near leading edge). There was more broadband "noise" available at the blade tip location (upper trace) than at the root of the blade (lower trace), indicating that higher random forces – perhaps due to vortex shedding – were acting on the tip than on the root. The discrete peaks at 460 Hz, 930 Hz, and 1380 Hz correspond approximately to loading *harmonic orders* λ *of 9, 18, and 27. The peaks in the sound* pressure level spectrum at 500, 1000, 1500, and 2000 Hz correspond to sound harmonic numbers n of 10, 20, 30, and 40.

These radiation and loading harmonics correspond to combinations of sound radiation and source input harmonic orders $m = k = 1$, $m = k = 2$, and $m = k = 3$, for which phase speeds are a maximum, as evident from Table III. Other listed combinations of m and k lead to much lower phase speeds, well below sonic speeds, and will not be considered further, since sound radiation at corresponding frequencies should be and was observed to be minimum. Also, from the Table, one should expect efficient sound radiation for modal orders of 1, 2, and 3 only for the two higher RPMs, since the lowest one always results in phase speeds below sonic. This is confirmed in Fig. 18, where the *power* levels of the discrete sound radiation from the stator/rotor configuration at several rotational speeds* are plotted, for radiation modal orders μ of 1, 2, and 3. The figure indicates the region of subsonic phase speed for each modal order. Clearly, the power level increases drastically as the phase speed increases (towards the right in Fig. 18) for a particular modal order.

---

* Not all of which are listed in Table III.

From traces similar to those shown in Fig. 17, the discrete harmonic-loading levels (in terms of differential pressure levels) at various locations on the blade were determined. Table IV presents the differential pressure levels in dB relative to 0.0002 μbar, at loading harmonic orders λ = 9, 18, and 27 for four sensors. The latter ones can be related to the radiation at corresponding sound harmonic numbers n = 10, 20, and 30. The differential pressure levels observed at the four sensor locations were averaged together under the assumption of full coherence of the force field on the blade and plotted versus loading harmonic frequency in Fig. 19. To arrive at the total force, the force per unit area was multiplied by the total blade area (26 cm), again assuming full coherence of the force field over the entire blade area – an assumption that is very likely not true at higher frequencies, where the hydrodynamic wavelength becomes smaller than typical blade dimensions. The radiated power in the *nth* sound harmonic due to the λ*th* harmonic source input is given by (see Table II)

$$\Pi_{n\lambda} = \frac{B^2}{8\pi R_0^2 \rho c} T_\lambda^2 \cdot T_1 \quad ,$$

where T_1 was defined in the previous chapter.

T_λ is the total force on the blade due to the loading harmonic of order λ in the "thrust direction".

Assuming that T = D, or T/D = 1, and that the fluctuating force vector acted at right angles on the blade, T (and hence D) was assumed to be about 70% of the measured total force on the blade.

Table V summarizes the results for the tone radiation due to harmonic loads on the rotor. Results are presented for the three rotational speeds that were tested. In the last column, measured sound power levels at the sound harmonic number and those predicted using the measured average total force at the corresponding harmonic loading frequencies are compared.

The agreement is acceptable, although there seems to be a trend of over-predicting levels at low rotational speeds and under-predicting levels at high speeds. However, at low rotational speeds, the phase speed was subsonic and hence the efficiency of radiation was quite small. At the higher rotational

TABLE IV: DIFFERENTIAL PRESSURE LEVELS IN dB re 2×10^{-4} μBAR FROM VARIOUS SENSORS ON ONE BLADE, WHEN THE TEN-BLADED ROTOR ROTATES DOWNSTREAM OF A NINE-BLADED STATOR.

RPM/rps	Loading Harmonic Order	Loading Harmonic Frequency (Hz)	Differential Pressure Level dB re 2×10^{-4} μ bar at Sensor No.			
			1	2	5	6
1580/25.3	9	230	121	117	101	113
	18	460	113	116	·/.	117
	27	690	·/.	100	·/.	·/.
2260/37.7	9	345	125	119	113	92
	18	·/.	·/.	·/.	·/.	·/.
	27	1190	·/.	·/.	109	·/.
3000/50	9	465	123	118	·/.	124
	18	930	117	·/.	·/.	118
	27	1400	114	·/.	·/.	·/.

·/. no data obtained

TABLE V: MEASURED AND PREDICTED SOUND POWER LEVEL RADIATION OF MODAL ORDER μ DUE TO LOADING HARMONIC ORDER λ FOR D/T = 1

Modal Order of Radiation μ	Loading Beam Order λ	Frequency Parameter nM			Total Force Per Unit Area (dyn/cm²)			Sound Power Level, dB re 10^{-12} watt meas./pred.		
		Rev/Sec			Rev/Sec			Rev/Sec		
		25.3	37.7	50	25.3	37.7	50	25.3	37.7	50
1	9	0.71	1.05	1.4	120	200	250	76 / 79.5	87 / 84.5	96 / 87.5
2	18	1.42	2.1	2.8	120		150	77 / 84	84 / **	92 / 86
3	27	2.13	3.15	4.2	20	55	100	* / 70	76 / 78	88 / 84

* no sound measurements obtained
** no force measurements obtained

speeds, there was probably some interaction of the potential field around the rotor with the upstream stator that generated additional sound which cannot be related to forces on the rotor. Also, D and T were probably not equal as assumed in interpreting the data.

2. Broadband investigation

Introduction

In the following, one-third octave band spectra – both for rotor blade forces and radiated sound – will be presented for a variety of configurations and discussed in a more general way.

Table VI lists the five experimental configurations that were tested. In all cases, rotor blade and stator blade angles were identical – 79° at the tip and 53° at the root for the blade with respect to the axis – the concave side of the rotor blade faced downstream, and the upstream stator blades were oriented so that their mean chord was parallel to the rotor axis.

TABLE VI: EXPERIMENTAL CONFIGURATIONS

B	V	U (ft/sec)	RPM	
1	0	0	2000, 3000, 4000	driven
1	0	70	2000, 3000, 4500	by
10	0	0	2000, 3000	motor
10	0	70	2400	driven by
10	9	70	2100	airflow

In Table VI B is the number of rotor blades and V the number of stator blades; U is the speed of the superimposed flow from the tunnel orifice. V = 0 indicates the absence of the stator. RPM is the rotational rate with which the rotor was driven by the motor or with which the rotor spun because of superimposed flow; in this latter case, the rotor was not driven by the motor.

Data Presentation and Discussion

For each experimental configuration, one-third octave band spectra were obtained from sensors* 1, 2, 4, 5, and 6, all of which are differential-pressure sensors. Frequently, there was a substantial variation in differential pressure levels (DPL) over the blade, indicating that flow over the blade was nonuniform with attached or separated fields. Figure 20 is an example of a large variation in DPL spectra: DP levels vary as much as 15 dB over the blade. Here the single-bladed rotor was driven by the motor.

Figure 21 shows a case of DPL variation that is relatively small (on the order of 3 dB), especially at higher frequencies. Here, the 10-bladed rotor was driven by the airflow at a rotational speed of 2400 rpm. It is believed that the amount of variation between individual DPL spectra on the blade is a measure of how far off-design the blade operates under a particular experimental condition. Largest "scatter" was always observed when the rotor was driven by the motor; data spread was substantially reduced when the rotor was driven by the airflow in which cases the rotor selected the appropriate rotational speed corresponding to a "design situation".

For data interpretation, all five DPL spectra were averaged over the blade surface under the assumption of full coherence of the differential pressure field: thus,

$20 \log \{[\sum_{i=1}^{i} \Delta p_i(f)]/n\}$ was determined in each case and plotted

versus the one-third octave band center frequency f; here $\Delta p_i(f)$ is the differential pressure measured through sensor i at the frequency *f* and *n* is the number of sensors. All DPL spectra shown in Figs. 22 through 26 were obtained in this manner.

---

* Sensors 2, 4, and 6 were close to the leading edge, and sensors 1, 3, and 5 close to the trailing edge, going from tip to root. Sensor 3 was the single-sided sensor.

To convert the averaged differential pressure spectra into force spectra, they were multiplied with the total* blade area A; thus, "fully coherent" force spectra were obtained by plotting

$10 \log \{[\sum_{i=1}^{i} \Delta p_i(f)]A/n\}$ versus one-third octave band center frequency.

Force-level spectra were then converted into sound power level spectra (using the analytical expression for free-field dipole radiation – Table I) and compared to measured sound power level spectra.

One of the shortcomings of the experimental technique is the limited number of DP sensors that could be placed on the blade. As discussed previously, vital information near the leading and trailing edges and near the blade tip could not be obtained, so that conclusions on the total fluctuating force (in frequency bands) imposed by the blade onto the surrounding medium and radiated as sound are somewhat speculative.

In general, however, the behavior of the DPL spectra is reflected in the behavior of the radiated sound power level (PWL) spectra; for example, if in a particular experimental configuration the differential pressures increase when flow is superimposed, the radiated sound power also increases. This behavior confirms the expected interrelationship of differential pressures (or, equivalently, forces) and radiated sound.

For the broadband radiation, the issue of phase speed does not enter, since the entire rotor disk or rotor/stator configuration acts as a broadband source. The fact of rotation (at least at those rotational speeds investigated, which never exceeded a Mach number of 0.25) is unimportant in this context.

---

* Since no information on the coherence of the force field on the blade is available, the *total* blade area was used to convert measured pressure spectra into force spectra. However, the force field is likely to lose coherence at higher frequencies; in this case, forces cancel locally on the blade and less sound is radiated. Hence, an indirect measure of the coherence of the force field on the blade is the deviation of the predicted sound power from the measured one.

Figures 22a,b through 26a,b present the results. Those figures denominated with "a" pertain to differential pressure measurements on the blade, those with "b" compare sound power levels predicted from force measurements with directly measured sound power levels.

The remainder of this section discusses the results for the five experimental configurations.

1. B = 1; V = 0; U = 0 ft/sec

Figure 22a shows DPL spectra and Fig. 22b PWL spectra for 2000, 3000, and 4000 rpm. In this case, the single rotor blade was driven by the motor. The DPL spectra show the bending mode frequency at 400 Hz. The PWL spectra exhibit a haystack shape, with peaks in the 31.5 Hz, 50 Hz, and 63 Hz bands, corresponding to the fundamental rotational frequencies of 2000, 3000, and 4000 Hz. Radiation at these frequencies results from the steady force field (which, of course, cannot be measured with *fluctuating* pressure sensors); hence, no pronounced peaks at these frequencies appear in the DPL spectra. Figure 22b indicates that broadband levels were predicted corretly in the frequency range up to about 400 Hz. Above 400 Hz, sound power levels are substantially over-predicted, indicating that above this frequency the coherence of the force field is substantially reduced, so that force cancellation on the blade occurs, resulting in decreased sound radiation.

2. B = 1; V = 0; U = 70 ft/sec

Figures 23a and 23b show DPL and PWL spectra for the single rotor blade; the rotor was driven by the motor at 2000, 3000, and 4000 rpm; but, in addition, flow of 70 ft/sec was superimposed. This superposition of flow caused both the DPL and the PWL spectra at 2000 and 3000 rpm to shift to higher levels – as compared to the case without flow (see Figs. 22a and 22b). This shift indicates some flow phenomenon that causes larger (random) forces on the blade and that consequently increases sound radiation. Superposition of flow apparently increases the coherence of the force field beyond frequencies of 400 Hz, since levels are correctly predicted up to about 1600 Hz (Fig. 23b). Above 1600 Hz, force field coherence decreases. The deviation of predicted and measured levels below 400 Hz has the same reasons as before.

3. B = 10; V = 0; U = 0 ft/sec

Figures 24a and 24b show results for the 10-bladed rotor operating in a "propeller mode", (i.e., without superimposed flow) at 2000 and 3000 rpm. Presumably caused by insufficient balancing of the 10-bladed rotor, strong peaks appear at the shaft-rotational frequency and multiples of this frequency (33 Hz, 66 Hz, 133 Hz for 2000 rpm, and 50 Hz and 100 Hz for 3000 rpm) in the DPL data. For both speeds, the bending mode frequency of the blade at 400 Hz shows clearly. The PWL spectra (Fig. 24b) exhibit strong peaks at (a) the shaft rotational frequencies and their multiples, induced by the steady pressure field, and (b) at multiples of 10 (the number of blades) of the rotational frequency (333 Hz and 666 Hz for 2000 rpm, and 500 Hz and 1000 Hz for 3000 rpm).

On the basis of forces measured on one blade, sound power levels are predicted correctly over a large frequency range, from about 200 Hz to 4000 Hz (Fig. 24b); however, if each of the ten blades are considered to radiate independently of each other, sound power levels should be 10 dB higher than measured. Evidently, radiation from the ten-bladed rotor is reduced by 10 dB, possibly due to opposing forces induced on the neighboring blades.

4. B = 10; V = 0; U = 70 ft/sec

Superimposed flow on the 10-bladed rotor results in a "design rpm" of 2400 with very little variation in DP levels on the blade surface (see Fig. 21). Due to the fact that the rotor operated near or at a "design condition", peaks at shaft rotational frequencies are less pronounced (Fig. 25a) than in the previously discussed case, where the rotor was driven by the motor at some off-design condition (Fig. 24a). The PWL spectrum (Fig. 25b) shows a peak at 8000 Hz, corresponding to twice the rotational frequency times the number of blades. Furthermore, the high-frequency portion of both the DPL and the PWL spectrum exhibits increased levels for this condition as compared to the previous case without flow. Sound power levels were again predicted on the basis of the forces on *one* rotor blade, rather than on 10 blades, and the agreement extends to rather high frequencies.

5. B = 10; V = 9; U = 70 ft/sec

The presence of an upstream 9-bladed stator resulted in the DPL spectrum shown in Fig. 26a and the corresponding PWL spectra shown in Fig. 26b. Superimposed flow caused the rotor to spin at 2100 rpm. Peaks in the DPL spectrum at 320 and 640 Hz correspond to the loading harmonic frequencies of loading harmonic order λ equal to 9 and 18. Sound radiation due to these loadings appears at multiples of the blade passage frequency, 400 and 800 Hz. Other than that, both the DPL and PWL spectra are similar to the previous ones where stator blades were absent.

Similar considerations for sound power level prediction as outlined in (3) and (4) above hold for this case. A substantial deviation at higher frequencies of predicted and measured sound power levels indicates the occurrence of a drastic force field coherence breakdown for this particular configuration.

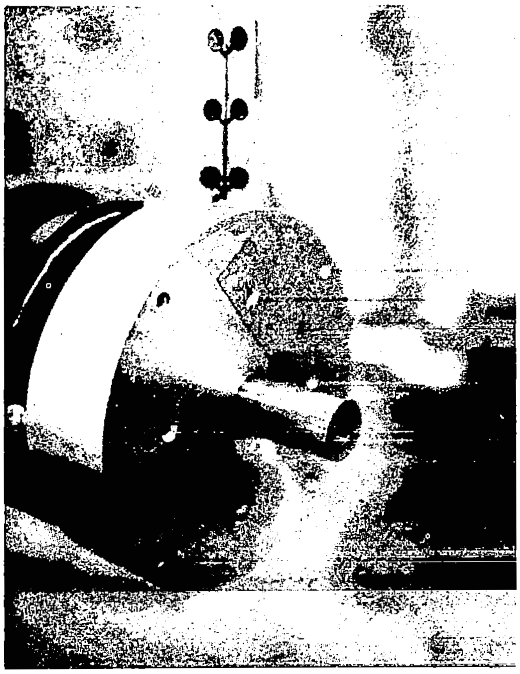

FIG. 11a. BASIC ROTOR CONFIGURATION

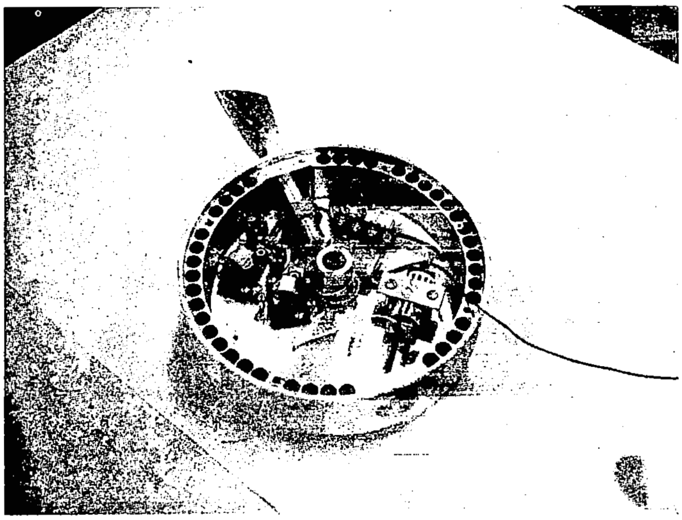

FIG. 11b. VIEW INTO ROTOR HUB WITH TRANSMITTER AND POWER SUPPLIES

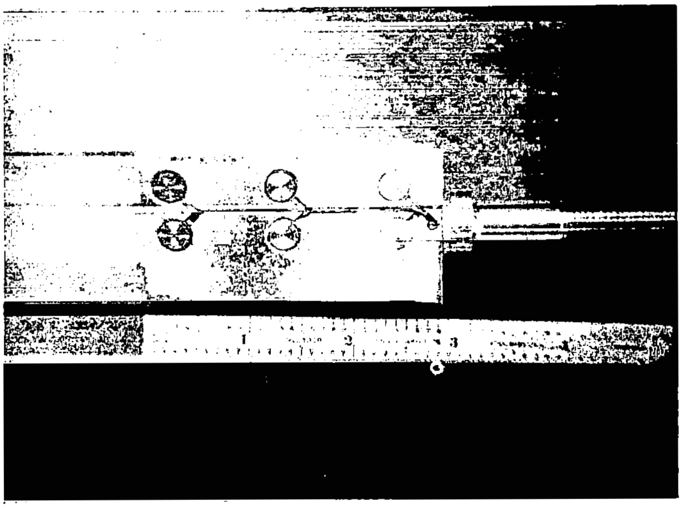

Pressure Side

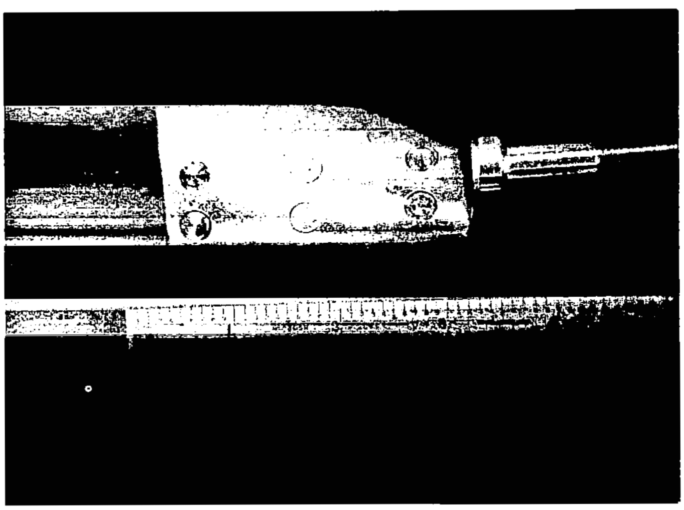

Suction Side

FIG. 12. INSTRUMENTED BLADE

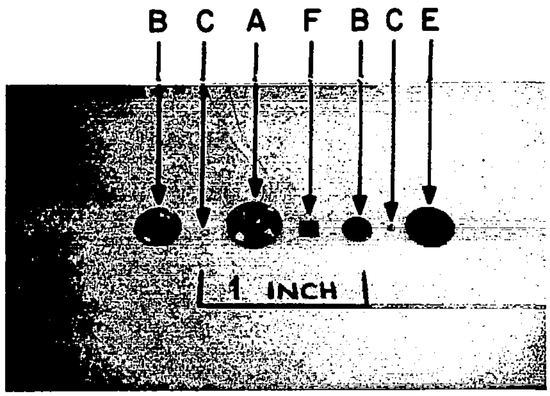

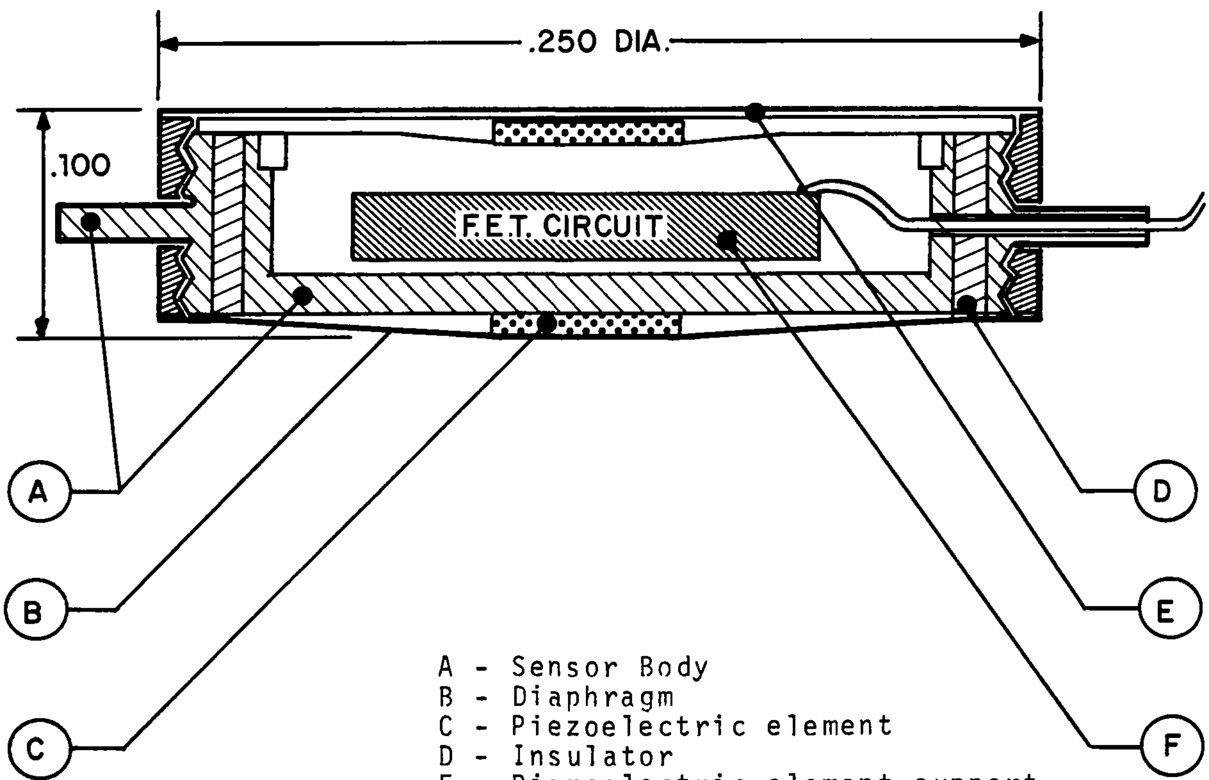

A - Sensor Body
B - Diaphragm
C - Piezoelectric element
D - Insulator
E - Piezoelectric element support
F - FET Circuitry with overvoltage protection

FIG. 13. DIFFERENTIAL PRESSURE SENSOR

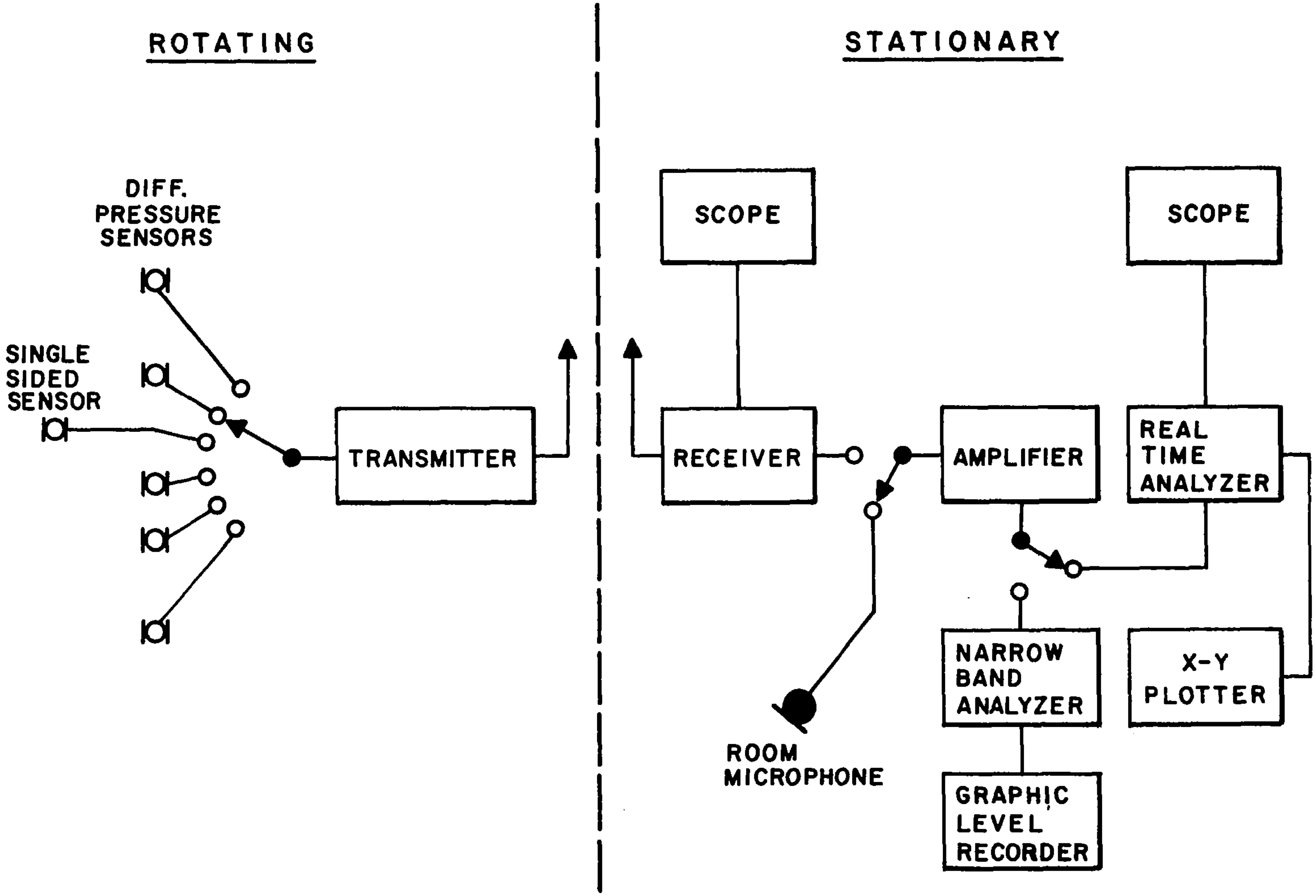

FIG.14 DATA ACQUISITION BLOCK DIAGRAM

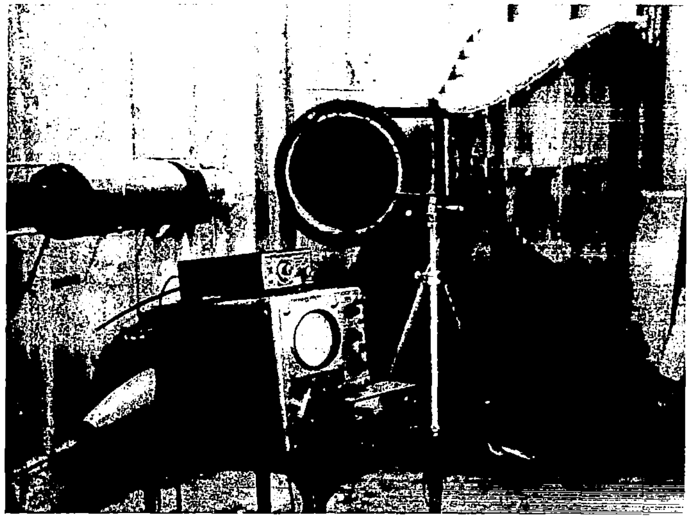

Fig. 15 Test Set-up: View toward open-jet wind tunnel

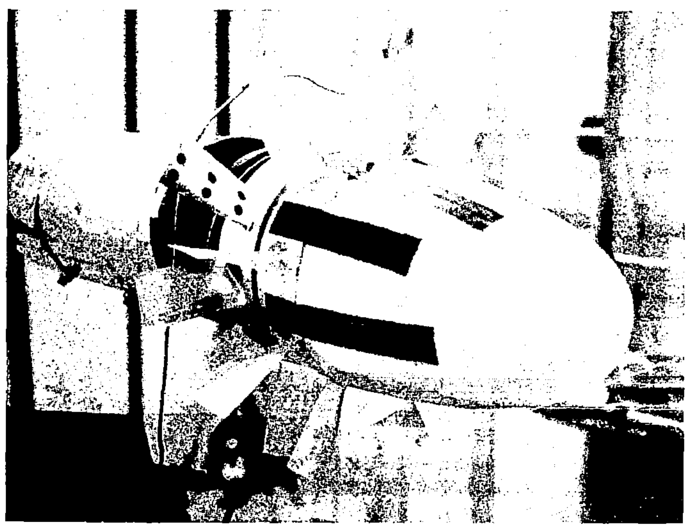

Fig. 16 Rotor Assembly: 9-bladed stator upstream of 10-bladed rotor

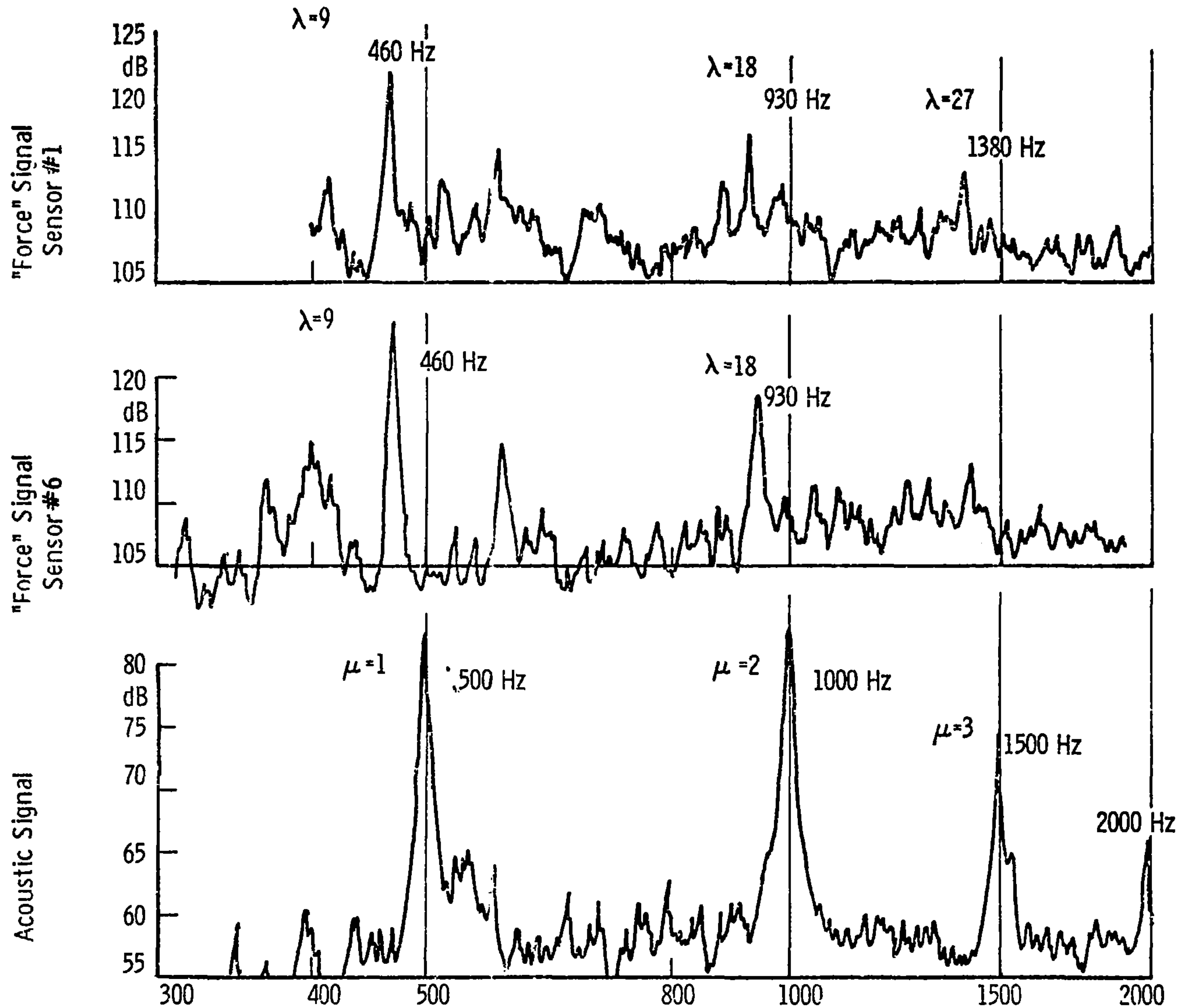

FIG. 17. DIFFERENTIAL-PRESSURE NARROWBAND ANALYSIS AND CORRESPONDING SOUND RADIATION

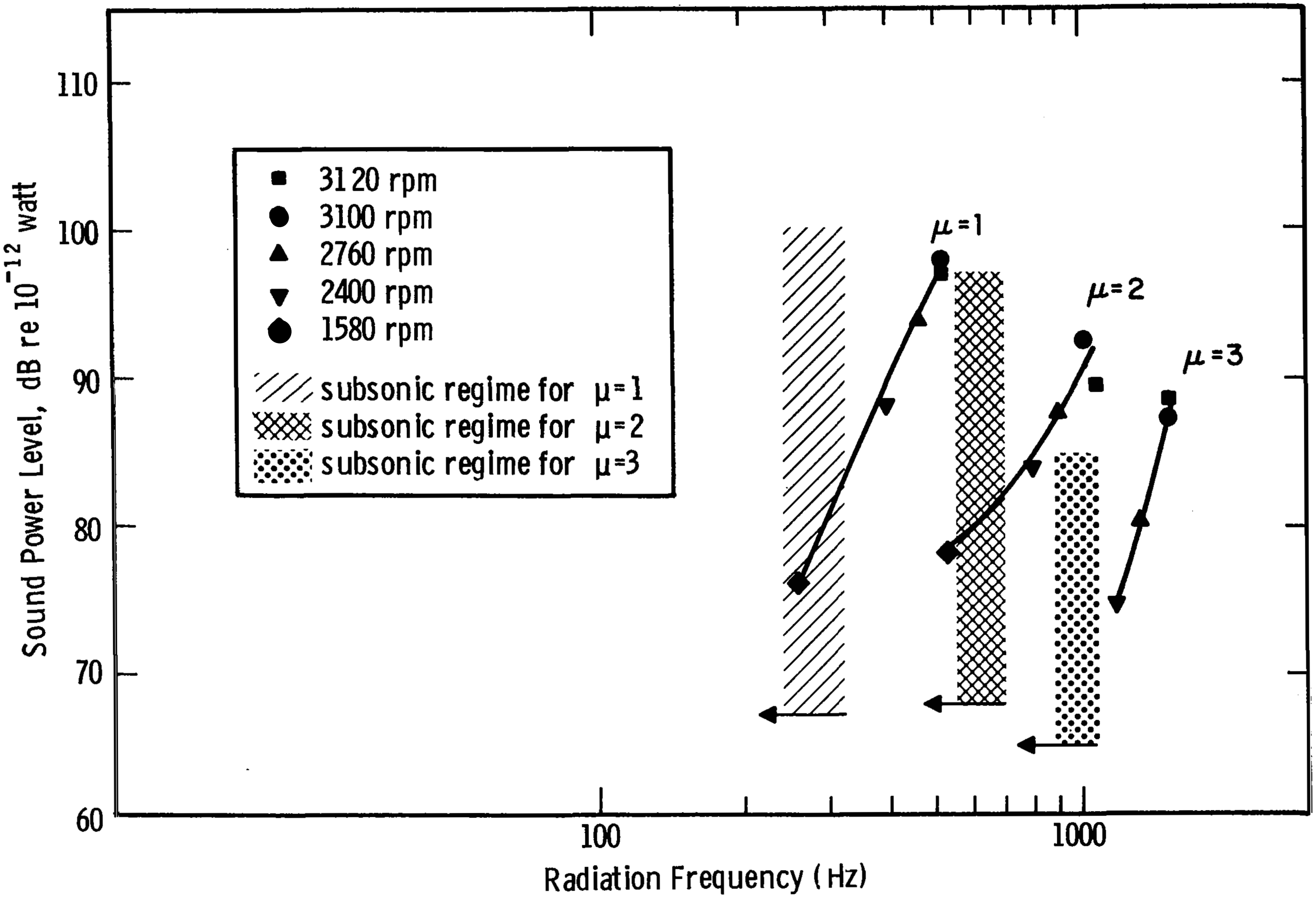

FIG.18 SOUND POWER LEVEL OF TONES OF MODAL ORDER μ

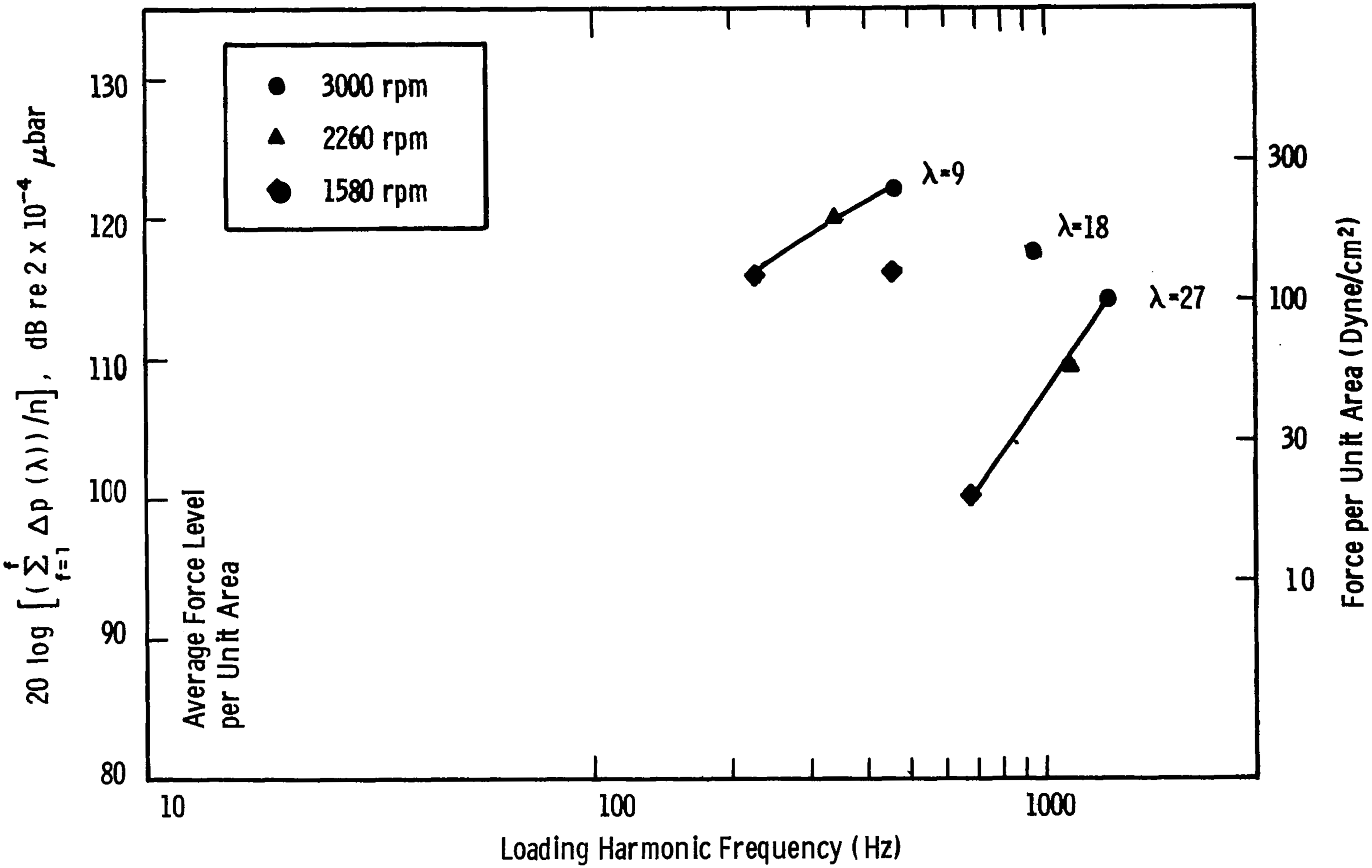

FIG.19 AVERAGE TOTAL FORCE DUE TO LOADING HARMONIC λ ON ROTOR BLADE

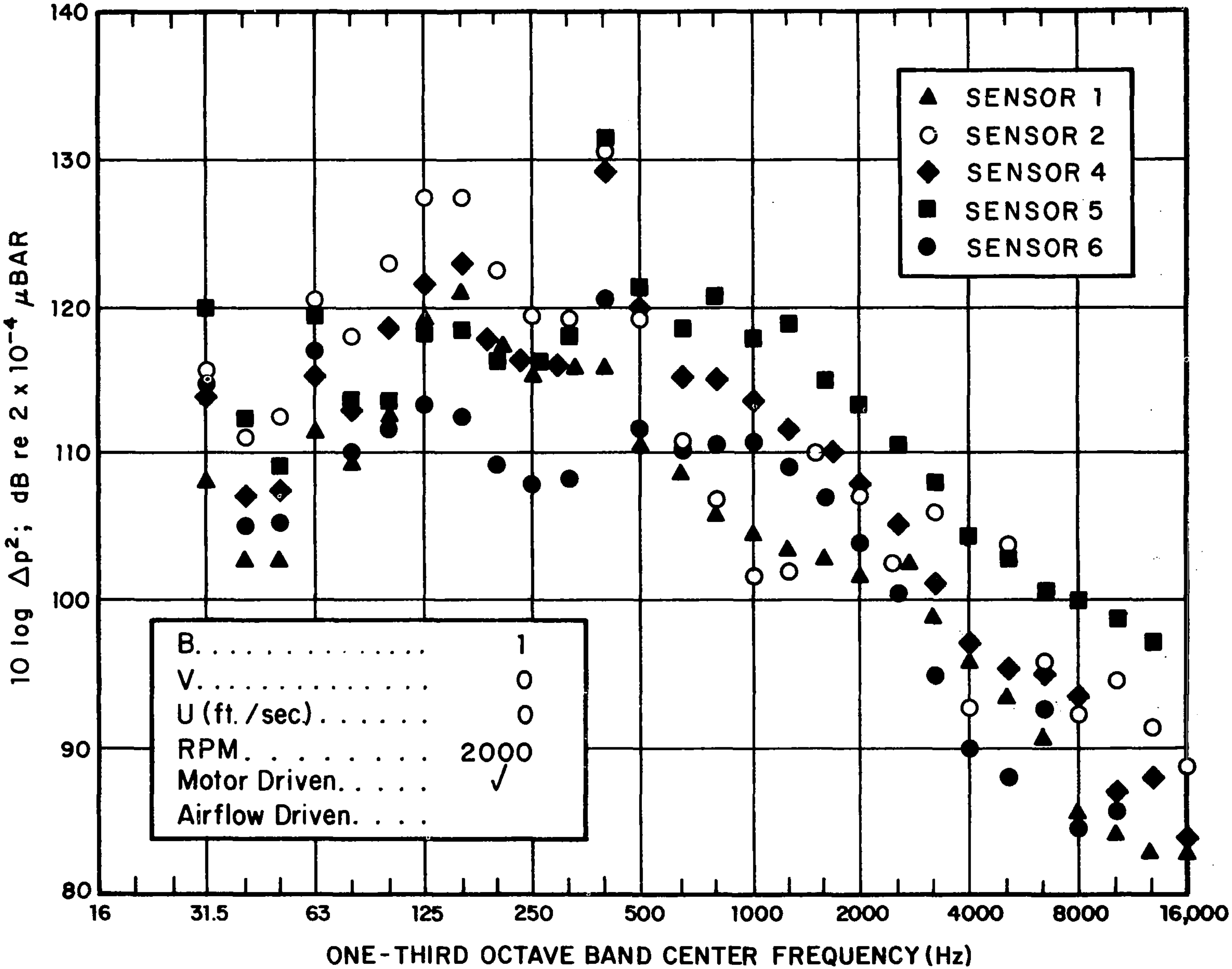

FIG.20 DIFFERENTIAL-PRESSURE LEVEL SPECTRA

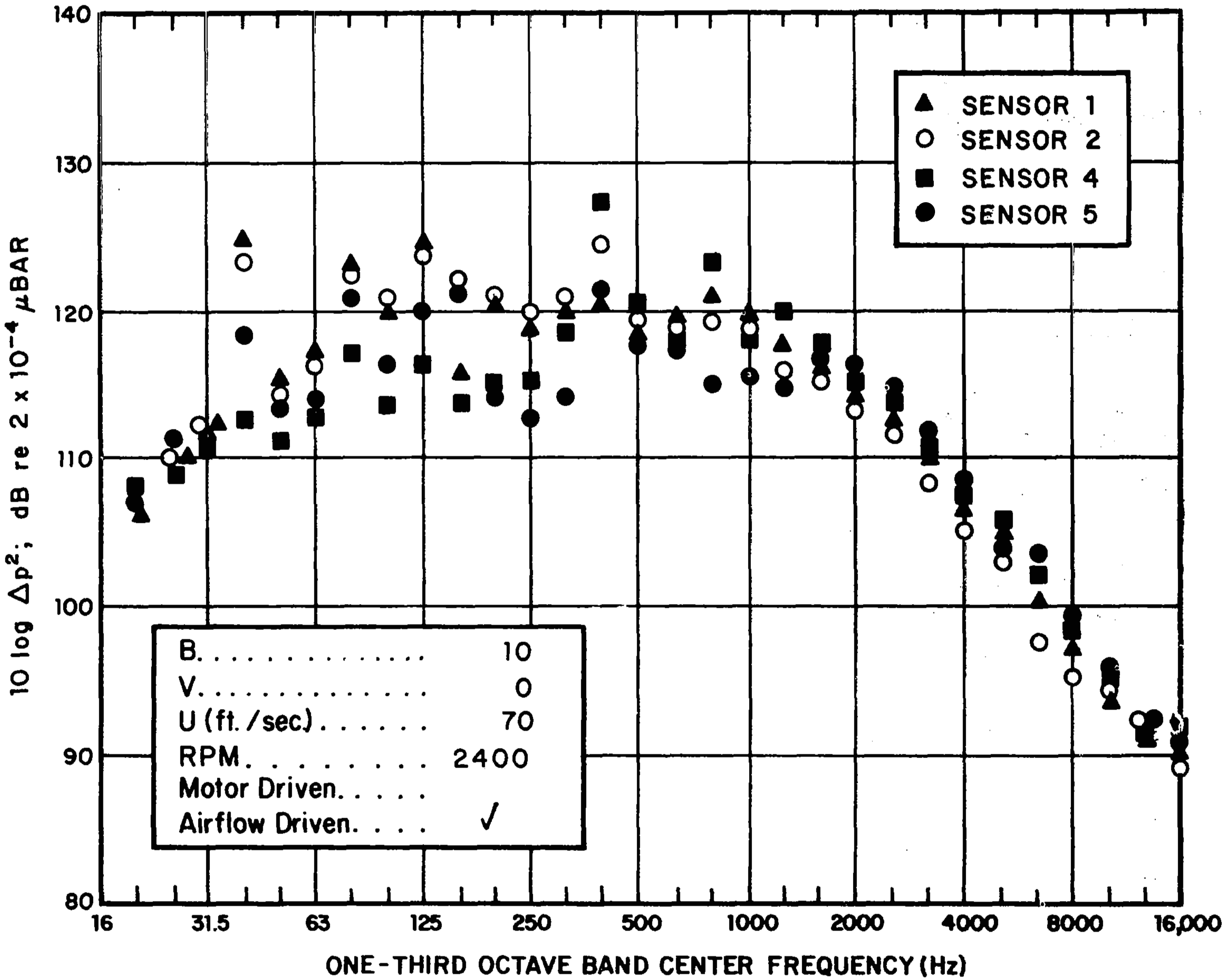

FIG. 21 DIFFERENTIAL-PRESSURE LEVEL SPECTRA

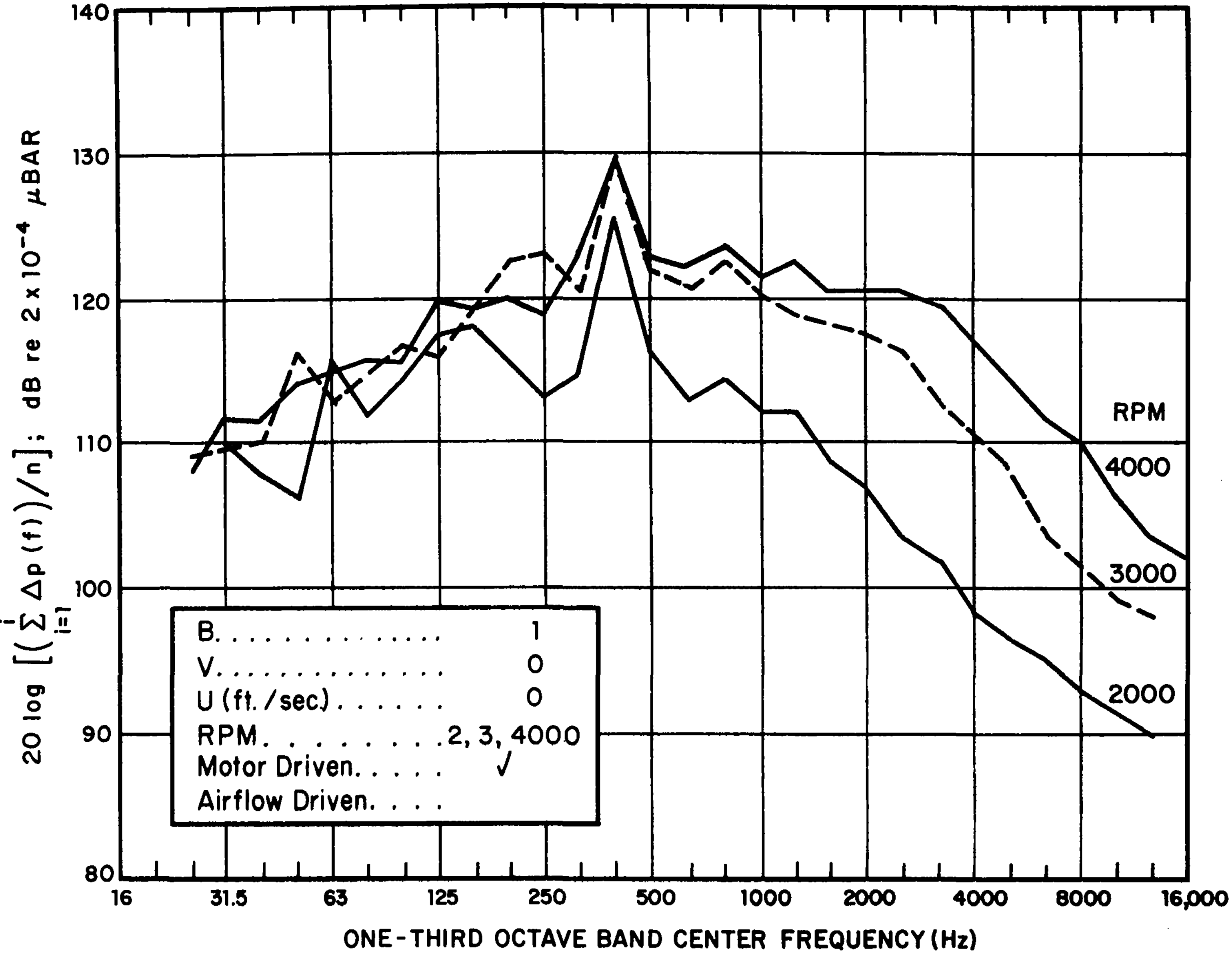

FIG.22a DIFFERENTIAL-PRESSURE LEVEL SPECTRA

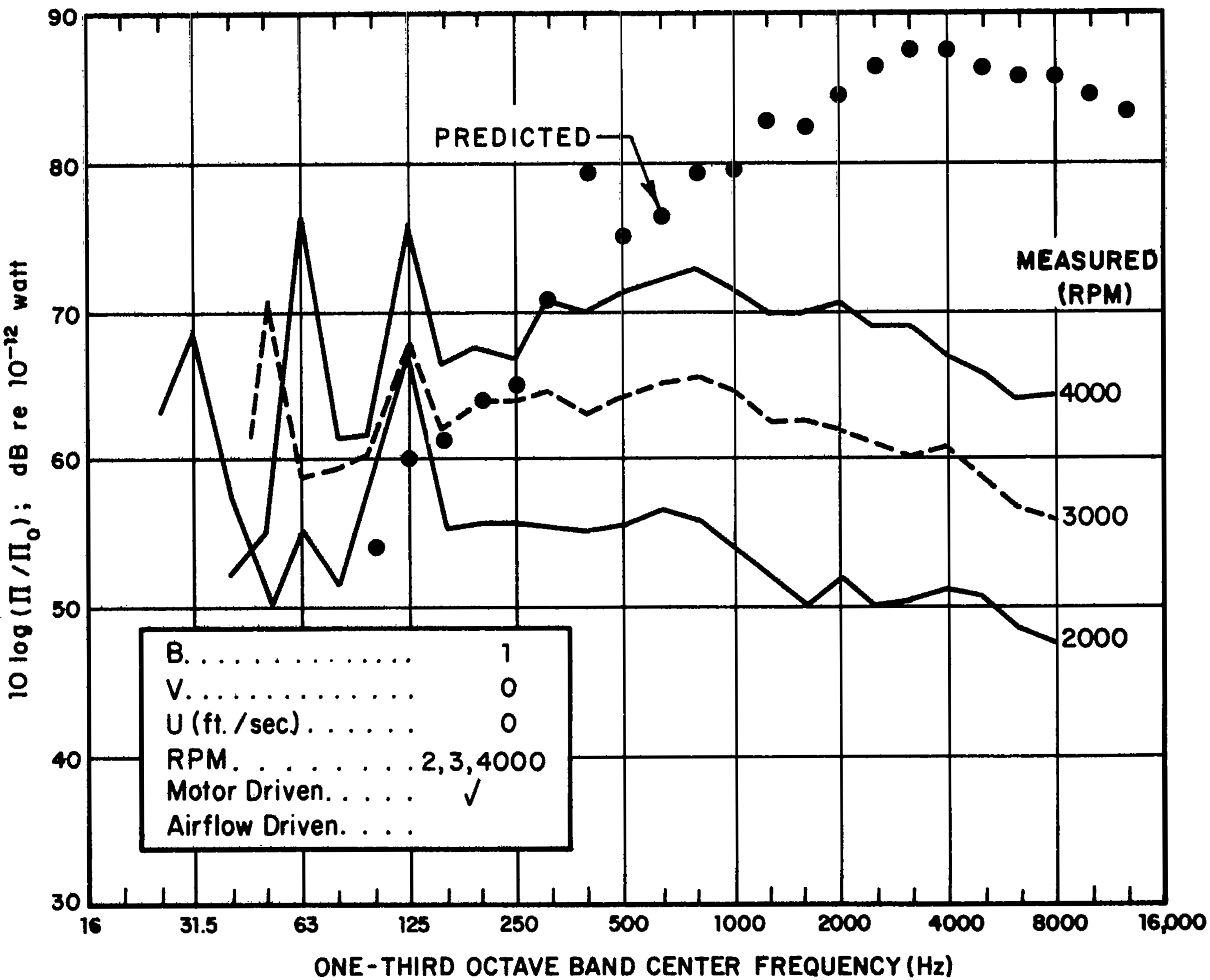

FIG.22b SOUND POWER LEVEL SPECTRA

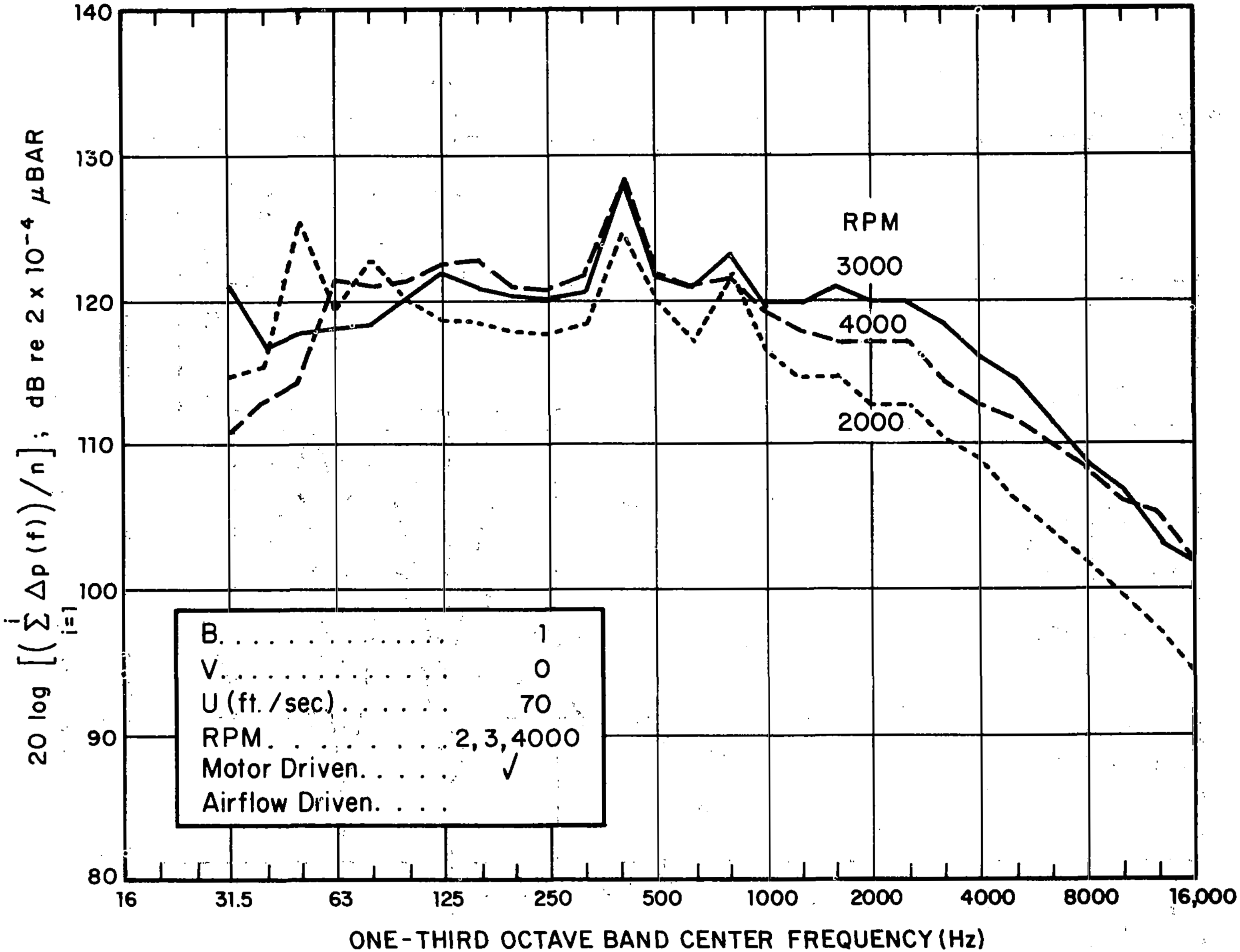

FIG.23a DIFFERENTIAL-PRESSURE LEVEL SPECTRA

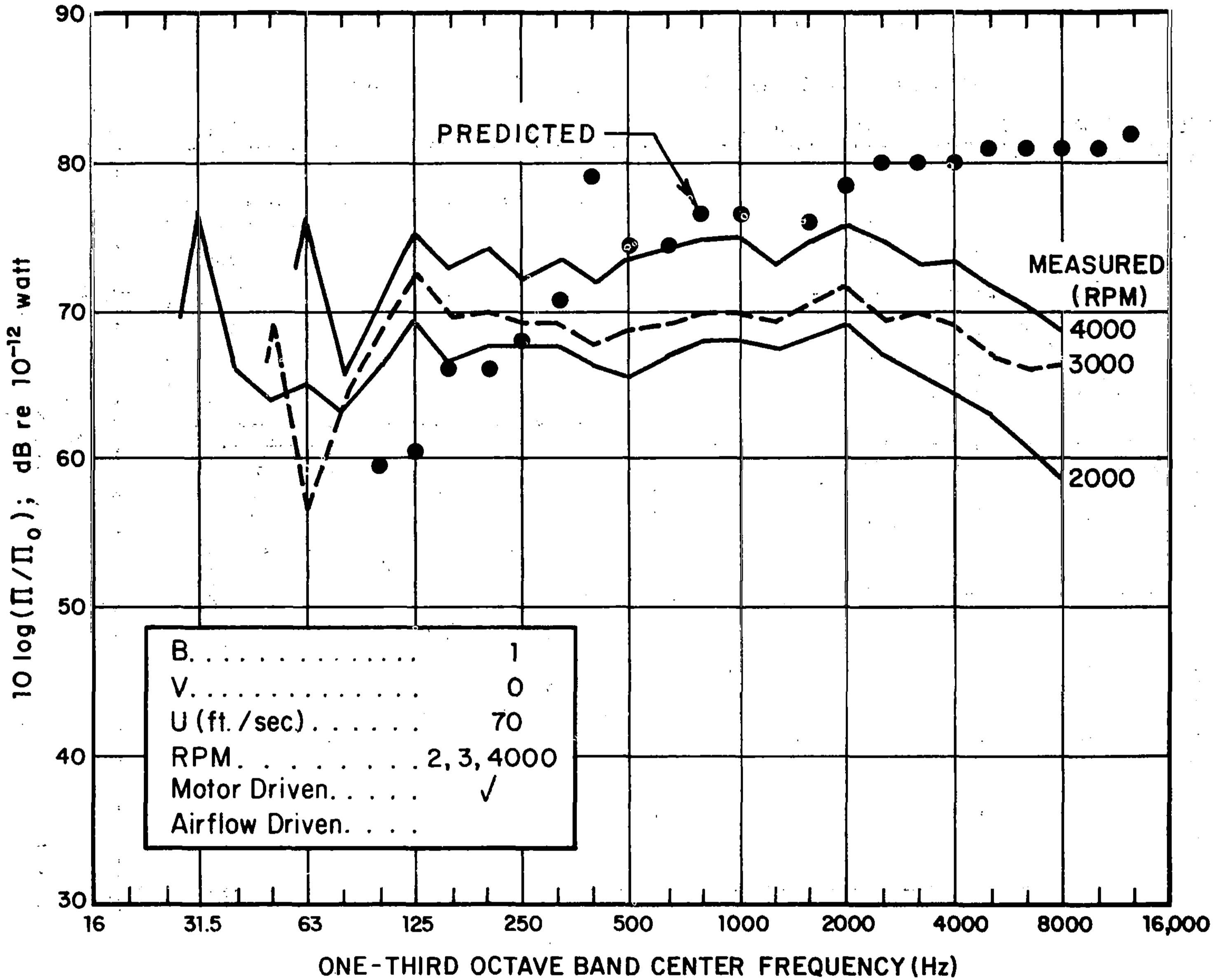

FIG.23b SOUND POWER LEVEL SPECTRA

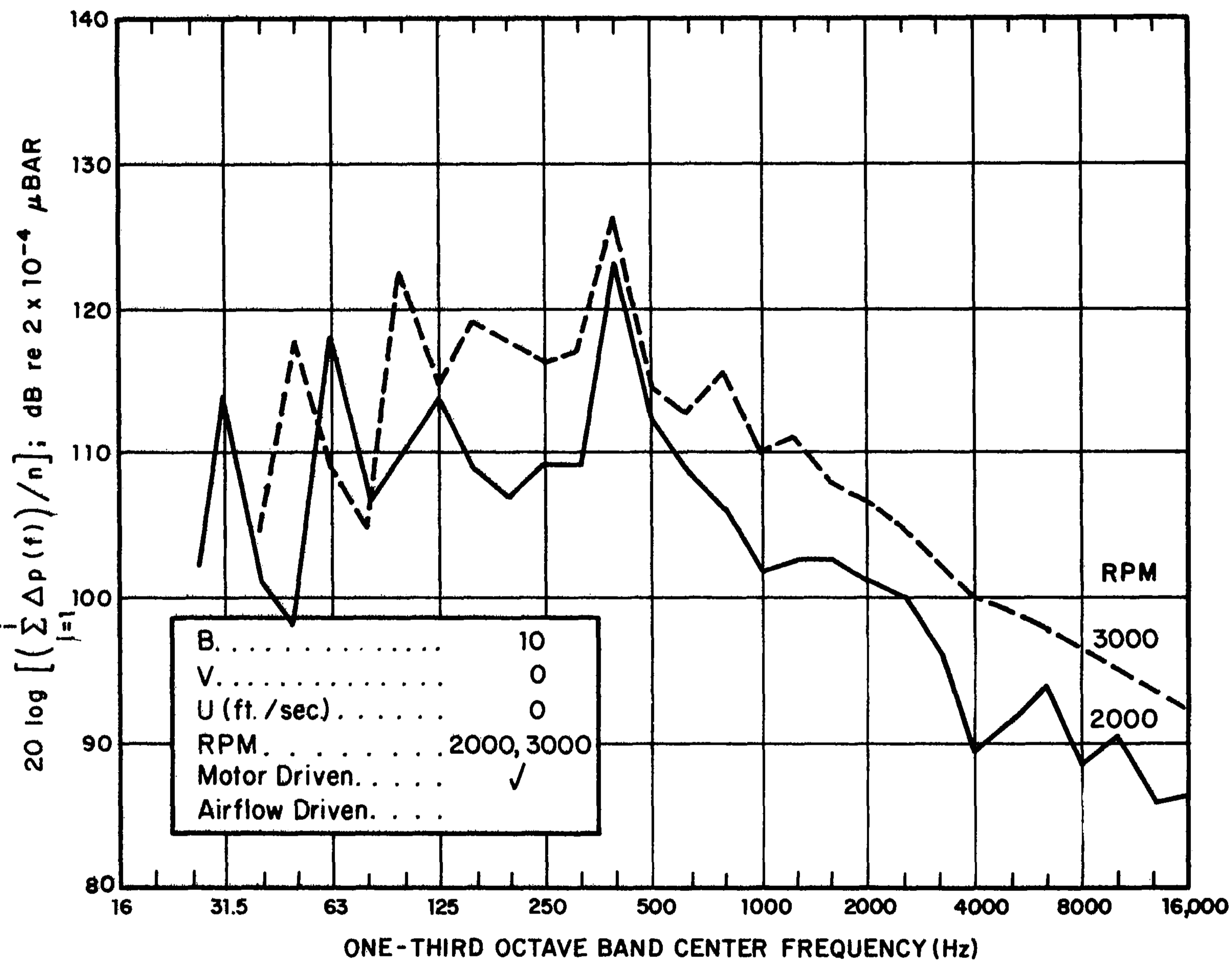

FIG.24a DIFFERENTIAL-PRESSURE LEVEL SPECTRA

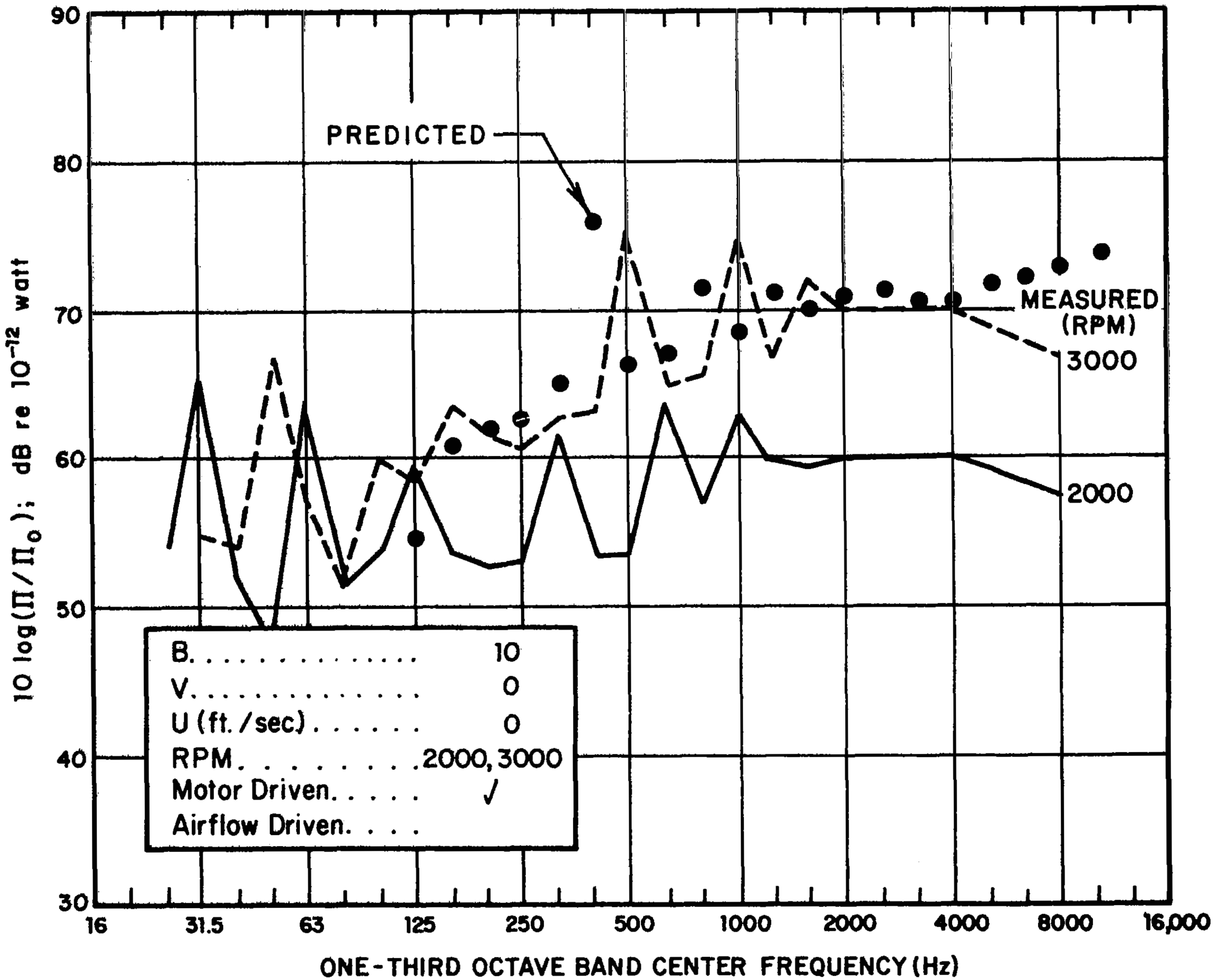

FIG.24b SOUND POWER LEVEL SPECTRA

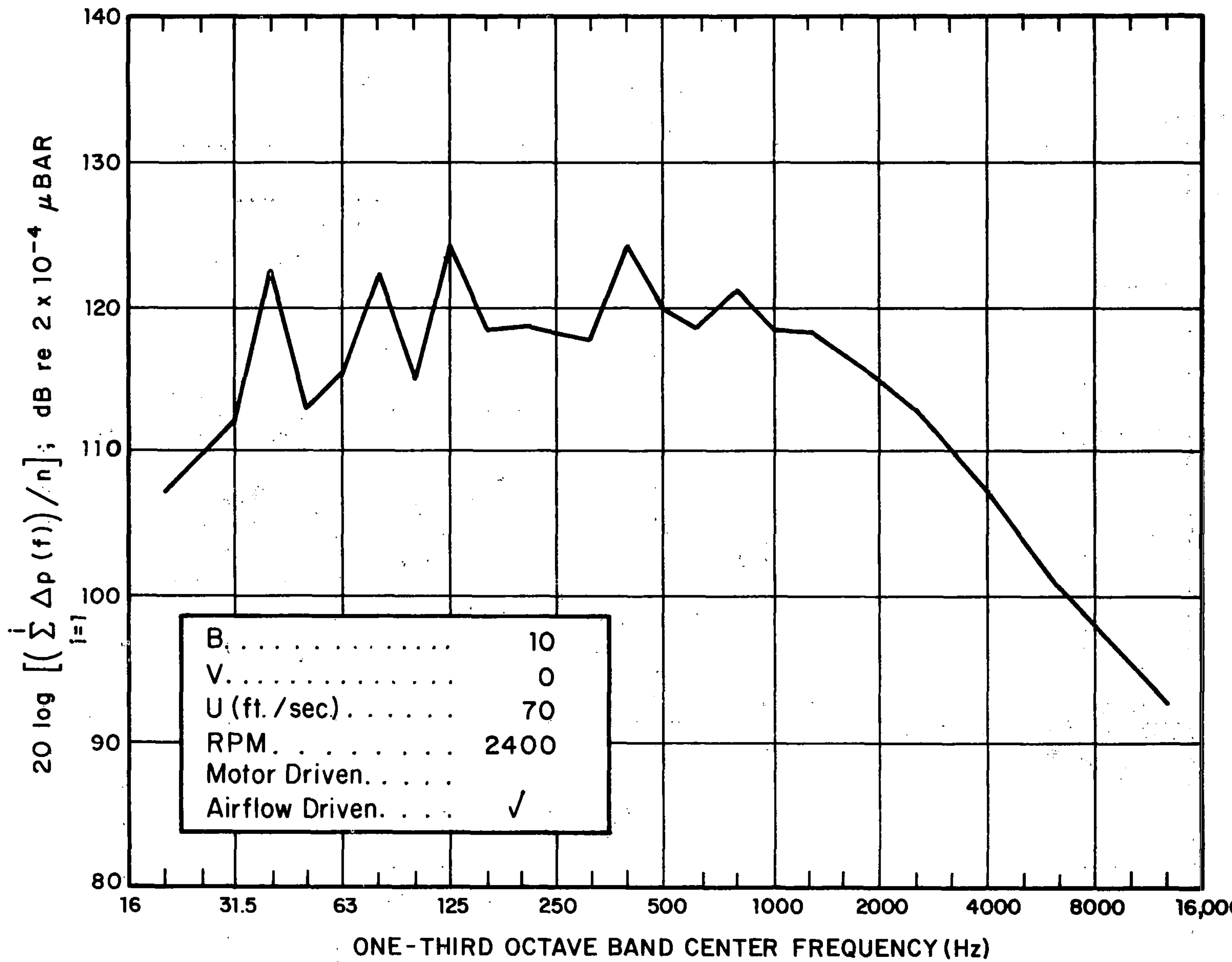

FIG.25a DIFFERENTIAL-PRESSURE LEVEL SPECTRUM

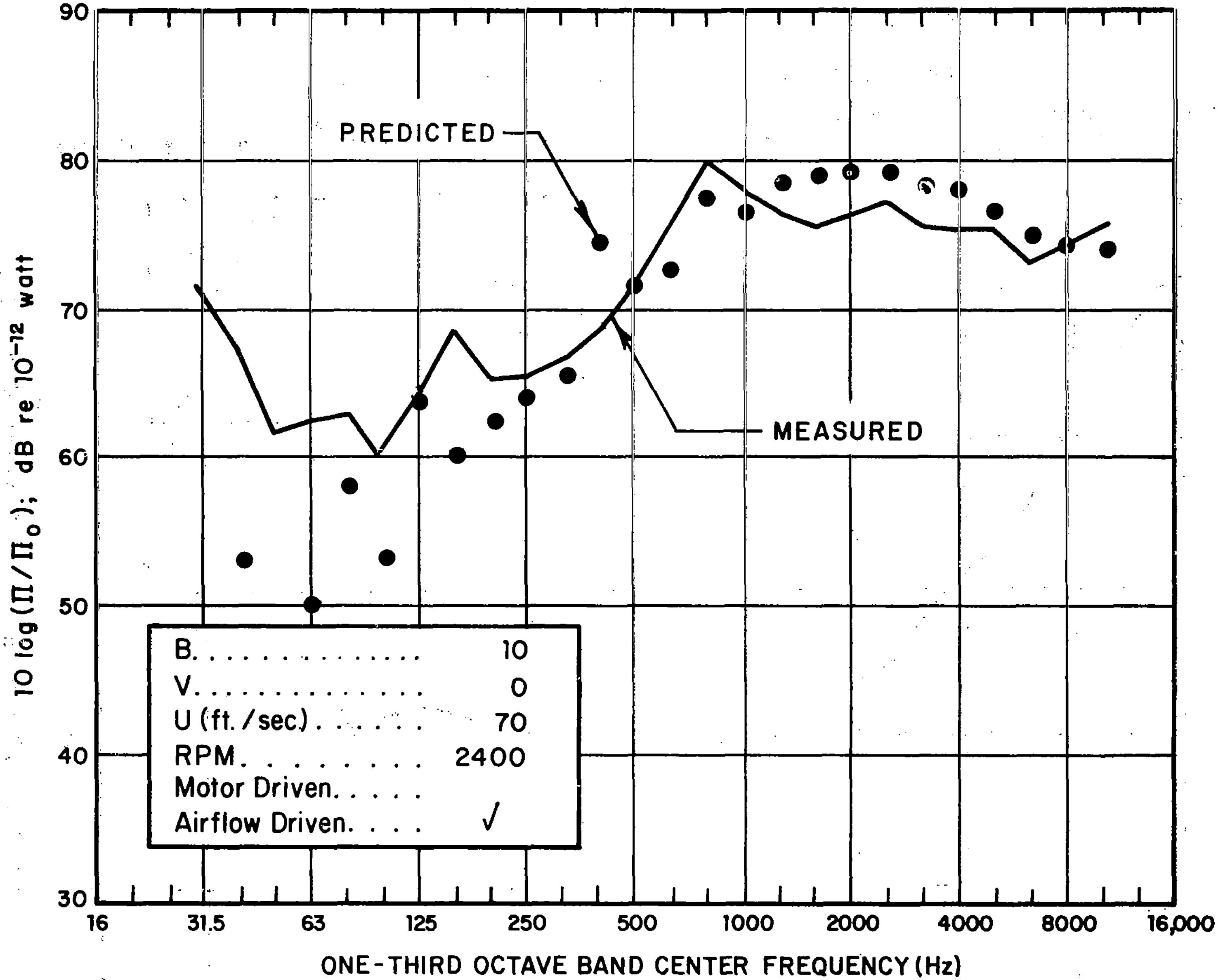

FIG.25b SOUND POWER LEVEL SPECTRUM

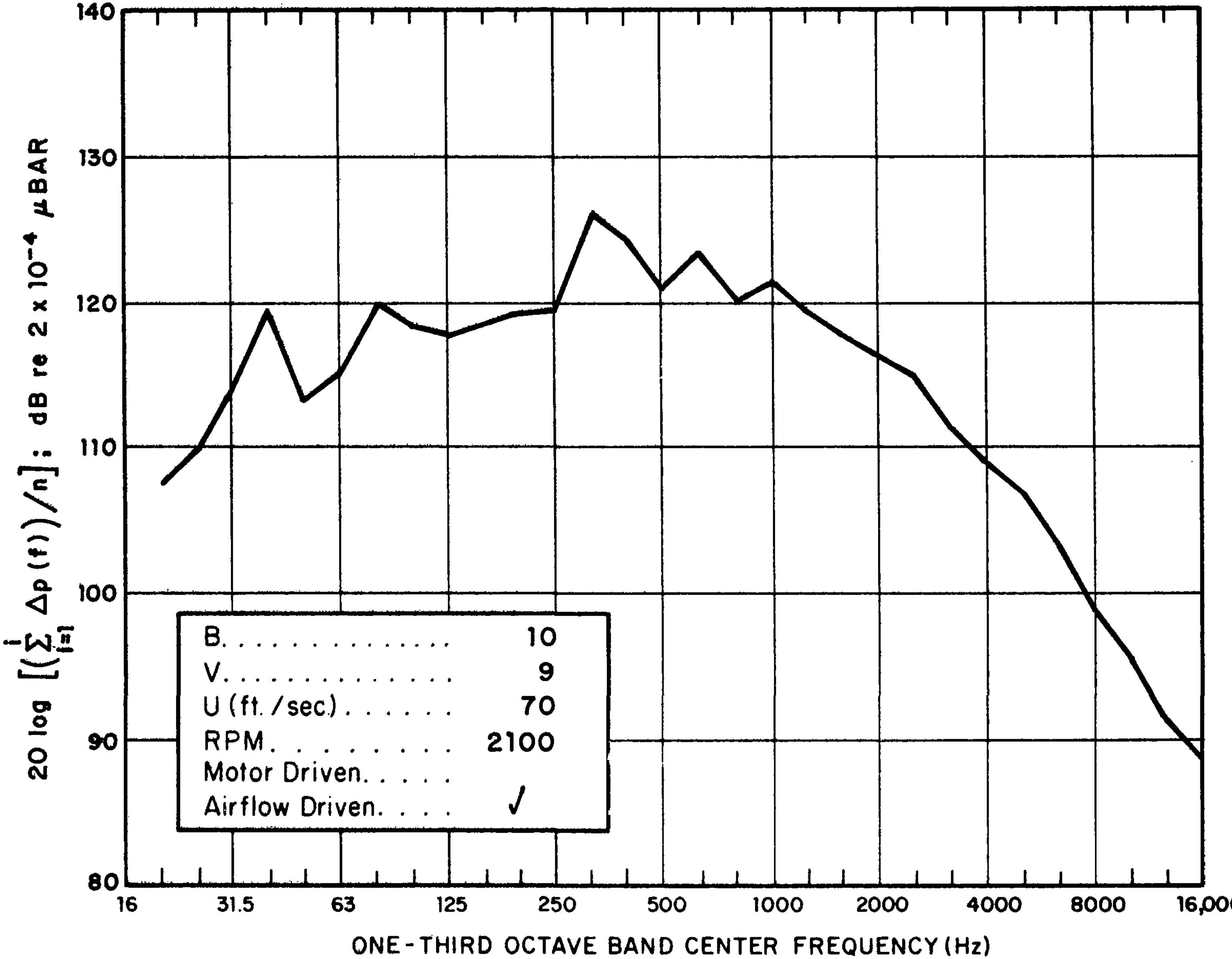

FIG.26a DIFFERENTIAL-PRESSURE LEVEL SPECTRUM

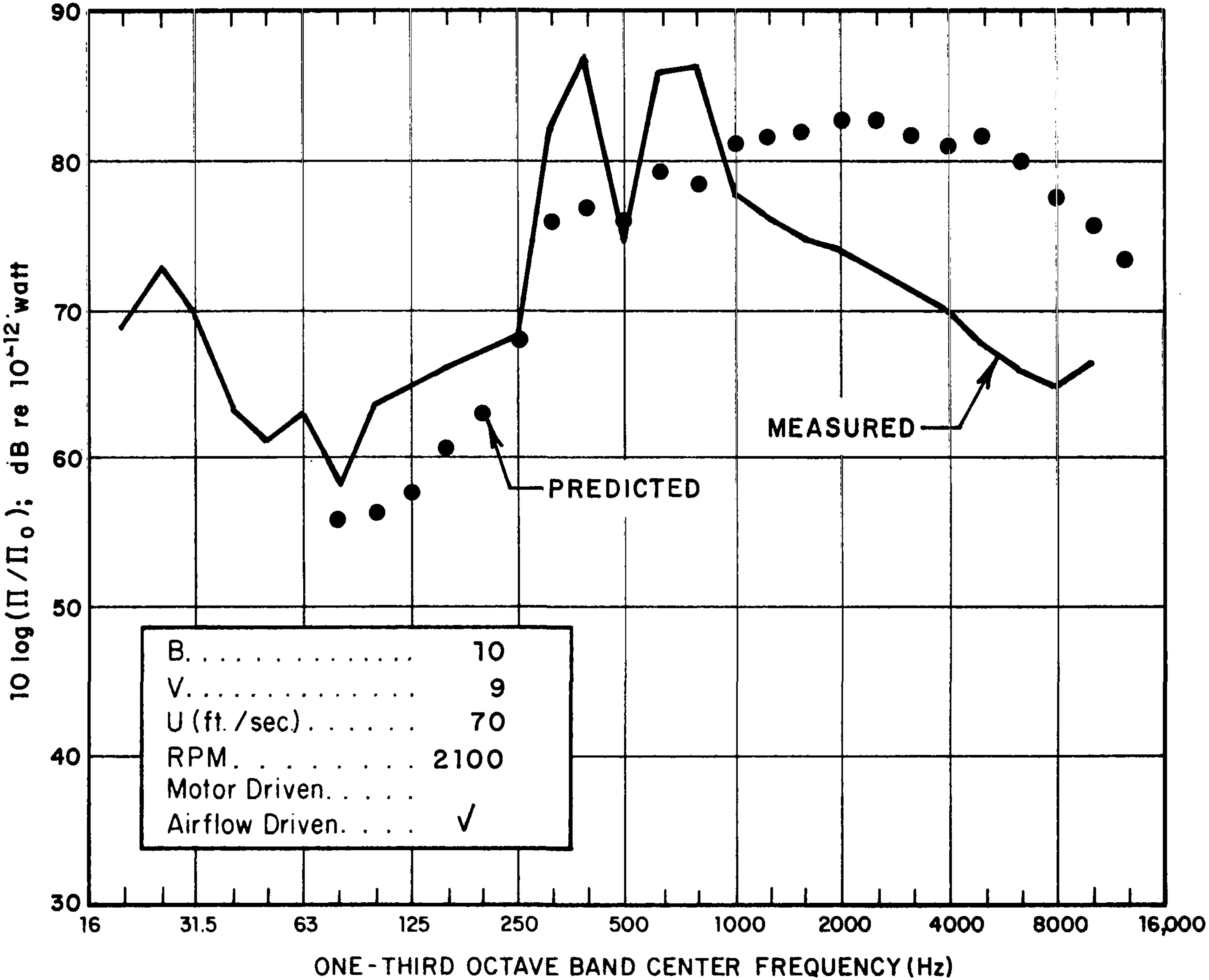

FIG.26b SOUND POWER LEVEL SPECTRUM

IV. SUMMARY AND CONCLUSIONS

Within the present study analytical models for the generation and radiation of discrete frequency sound by rotor/stator combinations in various environments were developed. On the basis of some rather simple and very familiar arguments about the size of ducts relative to acoustic wavelengths and some equally familiar ideas about subsonic versus supersonic phase velocities, it is possible to obtain a simple but accurate understanding of the important features of compressor noise theory. For example:

1. Using the idea of an infinite line of fluctuating lift and drag forces, one can develop very simple and accurate expressions for the total acoustic power radiated by a rotor in a free environment. The results agree with the more exact calculations of Lowson (reference 2).

2. The effect of a duct may be accounted for by considering a "very confined" annular environment, which is modeled as the region between two semi-infinite parallel plates, or by considering a rotor in a free environment where the sources are close to a single wall. The simple theory indicates under which conditions the duct becomes important and what models are appropriate for more detailed calculations.

3. The results of the simple theory agree with the more detailed calculations of Lansing (reference 3) when the same quantity, namely, "power radiated forward", is compared. An interesting question raised by this result is the effect of downstream conditions in a real compressor for which the semi-infinite circular duct is probably not a good model. It is also clear that the power radiated downstream must be included in some fashion.

To verify experimentally the analytical results, a system to measure fluctuating forces on rotating airfoils was developed, using special differential-pressure microphones and FM-telemetry. Relevant experiments covering both the discrete-frequency and the broadband aspects of stator/rotor sound generation were conducted and reasonable agreement of theory and experiment was achieved.

However, no experiments on the force field coherence characteristics on a single rotating blade or on a multibladed rotor disk were conducted. Thus, the frequency at which force field coherence breaks down and at which sound radiation decreases due to cancellation effects could not be determined directly. However, the experimental results clearly indicate the occurrence of such an effect, and it is suggested that detailed studies of the force field correlation characteristics be performed in a future study.

APPENDIX A

TRANSMISSION OF SOUND INTO A THREE-DIMENSIONAL ENVIRONMENT FROM A STATIONARY POINT SOURCE LOCATED IN A TWO-DIMENSIONAL ENVIRONMENT

1. Sound Generation in a Two-Dimensional Environment*

a. Plane wave expansions of the sources

To obtain the plane wave expansions of the monopole sources, we will solve the sound generation problem using Fourier transforms in y for a single source. We will then discuss the effect of the free-end boundary condition on the solution by means of images.

We introduce the Fourier transform pair in y, k_y.

$$\phi(x,y) = \frac{1}{2\pi} \int_{-\infty}^{\infty} \Phi(k_y,x) e^{ik_y y} \, dk_y$$

$$\Phi(k_y,x) = \int_{-\infty}^{\infty} \phi(x,y) e^{-ik_y y} \, dy \quad . \tag{A-1}$$

The equation governing sound generation in a two-dimensional environment is

$$\nabla^2\phi + k^2\phi = 0 \ , \tag{A-2}$$

where ϕ is the complex amplitude of the velocity potential

$$\tilde{\phi}(x,y,t) = \phi \cdot e^{-i\omega t} \quad .$$

---

* The source strength for the monopole $\tilde{S}_{2D}$ and for the dipole $\tilde{F}_{2D}$ used in this analysis are per unit length. 2D stands for two-dimensional.

The transformed equation is

$$\frac{d^2\Phi}{dx^2} + (k^2-k_y^2)\Phi = 0 \quad . \tag{A-3}$$

The solution to Eq. A-3 is

$$\Phi(x,k_y) = A(k)e^{-i\sqrt{k^2-k_y^2}} + B(k)e^{i\sqrt{k^2-k_y^2}} \quad . \tag{A-4}$$

The radiation condition on outgoing waves will be satisfied by letting $k = \omega/c + i\varepsilon$ so that $\phi\cdot e^{-i\omega t} = \phi\cdot e^{-i(\omega+i\varepsilon)t} \to 0$ at $t = -\infty$. This operation will place the branch points of $\sqrt{k^2-k_y^2}$ off the real axis in the Fourier inversion integral.

Consideration of outgoing waves gives

$$\Phi(k_y,x) = A(k)e^{i\sqrt{k^2-k_y^2}\,x} \quad ; \qquad \text{for } x > 0$$

and

$$\Phi(k_y,x) = B(k)e^{-\sqrt{k^2-k_y^2}\,x} \quad ; \qquad \text{for } x < 0 \quad . \tag{A-5}$$

The various fundamental sources are derived by applying different "jump" conditions at $x = 0$.

For a *monopole source*

$$\Delta\left(\frac{\partial\phi}{\partial x}\right) = \delta(y)\tilde{S}_{2D} \quad .$$

For a *vertical dipole source*

$$(\rho i\omega)\ \Delta\left(\frac{\partial\phi}{\partial x}\right) = \delta'(y)\tilde{F}_{2D} \quad . \tag{A-6}$$

For a *horizontal dipole source*

$$(\rho i\omega)\ \Delta(\phi) = \delta(y)\tilde{F}_{2D} \quad .$$

The other quantity [ϕ or $(\partial\phi/\partial x)$] is continuous across $x = 0$.

The Monopole Source

For the monopole source, Eq. A-6 becomes

$$\frac{d\Phi^{+}(k_y,x)}{dx} - \frac{d\Phi^{-}}{dx} = \tilde{S}_{2D} \quad ,$$

$$\Phi^{+} = \Phi^{-} \quad , \qquad A = B$$

$$i\sqrt{k^2-k_y^2}\ (2A) = 1 \quad , \qquad A = \frac{-i}{2}\,\frac{1}{\sqrt{k^2-k_y^2}} \quad . \tag{A-7}$$

The plane wave expansion of the monopole source is

$$\Phi^{\pm}(k_y,x) = \frac{-i}{2}\,\tilde{S}_{2D}\,\frac{e^{\pm i\sqrt{k^2-k_y^2}\ x}}{\sqrt{k^2-k_y^2}} \quad , \qquad \text{for } x \lessgtr 0 \quad . \tag{A-8}$$

Dipole Sources

The derivative of Eq. A-8 with respect to x should give a function proportional to the horizontal dipole; the multiplication of Eq. A-8 by ik_y (equivalent to a differentiation in y) gives a function proportional to the vertical dipole. This relation is an added check on the form and constants of proportionality in the jump condition for the various sources.

Solving Eq. A-6 for the horizontal dipole gives

$$(\rho i\omega)\ [A(k) + A(k)] = 1$$

$$A(k) = -B(k)$$

$$A(k) = \frac{-i}{2\rho\omega}$$

$$\Phi^{\pm}_{hD} = \frac{\pm 1 f_{2D}}{2(\rho\omega i)} \cdot e^{\pm i\sqrt{k^2-k_y^2}\ x} \quad . \qquad \text{(A-9)}$$

For the vertical dipole

$$(\rho i\omega)\sqrt{k^2-k_y^2}\ (2A) = k_y\tilde{F}_{2D}$$

$$\Phi[\delta'(y)] = ik_y$$

$$A = \frac{k_y\tilde{F}_{2D}}{2\sqrt{k^2-k_y^2}\ (\rho i\omega)}$$

$$A = B$$

$$\Phi^{\pm}_{vD} = \frac{\tilde{F}_{2D}}{(2\rho\omega i)} \cdot e^{\pm i\sqrt{k^2-k_y^2}\ x} \cdot \frac{k_y}{\sqrt{k^2-k_y^2}} \quad . \qquad \text{(A-10)}$$

b. Summary of results

Monopole

$$\Phi^{\pm}_{M}(x,k_y) = -\frac{i}{2}\ \frac{\tilde{S}_{2D} \cdot e^{\pm i\sqrt{k^2-k_y^2}\ x}}{\sqrt{k^2-k_y^2}} \quad , \quad x \gtrless 0 \quad . \qquad \text{(A-11)}$$

Vertical Dipole

$$\Phi^{\pm}_{vD}(x,k_y) = \frac{\tilde{F}_{2D}}{(2\rho\omega i)} \cdot \frac{k_y}{\sqrt{k^2-k_y^2}} \cdot e^{\pm i\sqrt{k^2-k_y^2}\, x} \quad , \quad x \gtrless 0 \ . \tag{A-12}$$

Horizontal Dipole

$$\Phi^{\pm}_{hD}(x,k_y) = \pm \frac{\tilde{F}_{2D}}{(2\rho\omega i)} e^{\pm i\sqrt{k^2-k_y^2}\, x} \quad , \quad x \gtrless 0 \ . \tag{A-13}$$

It can be seen that

$$\Phi_{vD} \sim k_y \Phi_M$$

and that

$$\Phi_{nD} \sim \frac{d(\Phi_M)}{dx} \ . \tag{A-14}$$

c. **Solution for the two-dimensional environment with images**

We now consider the above sources located at $x = 0$ in the semi-infinite two-dimensional environment. The appropriate boundary condition is then $\Phi = 0$ along the y-axis. This condition is assured by choosing image singularities, located at $x = -\ell$, which are of the same strength and proper sign.

Imaging the sources of Eqs. A-11, A-12, and A-13, we have for the region $-\ell < x < +\ell$, the following expressions for Φ, which satisfy Φ so that at $x = 0$:

For the *monopole source*

$$\Phi_M = \frac{i}{2}\,\frac{\tilde{S}_{2D}\, e^{-i\sqrt{k^2-k_y^2}\,(x-\ell)}}{\sqrt{k^2-k_y^2}} + \frac{i}{2}\,\frac{\tilde{S}_{2D}\, e^{i\sqrt{k^2-k_y^2}\,(x+\ell)}}{\sqrt{k^2-k_y^2}} \quad . \qquad \text{(A-15)}$$

For the *vertical dipole*

$$\Phi_{vD} = \frac{\tilde{F}_{2D}}{(2\rho\omega i)}\,\frac{k_y}{\sqrt{k^2-k_y^2}}\left[e^{-i\sqrt{k^2-k_y^2}\,(x-\ell)} - e^{i\sqrt{k^2-k_y^2}\,(x+\ell)}\right] \quad . \qquad \text{(A-16)}$$

For the *horizontal dipole*

$$\Phi_{hD} = \frac{\tilde{F}_{2D}}{(2\rho\omega i)}\, e^{-i\sqrt{k^2-k_y^2}\,(x-\ell)} + \frac{1}{(2\rho\omega i)}\, e^{i\sqrt{k^2-k_y^2}\,(x+\ell)} \quad . \qquad \text{(A-17)}$$

Of particular interest is the plane wave expansion of $\partial\Phi/\partial x$ – the horizontal particle velocity along the y-axis – since this is the mechanism responsible for sound transmission into the free environment.

The *monopole source*

$$\left.\frac{\partial\Phi}{\partial x}\right|_{x=0} = \tilde{S}_{2D} \cdot e^{+i\sqrt{k^2-k_y^2}\,\ell} \quad . \qquad \text{(A-18)}$$

The *vertical dipole*

$$\left.\frac{\partial\Phi}{\partial x}\right|_{x=0} = \frac{\tilde{F}_{2D}}{\rho\omega} \cdot k_y \cdot e^{+i\sqrt{k^2-k_y^2}\,\ell} \quad . \qquad \text{(A-19)}$$

The *horizontal dipole*

$$\left.\frac{\partial \Phi}{\partial x}\right|_{x=0} = \frac{\tilde{F}_{2D}}{\rho\omega} \sqrt{k^2-k_y^2}\; e^{i\sqrt{k^2-k_y^2}\,\ell} \quad . \tag{A-20}$$

2. Transmission of a Plane Wave in a Two-Dimensional Environment into a Three-Dimensional Environment

We now consider the power radiated into the three-dimensional space at the slit by the particle velocities produced by the incidence and reflection of the waves in the confined environment. In the previous analyses, we obtained the velocity normal to the slit in the form of a Fourier transform in y. This method is very convenient for the calculation of the sound radiated into the free environment. Each wave component is considered separately.

The governing equation in this space is the three-dimensional wave equation

$$\nabla^2\phi + c^2\phi = 0 \quad . \tag{A-21}$$

Again, using Fourier transforms in y, we obtain

$$\nabla^2_{2D}\Phi(k_y,x,z) + (k^2-k_y^2)\Phi(k_y,x,z) = 0 \quad . \tag{A-22}$$

The dominant radiation from the slit is due to the "source effect" of the normal velocity at the slit. Thus, the waves in the free space are cylindrical and are functions of r and k_y only. Equation A-22 becomes

$$\frac{1}{\gamma}\frac{\partial}{\partial r}\left[r\,\frac{\partial\Phi}{\partial r}(r,k_y)\right] + (k^2-k_y^2)\Phi(k_y,r) = 0 \quad , \tag{A-23}$$

where $r = \sqrt{x^2+z^2}$.

The outgoing-wave solution to Eq. A-22 is

$$\Phi(k_y,r) = A(k_y)H_0^{(1)}\left(\sqrt{k^2-k_y^2}\,r\right) \quad . \tag{A-24}$$

To determine $A(k_y)$, we examine the behavior of $\Phi(k_y,r)$ for small r, equating its source-like behavior to the effective source at the slit from the normal velocity.

For small r,

$$\Phi(k_y,r) \approx A(k)\left(1 + i\,\frac{2}{\pi}\log r + iC\right) . \qquad \text{(A-25)}$$

The source-like behavior is given by

$$\Phi(k_y,r) \approx A(k)\, i\, \frac{2}{\pi} \log r$$

$$\approx \frac{S(k)}{2\pi} \log r \quad , \qquad \text{(A-26)}$$

where

$$\frac{S(k)}{2\pi} = \frac{A(k)i^2}{\pi} \quad ; \qquad A(k) = -i\; S(k)/4 \quad .$$

The source strength due to the reflected and incident waves is

$$S(k_y) = -u(k_y)h \qquad \text{(A-27)}$$

for each wave component. The $u(k_y)$ for the various sources are given in Eqs. A-18, A-19, and A-20,

$$\Phi(k_y,r) = +\,\frac{i}{4}\,u(k_y)h \cdot H_0^{(1)}\left(\sqrt{k^2+k_y^2}\; r\right) \quad . \qquad \text{(A-28)}$$

For the various sources, combining Eq. A-26 with Eqs. A-18 through A-20 gives the following forms for $\Phi(k_y;r)$ in free space:

Monopole

$$\Phi_M(r,k_y) = i\,\frac{1}{4}\left[-e^{i\sqrt{k^2-k_y^2}\;\ell}\right] h\; \tilde{S}_{2D} H_0^{(1)}\left(\sqrt{k^2-k_y^2} \cdot r\right) \quad . \qquad \text{(A-29)}$$

Vertical Dipole

$$\Phi_{vD}(r,k_y) = i\,\frac{1}{4}\left[-\frac{k_y}{\rho\omega}\,e^{i\sqrt{k^2-k_y^2}}\right]h\;\tilde{F}_{2D}H_0^{(1)}\left(\sqrt{k^2-k_y^2}\;r\right) \quad . \tag{A-30}$$

Horizontal Dipole

$$\Phi_{hD}(r,k_y) = i\,\frac{1}{4}\left[\frac{\sqrt{k^2-k_y^2}}{\rho\omega}\cdot e^{i\sqrt{k^2-k_y^2}\,\ell}\right]h\;\tilde{F}_{2D}H_0^{(1)}\left(\sqrt{k^2-k_y^2}\;r\right) \quad . \tag{A-31}$$

Now that we have the Fourier transforms of u and p along the slit, we can calculate the power radiated into free space.

$$p(y,t) = \mathrm{Re}\left\{\frac{i\rho\omega}{2\pi}\int_{-\infty}^{\infty}\Phi e^{ik_y\cdot y}\,dk_y\cdot e^{-i\omega t}\right\}$$

$$u(y,t) = \mathrm{Re}\left\{\frac{1}{2\pi}\int_{-\infty}^{\infty}Ue^{ik'y}\,dk'\;e^{-i\omega t}\right\}$$

$$\Pi(t) = h\sin\omega t\int_{-\infty}^{\infty}\mathrm{Im}\left\{\frac{i\rho\omega}{2\pi}\int_{-\infty}^{\infty}\Phi e^{ik_y y}\,dk\right\}$$

$$\cdot\;\mathrm{Im}\left\{\frac{1}{2\pi}\int_{-\infty}^{\infty}-Ue^{ik'y}\,dk'\right\}dy$$

$$+\;h\cos\omega t\int_{-\infty}^{\infty}\mathrm{Re}\left\{\frac{i\rho\omega}{2\pi}\int_{-\infty}^{\infty}\Phi e^{iky}\,dk\right\}$$

$$\cdot\;\mathrm{Re}\left\{\frac{1}{2\pi}\int_{-\infty}^{\infty}-Ue^{ik'y}\,dk'\right\}dy \quad . \tag{A-32}$$

In this problem, Φ and U are both even or both odd for the various simple sources.

For Φ and U_∞ even in k_y (but complex),

$$\Pi(t) = h \sin\omega t \int_{-\infty}^{\infty} \mathrm{Im}\left\{\frac{i\rho\omega}{(2\pi)^2} \int_{-\infty}^{\infty} \phi \cos k_y y \, dk_y\right\}$$

$$\cdot \mathrm{Im}\left\{\int_{-\infty}^{\infty} u \cos k_y' y \, dk_y\right\} k_y$$

$$+ h \cos\omega t \int_{-\infty}^{\infty} \mathrm{Re}\left\{\frac{i\rho\omega}{(2\pi)^2} \int_{-\infty}^{\infty} \phi \cos k_y y \, dk_y\right\}$$

$$\cdot \mathrm{Re}\left\{\int_{-\infty}^{\infty} u \cos k_y' \, dk_y'\right\} k_y \quad . \tag{A-33}$$

Integrating with respect to y, we find

$$\frac{1}{2\pi} \int_{-\infty}^{\infty} \cos k_y' y \cos k_y y d_y = \frac{\delta}{2} (k_y + k_y') + \frac{\delta}{2} (k_y - k_y')$$

$$\Pi(t) = h \sin\omega t \int_{-\infty}^{\infty} \mathrm{Im}\left\{\frac{i\rho\omega}{(2\pi)} \int_{-\infty}^{\infty} \phi dk_y\right\}$$

$$\cdot \mathrm{Im}\left\{\int_{-\infty}^{\infty} U dk_y\right\}\left[\frac{\delta}{2} (k_y + k_y') + \frac{\delta}{2} (k_y - k_y')\right]$$

$$+ h \cos\omega t \int_{-\infty}^{\infty} \mathrm{Re}\left\{\frac{i\rho\omega}{(2\pi)} \int_{-\infty}^{\infty} \Phi dk_y\right\}$$

$$\cdot \mathrm{Re}\left\{\int_{-\infty}^{\infty} U\left[\frac{\delta}{2} (k_y + k_y') + \frac{\delta}{2} (k_y - k_y')\right] dk_y'\right\} \quad . \tag{A-34}$$

Since Φ and U are even in k_y, Eq. A-34 becomes

$$\Pi(t) = h \sin\omega t \int_{-\infty}^{\infty} \mathrm{Im}\left\{\frac{i\rho\omega}{2\pi}\,\Phi(k)\right\} \mathrm{Im}\{U(k)\}\, dk$$

$$+ h \cos\omega t\, (2\pi) \int_{-\infty}^{\infty} \mathrm{Re}\left\{\frac{i\rho\omega}{2\pi}\,\Phi(k)\right\} \mathrm{Re}\{U(k)dk\} \quad . \qquad \text{(A-35)}$$

The rms average Π is given by one-half of the peak Π_0:

$$\Pi_{rms} = \frac{h}{2}\left[\int_{-\infty}^{\infty} \mathrm{Im}\left\{\frac{i\rho\omega}{2\pi}\,\Phi(k)\right\} \mathrm{Im}\{U(k)\}dk \right.$$

$$\left. + \int_{-\infty}^{\infty} \mathrm{Re}\left\{\frac{i\rho\omega}{2\pi}\,\Phi(k)\right\} \mathrm{Re}\{U(k)\}dk\right] \quad . \qquad \text{(A-36)}$$

As an example of an application of the above formula, we compute, using the plane wave expansions, the power per unit length radiated by a monopole source in a two-dimensional environment. We will then compare this to the sound transmitted into free space at the slit. The plane wave expansion for the potential due to a monopole source at x = ℓ is

$$\Phi(k_y) = -\frac{i}{2}\,\frac{\tilde{S}_{2D}\, e^{-(x-e)\sqrt{k^2-k_y^2}\; i}}{\sqrt{k^2-k_y^2}} \qquad \text{(A-37)}$$

and the x-velocity due to this source is

$$\frac{\partial\Phi}{\partial x}(k_y) = -\frac{\tilde{S}_{2D}}{2}\, e^{i\sqrt{k^2-k_y^2}\;\ell} \quad . \qquad \text{(A-38)}$$

Calculating the peak power from Eq. A-38, we find

$$\Pi = \frac{1}{2\pi}\int_{-\infty}^{\infty} \mathrm{Im}\left\{\frac{1}{2}\,\rho\omega\tilde{S}_{2D}\,\frac{e^{i\sqrt{k^2-k_y^2}\,\ell}}{\sqrt{k^2-k_y^2}}\right\} \mathrm{Im}\left\{\frac{\tilde{S}_{2D}}{2}\,e^{i\sqrt{k^2-k_y^2}}\right\} dk_y$$

$$+\ \frac{1}{2\pi}\int_{-\infty}^{\infty} \mathrm{Re}\left\{\frac{\rho\omega}{2}\,\tilde{S}_{2D}\,\frac{e^{i\sqrt{k^2-k_y^2}\,\ell}}{\sqrt{k^2-k_y^2}}\right\} \mathrm{Re}\left\{\frac{\tilde{S}_{2D}}{2}\,e^{i\sqrt{k^2-k_y^2}}\right\} dk_y$$

$$\Pi = \frac{1}{2\pi}\int_{-k}^{k} \rho\,\frac{\omega\tilde{S}_{2D}^{2}}{4}\,\frac{dk_y}{\sqrt{k^2-k_y^2}} = \frac{\rho\omega\tilde{S}_{2D}}{8}\ . \qquad \text{(A-39)}$$

This is one-half of the total power from a source in a two-dimensional environment. (We calculate only the power going upstream.)

The calculation of power radiated into the three-dimensional environment is similar to that above. The differences are

1. the particle velocity u at the slit is doubled, and

2. the value of Φ is a value appropriate for a "line" wave radiating into a free environment.

Consider the *monopole source:*

$$u = -e^{i\sqrt{k^2-k_y^2}\,\ell}\;\tilde{S}_{2D}$$

$$\Phi = \frac{i}{4}\, e^{i\sqrt{k^2-k_y^2}\,\ell}\; h\tilde{S}_{2D}$$

$$\Pi_{peak} = h\left\{\int_{-k}^{k} \frac{\rho\omega}{2\pi}\,\frac{\tilde{S}_{2D}}{4}\,\tilde{S}_{2D}\cdot h\,dk_y\right\}\;;$$

$$k = \omega/c$$

$$\Pi_{peak} = \frac{h^2\tilde{S}_{2D}^2\rho\omega 2k}{8\pi} \tag{A-40}$$

$$\boxed{\Pi_{peak} = \frac{h^2\tilde{S}_{2D}^2}{4\pi}\,\rho\,\frac{\omega^2}{c}}$$

Consider the *vertical dipole:*

$$-U(k_y) = \frac{k_y}{\rho\omega}\,\tilde{F}_{2D}\, e^{i\sqrt{k^2-k_y^2}\,\ell}$$

$$\rho i\omega\Phi(k_y) = \frac{k_y}{4}\, h\,\tilde{F}_{2D}\, e^{i\sqrt{k^2-k_y^2}\,\ell}$$

$$\Pi_{peak} = h^2\left\{\int_{-k}^{k} \frac{k_y^2\tilde{F}_{2D}^2}{4\rho\omega 2\pi}\,dk_y\right\}$$

$$= \frac{2}{3}\,k^3h^2\,\frac{\tilde{F}_{2D}^2}{4\rho\omega 2\pi} \tag{A-41}$$

$$\boxed{\Pi_{peak} = \frac{\omega^2}{c^3\rho}\,\frac{\tilde{F}_{2D}^2h^2}{12\pi}}$$

Consider the *horizontal dipole:*

$$+u(k_y) = \frac{\sqrt{k^2-k_y^2}}{\rho\omega}\,\tilde{F}_{2D}\,e^{i\sqrt{k^2-k_y^2}\,\ell}$$

$$-\rho i\omega\Phi(k_y) = \frac{\sqrt{k^2-k_y^2}}{4}\,h\tilde{F}_{2D}\,e^{i\sqrt{k^2-k_y^2}\,\ell}$$

$$\Pi_{peak} = h^2\left\{\int_{-k}^{k}\frac{(k^2-k_y^2)\tilde{F}_{2D}}{4\rho\omega 2\pi}\,dk_y\right\}$$

$$\Pi_{peak} = \frac{h^2}{4\rho\omega\pi}\,\tilde{F}_{2D}^2\,k^2\left(\frac{2}{3}\,k\right) \tag{A-42}$$

$$\boxed{\Pi_{peak} = \frac{h^2}{12\rho\pi}\,\tilde{F}_{2D}^2\,\frac{\omega^2}{c^3}\cdot 2}$$

APPENDIX B

SOUND POWER RADIATION FROM LINE SOURCES IN A FREE-FIELD ENVIRONMENT

In this appendix we consider the sound power radiation from line sources, specifically volume sources and thrust and drag forces. The configuration considered is a sinusoidal line of singularities along the y-axis, with a phase shift between sources that produces a traveling wave (Fig. 27).

1. Volume Sources

We consider a line of volume sources along the y-axis of the form

$$Q(y,t) = Q_0 \exp[\dot{O}(k_y y-\omega t)] \quad , \tag{B-1}$$

where $Q(y,t)$ is volume outflow/unit length.

The velocity potential, ϕ, satisfies the wave equation with the boundary condition

$$\lim_{r \to 0} \left(2\pi r \frac{\partial \phi}{\partial r}\right) = Q_0 \exp[i(k_y y-\omega t)] \ . \tag{B-2}$$

The outgoing solution is

$$\phi(r,y,t) = -i \frac{Q_0}{4} H^{(1)}[(k^2-k_y^2)^{\frac{1}{2}} r] \exp[i(k_y y-\omega t)] \quad , \tag{B-3}$$

where $k = w/c$.

The far-field acoustic pressure is

$$\rho(r,y,t) \sim \frac{\rho\omega Q_0}{4} \sqrt{\frac{2}{\pi(k^2-k_y^2)^{1/2} r}} \exp[i(k^2-k_y^2)^{1/2} r] \times \exp[i(k_y y-\omega t)] \ . \tag{B-4}$$

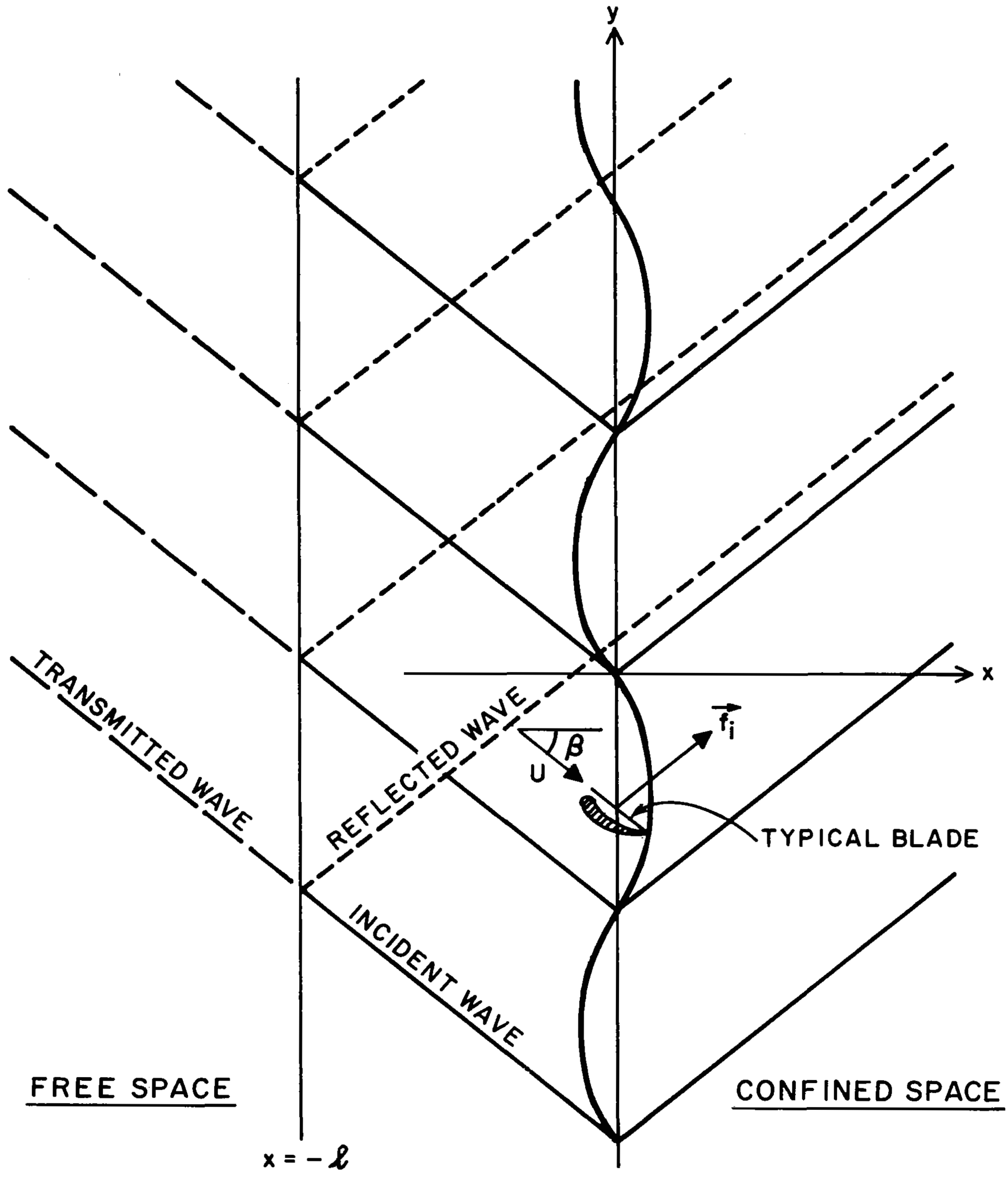

FIG.27 MODEL OF SOUND TRANSMISSION FROM CONFINED INTO FREE SPACE

The radial velocity (in the far field) is

$$V = \frac{Q_0}{4}(k^2-k_y^2)\sqrt{\frac{2}{\pi(k^2-k_y^2)^{1/2}r}}\exp[i(k^2-k_y^2)^{1/2}r] \times \exp[i(k_y y-\omega t)] \quad . \tag{B-5}$$

The rms acoustic power radiated/unit length is given by

$$\boxed{\begin{aligned} \Pi = \frac{1}{2}2\pi r|p||V_r| &= \frac{\rho c k Q^2}{8} \qquad \text{for } k > k_y \\ &= 0 \qquad\qquad \text{for } k < k_y \end{aligned}} \tag{B-6}$$

(p and V_r are in phase in the far field). This result can easily be understood in terms of the Mach number of the wave

$$M_c = (\omega/k_x)/c = k/k_x \ .$$

Note that the power radiated is independent of k_y, the mode wavenumber, once the Mach number, M_c, exceeds 1. [Although in the line model any value of k_y is appropriate, in the compressor model, $(k_y R_o)$ must be an integer.]

2. Thrust and Drag Forces

We now consider a sinusoidal line of thrust and drag forces of the form

$$\vec{f}_i = t_i \exp[i(k_y y-\omega t)]\vec{i} - d_i \exp[i(k_y y-\omega t)]\vec{j} \ . \tag{B-7}$$

The direction of $\vec{f}_i$ is chosen to be appropriate for Ω and k_y positive. The solution for the pressure is obtained directly as a sinusoidal superposition of point drag and thrust dipoles located along the y axis

$$p(x,y,zt) = \frac{t_i}{4\pi} \int_{-\infty}^{\infty} \frac{\partial}{\partial z} \left[\frac{e^{ikr_0(\eta)}}{r_0(\eta)} \right] e^{i(k_y\eta-\omega t)} \, d\eta$$

$$- \frac{d_i}{4\pi} \int_{-\infty}^{\infty} \frac{\partial}{\partial y} \left[\frac{e^{ikr(\eta)}}{r_0(\eta)} \right] e^{i(k_y\eta-\omega t)} \, d\eta \ , \qquad \text{(B-8)}$$

where $r_0(\eta) = [x^2+(y-\eta)^2+z^2]^{1/2}$ and $r = (x^2+z^2)^{1/2}$.

The relation

$$\frac{\partial}{\partial y} [r_0(\eta)] = \frac{\partial}{\partial \eta} [r_0(\eta)]$$

is used to re-express the second integral; after an integration by parts, we obtain

$$p(x,y,z,t) = \frac{t_i}{4\pi\partial} \frac{\partial}{z} \int_{-\infty}^{\infty} \left[\frac{e^{ikr_0(\eta)}}{r_0(\eta)} \right] e^{i(k_y\eta-\omega t)} \, d\eta$$

$$- \frac{ik_y d_i}{4\pi} \int_{-\infty}^{\infty} \frac{e^{ikr_0(\eta)}}{r_0(\eta)} e^{i(k_y\eta-\omega t)} \, d\eta \ . \qquad \text{(B-9)}$$

The integral is proportional to the Hankel function $H_0^{(1)}$. The result is

$$|p(x,z)| = \frac{1}{4} \left(t_i \frac{\partial}{\partial z} - ik_y d_i \right) \left\{ H_0^{(1)} [(k^2-k_y^2)^{1/2} r] \right\} \ . \qquad \text{(B-10)}$$

The acoustic far-field pressure is

$$|p(r,\theta)| = \frac{1}{4}\,(t_i\sqrt{k^2-k_y^2}\ \sin\theta - k_y d_i)\left[\frac{2}{\pi(k^2-k_y^2)^{\frac{1}{2}}}\right]^{\frac{1}{2}} \quad , \qquad \text{(B-11)}$$

where $\sin\theta = z/r$. The radial velocity is obtained from

$$V_r = \frac{\partial\phi}{\partial r} = \frac{-i}{\rho\omega}\frac{\partial p}{\partial r} \quad .$$

In the acoustic far field

$$v_r(r,\theta) = \frac{1}{4}\,\frac{(k^2-k_y^2)}{\rho\omega}\,[t_i(k^2-k_y^2)^{\frac{1}{2}}\ \sin\theta - k_y d_i] \quad . \qquad \text{(B-12)}$$

The rms acoustic power/unit length is obtained by integration:

$$\Pi = \frac{1}{2}\int_0^{2\pi} r|p|\,|v|\,d\theta \quad , \qquad \text{(B-13)}$$

where $|p|\,|v| = \frac{1}{16\pi\rho c k}\,[t_i(k^2-k_y^2)\ \sin\theta - d_i k_y]^2$.

In the integration from $\theta = 0$ to 2π, the contribution from the $t_i d_i$ cross term cancels; the expression for total power is

$$\boxed{\Pi = \frac{1}{8\rho c k}\left[\frac{t_i^2}{2}\,(k^2-k_y^2) + k_y^2 d_i^2\right]} \qquad \text{(B-14)}$$

For $k_y = 0$, $\Pi = t_i^2 k/16\rho c$, which is the result for a two-dimensional acoustic dipole.

One can also identify the power radiated "forward" and "rearward" by integrating from $\theta = 0, \pi$ and from π to 2π. This integration gives

$$\Pi_{\substack{\text{forward} \\ \text{rearward}}} = \frac{1}{16\rho c k} \left[\frac{t_i^2}{2} (k^2 - k_y^2) + k_y^2 d_i^2 \right.$$

$$\left. \mp \frac{4}{\pi} d_i t_i (k^2 - k_y^2)^{\frac{1}{2}} k_y \right] \qquad k > k_y \quad . \text{(B-15)}$$

As in the theory of propeller noise, the relationship of the lift and drag forces is such that more power is radiated downstream.

APPENDIX C

TRANSMISSION INTO A THREE-DIMENSIONAL ENVIRONMENT FROM LINE SOURCES IN A TWO-DIMENSIONAL ENVIRONMENT

We now consider the sound radiated by a sinusoidal distribution of thrust and drag forces confined between two closely spaced parallel plates of infinite vertical extent and semi-infinite horizontal extent, modeling the annular duct of a compressor as shown in Fig. 6. We are interested in the total acoustic power/unit length radiated into the free space beyond the edge of the confined flow. Figure 27 shows the configuration for the mathematical details. A singularity distribution of forces is located along the y-axis with the form

$$\vec{f}_i = t_i\, e^{i(k_y y-\omega t)}\, \vec{i} + d_i\, e^{i(k_y y-\omega t)}\, j \quad . \tag{C-1}$$

(Complex exponential notation will be used for convenience.) In two-dimensional flow, the acoustic field due to a point force at the origin is

$$p(x,y,t) = \frac{it_i}{4}\frac{\partial}{\partial x} H_0^{(1)}\, [(k^2-k_y^2)^{\frac{1}{2}} r]$$

$$+ \frac{id_i}{4}\frac{\partial}{\partial y}\{H_0^{(1)}[(k^2-k_y^2)^{\frac{1}{2}} r]\} \quad . \tag{C-2}$$

For small r, $H_0^{(1)} \sim \frac{i2}{\pi} \log r$, so that

$$p(x,y,t) \sim -\frac{t_i}{2\pi}\frac{\partial}{\partial x}(\log r) - \frac{d_i}{2\pi}\frac{\partial}{\partial y}(\log r) \quad . \tag{C-3}$$

For a sinusoidal distribution of forces along the axis,

$$\underset{\lim\ x\to 0}{p(x,y,t)} \sim -\frac{t_i}{2\pi}\int_{-\infty}^{\infty} e^{i(k_y\eta-\omega t)} \frac{\partial}{\partial x}\{\log[r(\eta)]\}\, d\eta$$

$$+\frac{d_i}{2\pi}\int_{-\infty}^{\infty} e^{i(k_y\eta-\omega t)} \frac{\partial}{\partial \eta}\{\log[r(\eta)]\} \ , \qquad \text{(C-4)}$$

where $r(\eta) = [x^2+(y-\eta)^2]^{\frac{1}{2}}$ and the substitution $\partial/\partial y\ [r(\eta)] = \partial/\partial\eta\ [r(\eta)]$ has been made. The last term may be integrated by parts to give

$$-\frac{id_ik_y}{2\pi}\int_{-\infty}^{\infty} \log r(\eta)\ e^{i(k_y\eta-\omega t)}\, d\eta \ . \qquad \text{(C-5)}$$

Since $1/2\pi\ \partial/\partial x\ (\log r)$ is a generalized function for the delta function, the first term implies that one boundary condition to be satisfied on the y-axis is

$$\Delta p = p(0^+,y) - p(0^-,y) = -t_i\ e^{i(k_y y-\omega t)} \ . \qquad \text{(C-6)}$$

Solving for the contribution to the velocity potential results in

$$\underset{\lim\ y\to 0}{\phi(x,y,t)} = -\frac{id_ik_y}{2\pi\rho\omega}\int_{-\infty}^{\infty} \log[r(\eta)]\ e^{i(k_y\eta-\omega t)}\, d\eta \ . \qquad \text{(C-7)}$$

We take the x derivative of Eq. C-7 to obtain delta function behavior in the integral.

Since $\partial\phi/\partial x$ is the horizontal velocity u, we obtain a second boundary condition for the jump in horizontal velocity at the y-axis:

$$U = U(0^+,y) - U(0^-,y) = \frac{d_ik_y}{\rho\omega}\ \dot{e}^{\ i(k_y y-\omega t)} \ . \qquad \text{(C-8)}$$

Equation C-6 could have, of course, been directly obtained from Eq. C-1, but it is useful to carry it along in the derivation of C-8.

We now solve the problem sketched in Fig. 27: acoustic radiation by a line of singularities in a semi-infinite confined region with free space beyond. At the edge of the slit, the boundary condition is p = 0, so that

$$p(-\ell,0) = 0 \quad . \tag{C-9}$$

Equation C-9 is the first-order approximation for a narrow slit (narrow meaning $h << \lambda$).

The main features of the problem are:

1. Plane oblique acoustic waves are generated at the y-axis.

2. A significant portion of the power generated at the singularities is reflected at the opening and is transmitted to $X = \infty$ (immediately raising the issue of the applicability of semi-infinite models to compressors).

3. The boundary condition, p = 0, causes a doubling of the horizontal velocity.

4. The slit then acts like a line of volume sources as described in Appendix B. The acoustic power/unit length radiated into free space is obtained from Eq. B-6.

The solutions to the problem are plane waves that are oblique to the y-axis and of the form

$$\phi(x,y,t) = \left[A_0 \, e^{i(k^2-k_y^2)^{\frac{1}{2}}x} + B_0 \, e^{-i(k^2-k_x^2 \; x)} \right] e^{i(k_y y-\omega t)}$$

$$\text{for } -\ell < x < 0$$

$$\phi(x,y,t) = C_0 \, e^{i(k^2-k_y^2)^{\frac{1}{2}}x} \, e^{i(k_y y-\omega t)} \qquad \text{for } x > 0 \quad . \tag{C-10}$$

A_0, B_0, and C_0 are determined from the boundary conditions C-6, C-7, and C-8:

$$A_0 = \frac{i}{2\rho ck}\left[t_i - \frac{d_i k_y}{(k^2-k_y^2)^{\frac{1}{2}}}\right] e^{-i2\ell(k^2-k_y^2)^{\frac{1}{2}}}$$

$$B_0 = \frac{i}{2\rho ck}\left[t_i - \frac{d_i k_y}{(k^2-k_y^2)^{\frac{1}{2}}}\right]$$

$$C_0 = \frac{i}{2\rho ck}\left[t_i + \frac{d_i k_y}{(k^2-k_y^2)^{\frac{1}{2}}}\right] . \qquad \text{(C-11)}$$

Transmitted Power

The horizontal velocity at the slit is

$$u = \frac{\partial\phi}{\partial x} = \frac{i}{\rho\omega}(k^2-k_y^2)^{\frac{1}{2}}\left[t_i - \frac{d_i k_y}{(k^2-k_y^2)^{\frac{1}{2}}}\right] e^{-i\ell(k^2-k_y^2)^{\frac{1}{2}}} + e^{i(k_y y-\omega t)} .$$

(C-12)

From Appendix B, the rms power/unit length radiated by this sinusoidal line of volume sources, completely unbaffled (as in Fig. 6), is

$$\Pi = \frac{1}{8\rho ck}\left[t_i(k^2-k_y^2)^{\frac{1}{2}} - d_i k_y\right]^2 t^2 \qquad k > k_y$$

$$= 0 \qquad f < k_y , \qquad \text{(C-13)}$$

where t_i and d_i are the force/unit length and $t_i t$ and $d_i t$ are consequently equivalent to three-dimensional forces.

If the source is baffled, the power is

$$\Pi = \Pi_{\text{unbaffled}} * \frac{2\Pi}{\Lambda} ,$$

where Λ is the "open" angle, i.e., for a plane wall baffle, $\Lambda = \pi$. For the annular compressor duct of Fig. 6, $\Lambda = 3\pi/2$ might be appropriate, although modeling an actual compressor inlet by any baffled or unbaffled duct is problematical.

APPENDIX D

CONSIDERATIONS CONCERNING THE DEVELOPMENT OF A DIFFERENTIAL-PRESSURE SENSOR

1. Design Requirements

A differential pressure sensor with a total thickness of 0.10 in. poses some unique problems. The size requirement dictates that most of the components and techniques fully utilize "state-of-the-art" expertise.

Following is a brief discussion of some design requirements and their solutions.

a. Case strain

Requirement:

Transducer-body design capable of being mounted in compressor blade without introducing case strains.

Solution:

i) For rigidity all case materials were selected to be stainless steel.

ii) A center support arrangement as shown in Fig. 28 was chosen to guarantee that the mounting technique would not introduce any unnecessary case strains at the g loads anticipated. The lock ring clamps the sensor uniformly in place and allows both diaphragm areas to be free from any hard mounting to the compressor blade. A soft RTV compound fills the remaining voids and preserves the integrity of the blade surface.

b. Sensitivity

Requirement:

Sensitivity of each sensing element uniform within ± 1 dB.

Solution:

i) Careful quality control and precise workmanship were necessary to maintain the sensitivity within the allowable tolerances.

ii) All piezoelectric elements were cut on an ultrasonic grinder to diameter tolerances of 0.0002-in. diameter at BBN to insure their roundness. The element size is 0.050-in. diameter by 0.010 in. thick.

iii) Silver brazing of the 0.001-in. stainless steel diaphragms with a maximum fillet of 0.001-in. diameter was accomplished with techniques commonly employed at BBN. This tight control of the brace was necessary to insure a uniform active area of the diaphragm.

iv) All components were ultrasonically cleaned after manufacture and again before assembly.

c. Low output impedance

Requirement:

Spurious signals generated from lead vibration.

Solution:

i) Piezoelectric elements typically exhibit impedances of 10^{-12} ohms, leaving the sensor prone to random signals generated by lead motion. This fact made an internal impedance lowering circuit mandatory.

ii) An F.E.T. hybrid circuit, with an output impedance of less than 1500 ohms, developed at BBN, was incorporated into the transducer body.

d. Centrifugal loads

Requirement:

DC signal imparted by centrifugal loading.

Solution:

i) A bias resistor of 5×10^8 ohms was selected to give a lower roll-off frequency of 50 Hz to eliminate any DC or near DC (0-10 Hz) signals caused by centrifugal loading or large temperature gradients.

e. **Vibration sensitivity**

Requirement:

Drastic lowering of vibration sensitivity.

Solution:

i) The fact that the two sensing elements must be of opposite polarity to produce a differential pressure pulse caused the vibration output to be in phase and thus led to a doubling of the vibration sensitivity. The vibration output of one of the sensing elements was shifted 180° to produce a reduction in vibration sensitivity of about 20 dB between 50 and 20,000 Hz below the original state. The phase shift of the vibration signal had to be accomplished without any phase shift of the pressure signal. Rearranging the spring mass ratios of one of the sensing elements provided the necessary results.

ii) The reasonably high-frequency data (20 kHz) required from this sensor eliminated the single diaphragm type of differential sensor. Porting arrangements for a single element sensor would not be adequate for the frequency requirements and would also interrupt the smooth surface of the compressor blade.

Figure 13 shows a schematic of the differential-pressure sensor and a photograph of some of the components.

2. **Specifications**

Sensitivity	-115 ±1 dB V/μbar
Vibration Sensitivity	≈100 dB SPL/g between 50 and 20,000 Hz
Noise Floor	-100 dB V
Frequency Response	50 to 20,000 Hz
Temperature Sensitivity	±1 dB for -50 to 160°F
Power Requirement	1 mA @ 9 Volt DC
Case Material	Stainless Steel
Output Impedance	<1500 Ω

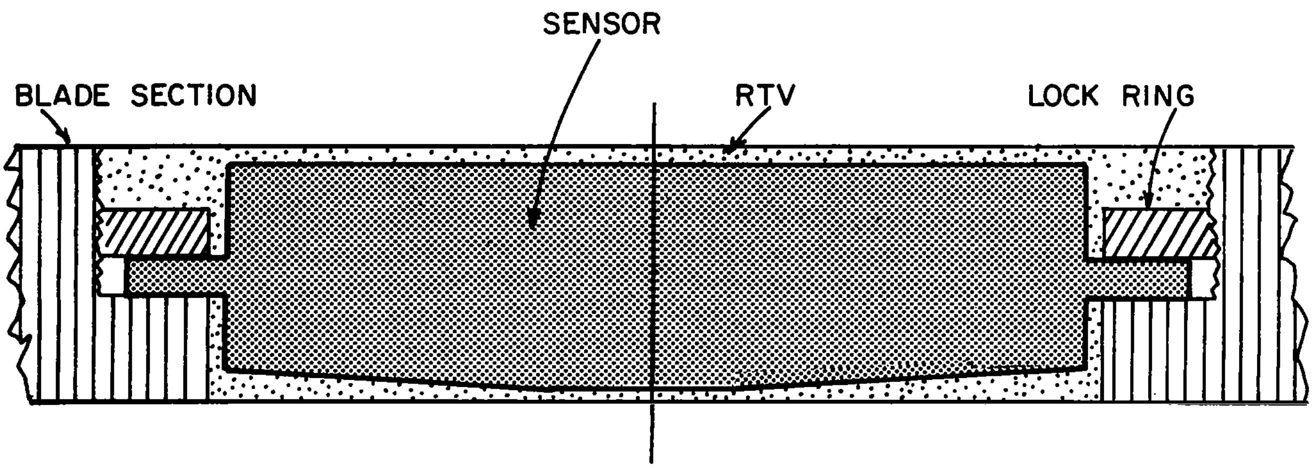

FIG. 28. MOUNTING OF DIFFERENTIAL-PRESSURE SENSOR IN BLADE

APPENDIX E

FM - Transmitter Specifications

Power Requirement	<7 mA
RF Frequency	within 88 to 104 mHz (selected for best reception)
Input Sensitivity	up to 125 mVolts
Noise Floor (shunted input)	<1 μvolt re input
Dynamic Range	47 dB
Signal Frequency Range	20 - 10,000 Hz
Temperature Compensation	50°F to 100°F
Battery Voltage	Nominal 1.4 volts
Weight of Transmitter	<10 grams
Range of Transmission	50 ft

APPENDIX F

CONSIDERATIONS CONCERNING THE CALIBRATION OF DIFFERENTIAL PRESSURE SENSORS

Differential sensors are used to obtain measures of the differential dynamic pressure on two opposite sides of a compressor blade. The use of differential sensors requires some special considerations.

The differential-sensor transfer function can be described in the following way:

$$e_0 = s_1 p_1 - s_2 p_2 \ , \tag{F-1}$$

where e_0 is the output voltage of the differential sensor, s_1 the pressure sensitivity of one side, and s_2 is the sensitivity of the other side. p_1 and p_2 are the dynamic pressures on sides 1 and 2.

If the sensor were ideal, s_1 would equal s_2 and $e_0 = (p_1 - p_2)$. However, in the small volume allowed in the size of the compressor blade, it is difficult enough to make a single measurement, much less a differential measurement. As a result s_1 differs somewhat from s_2 in the realization of the actual sensors, as will be shown below.

We examine the influence of a nonideal sensor where $s_1 \neq s_2$. Let the sensitivity be expressed as $s \pm a$, where $a = (s_1 - s_2)$ and $s = (s_1 + s_2)/2$. Equation F-1 is now rewritten as:

$$\begin{aligned} e_0 &= p_1(s + a) - p_2(s - a) \\ &= s(p_1 - p_2) + a(p_1 + p_2) \ . \end{aligned} \tag{F-2}$$

Here, the term $a(p_1 + p_2)$ is a correction to be applied to the data because of the mismatch in sensitivities.

To illustrate the effect we consider a hypothetical sensor with a 10% difference between s_1 and s_2. Assume $s_1 = 2.10$ µv/µbar and $s_2 = 1.90$ µv/µbar. We calculate s and a as:

$$s = \frac{s_1 + s_2}{2} = 2.00 \text{ v/}\mu\text{bar} \quad ,$$

$$a = \frac{s_1 - s_2}{2} = 0.10 \text{ v/}\mu\text{bar} \quad . \tag{F-3}$$

Assume $p_1 = 600$ µbars and $p_2 = 400$ µbars. The output voltage from the sensor will be:

$$e_0 = s_1 p_1 - s_2 p_2 = 1260 - 760 = 500 \ \mu\text{volts.}$$

By applying $e_0 = s(p_1 - p_2)$, the output signal of our hypothetical sensor would indicate a differential pressure of 250 µbars rather than the actual 200 µbars. Since s_1 is larger than s_2 ("a" is positive) we read a higher differential pressure. A correction factor K can be derived as follows:

$$\begin{aligned} K &= (\text{real diff. press.}) - (\text{indicated diff. press.}) \\ &= (p_1 - p_2) - \frac{e_0}{s} \\ &= -\frac{a}{s}(p_1 + p_2) \quad . \end{aligned} \tag{F-4}$$

We apply this correction to the above example and obtain $K = -0.05(1000) = -50$µbars. To use this correction we need to know "a" and $p_1 + p_2$.

The hypothetical measurement above is also shown in Fig. 29. The Δp without correction is 250 µbars. If the high-pressure side were reversed, the error would be low rather than high, giving an error band as indicated in Fig. 29. As p_1 and p_2 get larger, the error grows.

An estimate of $p_1 + p_2$ is important for the measurement so that corrections can be applied.

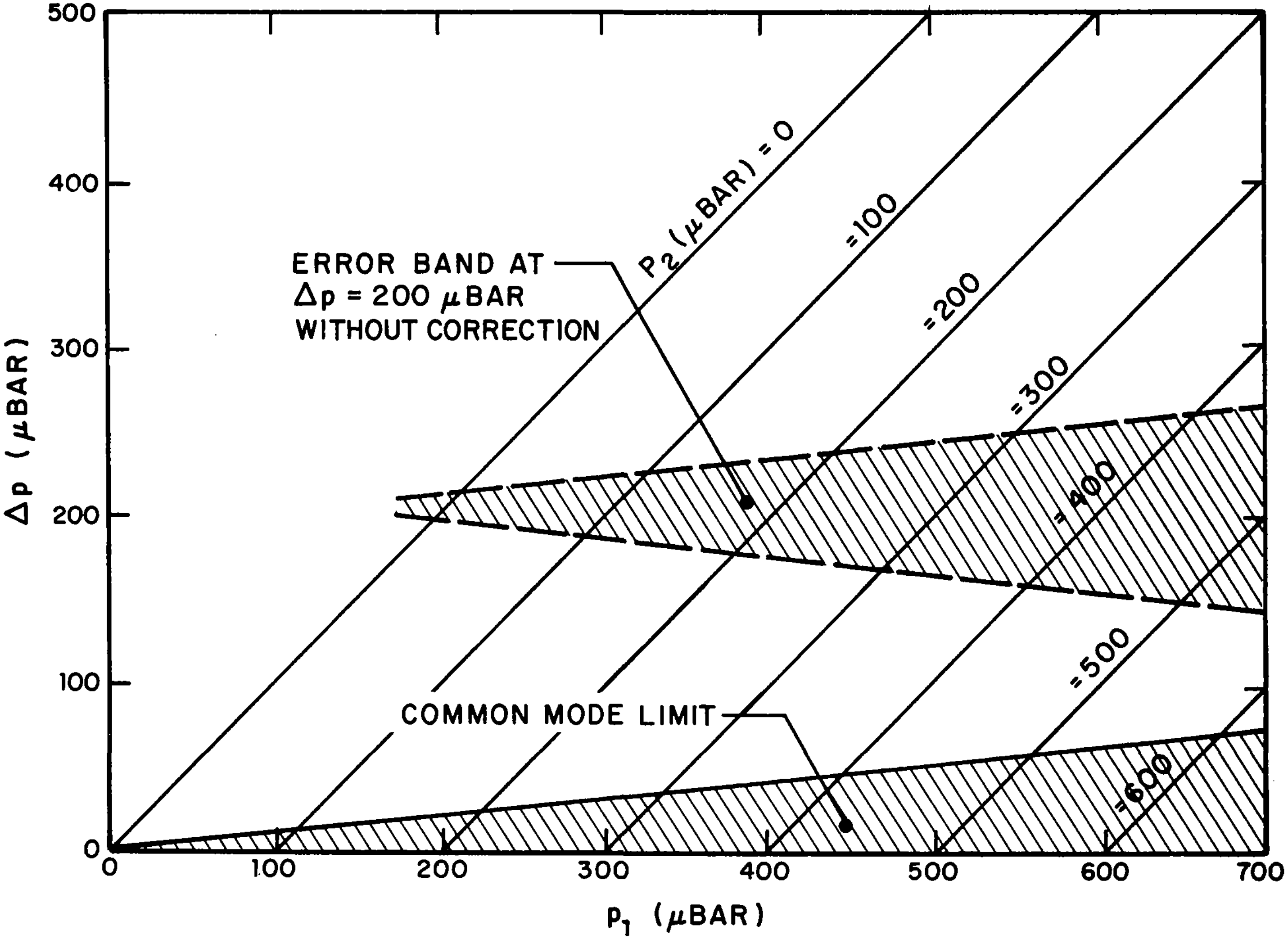

FIG.29 DIFFERENTIAL-PRESSURE MEASUREMENT WITH NON-IDEAL HYPOTHETICAL SENSOR.
s_1= 2.10 microvolt/microbar
s_2= 1.90 microvolt/microbar
s = 2.00; a = 0.10

A useful concept for differential measurements is common-mode rejection (CMR). Common-mode signals are those that are applied equally to both diaphragms. An ideally balanced sensor would yield an output of zero. A nonideal sensor gives an output that depends upon the degree of balance. The higher the CMR, the more accurately small differences can be measured in the presence of large pressures.

If we apply equal pressures of 500 μbars to our hypothetical unit, we obtain the following:

$$e_0 = 1050 - 950 = 100 \ \mu\text{volts} \quad ,$$

or an indicated pressure difference of 50 μbars. The CMR of the sensor is then 500/50, or 20 dB. This indicates a lower limit to the differential pressure that can be measured and which is indicated in Fig. 29 as the common-mode limit for the hypothetical sensor.

REFERENCES

1. Heller, H.H. and Widnall, S.E., "Correlation of Fluctuating Forces with Sound Radiation from Rigid Flow Spoilers," *J. Acoust. Soc. Amer.* **47** (May 1970).

2. Lowson, M.V., "Theoretical Studies of Compressor Noise," NASA CR-1287 (March 1969).

3. Lansing, D.L., "Exact Solution for Radiation of Sound from a Semi-Infinite Duct with Application to Fan and Compressor Noise," Symposium on Analytic Methods in Aircraft Aerodynamics, NASA SP-228 (October 1969).

4. Van Dyke, M., *Perturbation Methods in Fluid Mechanics* (New York Academic Press, New York, 1964).

5. Sears, W., "Aerodynamic Noise and the Sonic Room," *AIAA J.* 7, 517-586 (April 1969).

6. Morse, P.M. and Ingard, K.V., "Theoretical Acoustics," (McGraw-Hill Book Co., New York, 1968).